Observational Study on Properties of Photospheric Magnetic Field in the Polar Region of the Sun

太陽極域における光球面磁場の性質に関する観測的研究

Hiroaki Ito

伊藤 大晃

A Dissertation for the Degree of Doctor of Science

Nagoya University

2010

Acknowledgments

I would like to express my sincere gratitude to my supervisor, Professor Munetoshi Tokumaru, for giving me the opportunity to pursue this research, for his appropriate guidance and informative discussions in connection with my research, not to mention his unfailing encouragement throughout my graduate course. My sincere appreciation also to Professor Saku Tsuneta, who help guide my work, and for his informative discussions and clarifications in solar physics and about the *Hinode*, and for his critical reading and helpful suggestions for this thesis. I also wish to express my deep gratitude to the other members of the advisory committee on my thesis in the Solar-Terrestrial Environment Laboratory (STEL), Nagoya University, Professor Kanya Kusano and Associate Professor Satoshi Masuda, for their valuable comments on this thesis. I am indebted to Dr. Daikou Shiota in Computational Astrophysics Laboratory, RIKEN for his valuable advice and discussions in the cover of my research. He provided the computer code and the result for me to calculate a potential-field model in the corona. The research presented in this thesis has been carried out in collaboration with him.

I would also like to gratefully acknowledge Emeritus Professor Masayoshi Kojima, Associate Professor Satoshi Masuda and Assistant Professor Ken'ichi Fujiki for their helpful comments. I wish to acknowledge the engineering support of Kazuo Maruyama, and Yasushi Maruyama for the observation system of interplanetary scintillation at STEL. I am thankful to Mrs. Junko Okaniwa for her clerical support.

The MILOS code was developed by Orozco Suárez. The authors express sincere appreciation to his work, and thank him for allowing us to use the software. We acknowledge the useful comments and encouragements by D. Orozco Suárez, J.

Okamoto, Y. Katsukawa, L. Harra, E. Hiei., R. Ishikawa, R. Kano, N. Narukage, and K. D. Leka. *Hinode* is a Japanese mission developed and launched by ISAS/JAXA, collaborating with NAOJ as a domestic partner, NASA and STFC (UK) as international partners. Scientific operation of the *Hinode* mission is conducted by the *Hinode* science team organized at ISAS/JAXA. This team mainly consists of scientists from institutes in the partner countries. Support for the post-launch operation is provided by JAXA and NAOJ (Japan), STFC (UK), NASA, ESA, and NSC (Norway).

The white light coronal image taken by the Large Angle and Spectrometric Coronagraph (LASCO) on SOHO shown in Chapter 5 were produced by a consortium of the Naval Research Laboratory (USA), Max-Planck-Institut für Aeronomie (Germany), Laboratoire d'Astronomie (France), and the University of Birmingham (UK). SOHO is a project of international cooperation between ESA and NASA.

Last but not least, I would like to express my deep appreciation to my mother for their continuous support and encouragement throughout my graduate course.

Abstract of the Dissertation

The polar region of the Sun has not been explored well despite the long history of the solar observations. The polar regions are believed to have unipolar magnetic fields open to the interplanetary space. The polarity of the polar regions reverses around the maximum of the solar cycle. For several years around the solar activity minimum stable and large coronal holes are located in the polar regions. The mechanism of the polarity reversal and the mechanism on the formation of the coronal holes remain to be clarified. Observations of the polar magnetic field with its time variation are also critically important to understand the solar dynamo and the acceleration of solar wind. In this thesis, we investigate the property of the photospheric magnetic fields with the Solar Optical Telescope (SOT) aboard the *Hinode* satellite.

Following the introduction in Chapter 1, we summarize the spectropolarimetric observations to obtain the information of the magnetic fields in the solar photosphere in section 2.1 $\sim$ 2.3. We resolve the 180-degree ambiguity of the transverse magnetic fields with the assumption that the magnetic field vectors are either *vertical* or *horizontal* to the local surface (or undetermined).

We carried out high-resolution magnetic observations on both the North polar region and the quiet Sun at the East limb with the spectropolarimeter of the *Hinode*/SOT to characterize the polar region with respect to the quiet Sun in section 2.4 $\sim$ 2.5. Earlier observations with *Hinode* showed that the polar regions have scattered unipolar kilo-Gauss-patches (kG-patches). We find that the average area and the total magnetic flux of such kilo-Gauss magnetic concentrations in the polar region are larger than those of the quiet Sun.

In Chapter 3, We discuss the comparison between the polar region and the quiet region of the Sun. The magnetic field vectors classified as *vertical* in the quiet

Sun have symmetric histograms around zero in magnetic field strengths, showing balanced positive and negative fluxes, while the histogram in the North polar region is clearly asymmetric, showing a predominance of the negative polarity. The total magnetic flux of the polar region is larger than that of the quiet Sun. In contrast, the histogram of the *horizontal* magnetic fields is exactly the same between the polar region and the quiet Sun. This is consistent with the idea that a local dynamo process is responsible for the horizontal magnetic fields. A high-resolution potential field extrapolation shows that the majority of magnetic field lines from the kG-patches in the polar region are open with a fanning-out structure very low in the atmosphere, while in the quiet Sun, almost all the field lines are closed.

In Chapter 4, we report the yearly variation (2006 $\sim$ 2011) of the magnetic fields in the polar regions around solar minimum with *Hinode*/SOT. The fraction of the dominant magnetic flux in the polar regions increases with latitude. There is no clear boundary between the low-latitude quiet Sun and the polar coronal holes in the photospheric magnetic distributions. We examine the time variation of the vertical and horizontal magnetic flux and intrinsic fields. The comparison of the histograms for the areal fraction of the intrinsic magnetic field strength shows that those of the kG-patches slightly vary in the North polar region between 2006 $\sim$ 2008. In the South polar region, the histograms for the areal fraction of the kG-patches and the horizontal field are almost the same. It appears that the magnetic flux of vertical magnetic fields fluctuates more than that of the horizontal magnetic fields, which stays almost flat.

Summary and future works are presented in Chapter 5. At the beginning of 2011, when this study was completed, the solar activity began to rise. We have not observed the polar regions in one complete solar cycle. We hope that future investigations with *Hionde* clarify the formation process of the kG-patches, the polarity reversal process of the global magnetic field of the Sun, the formation and decay processes of the polar coronal holes, and the acceleration process of the high speed solar wind in the polar coronal holes.

Contents

Chapter 1

Introduction

In this chapter, we review our basic understanding on the solar atmosphere and solar magnetic fields, and introduce the *Hinode* satellite, which is extensively used in this thesis.

1.1 Vertical Structure of the Solar Surface

The sun mainly consistents of hydrogen and helium gas. The solar atmosphere is stratified because of the gravity, and is classified into four layers in its outer envelop; photosphere, chromosphere, transition region, and corona (Figure 1.1).

The layer that we observe in the visible light is called 'photosphere'. Energy transferred to the photosphere is lost mainly in a form of radiation into the outer space at the photosphere. The temperature of the photosphere decreases from 6400 K at the solar surface to the minimum value of 4100 K at the height of 500 km. At the temperature minimum, the temperature starts to increase outward again owing to yet unknown heating process. The layer higher than the temperature minimum up to about 2000 km is called 'chromosphere' (Figure 1.1). In this layer, temperature gradually increases with height. Then, the temperature sharply increases from 2×10^4 and a few 10^6 K. The high temperature layer is called 'corona', and the thin boundary layer between the chromosphere and the corona is called 'transition region'. The transition region is so sharp that there is practically discontinuity in a temperature and density. A mechanism to heat the outer solar atmosphere remains one of the great puzzles in solar physics.

In the solar interior, A photon produced in the solar interior is absorbed, scattered, and re-emitted by the plasma. The scattering and absorption become less

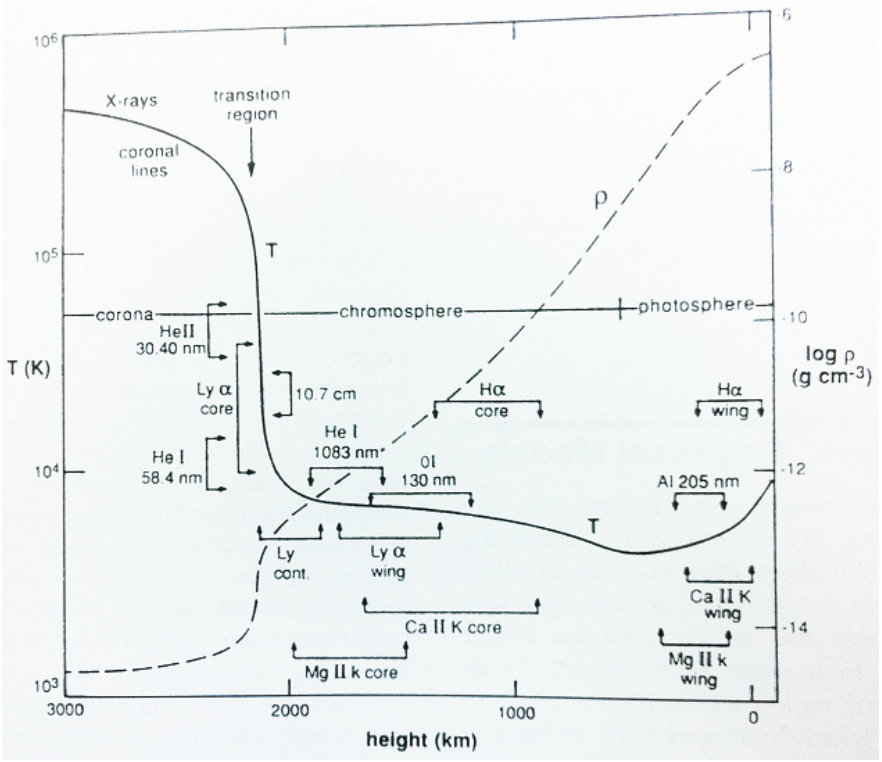

Figure 1.1: Temperature and density of the average quiet Sun as functions of height (model C). The calculated height intervals where the various continua and line features originate are indicated (Avrett 1999; Vernazza et al. 1981). The temperature distribution is for a model of the average quiet Sun and does not represent regions of the solar disk that are brighter and darker than the average.

efficient as the density of the medium decreases. At the photosphere, the atmosphere changes from completely opaque to completely transparent with height. The probability that a photon created at optical depth τ_ν can escape from the Sun without being absorbed or scattered is $e^{-\tau_\nu}$. The radiation spectra is almost black body with temperature of about 5780 K. Moving up the atmosphere, the temperature declines from a value about 6400 K at $\tau_{500nm} = 1$ to about 4100 K at a height of 500 km ($\tau_{500nm} \sim 10^{-3}$). The optical depth depends on the frequency ν of the photon and the direction from the vertical, and is related to the amount of the medium which the photon has to pass through. An observer can see the height at $\tau_\nu = 1$ at certain frequency ν. Hence, the height which we can see through at the solar limb is higher than that at the solar disk center. As described in section 1.1, the temperature decreases with height in the photosphere, the solar limb in visible wavelengths is darker than the Sun center. The effect is called 'limb darkening'.

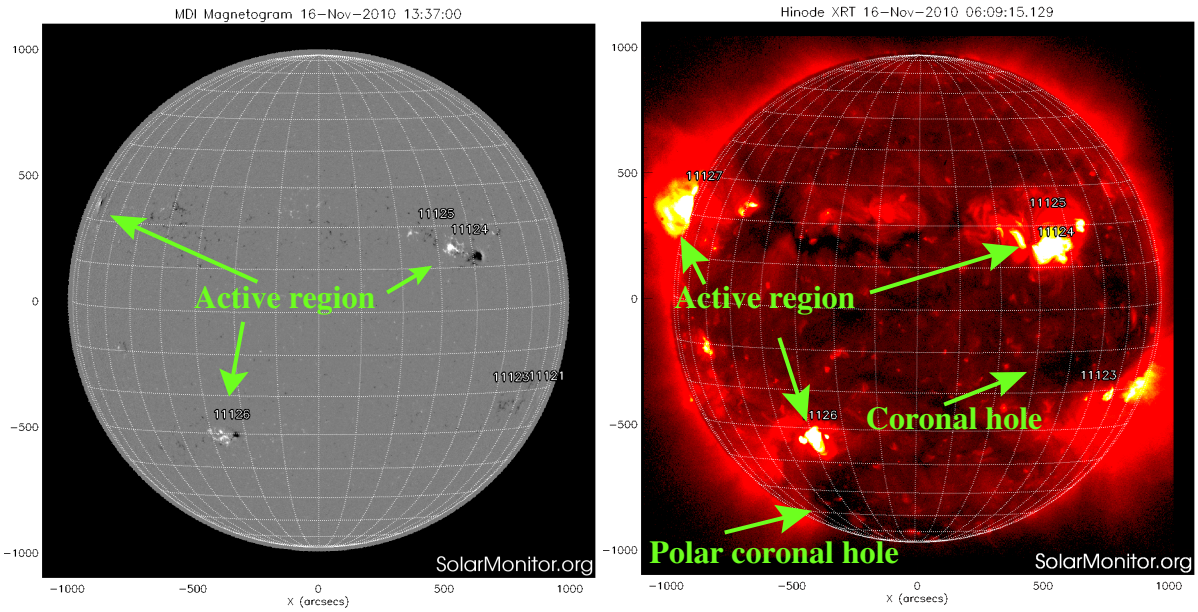

Figure 1.2: Left image; a full-disk magnetogram of the Sun obtained by Solar and Heliospheric Observatory (SOHO)/Michelson Doppler Imager (MDI). Right image of the Sun in x-rays (0.6 $\sim$ 20 nm) with *Hinode*/XRT. (Coursty of Solar monitor; http://www.solarmonitor.org/)

1.2 Global Structure of the Sun

Figure 1.2 is an image taken in X-rays which are emitted from the high temperature plasma in the solar corona, and is proportional to the squares of the plasma density. The brighter regions of the solar corona is thought to be strongly heated. There are many pieces of evidence that the amount of the heating is closely correlated with the magnetic field strength and/or the magnetic flux in the solar atmosphere. Thus, magnetic fields in the solar atmosphere would play a fundamental role to the heating of the corona. Here we introduce the global structure of the solar atmosphere, which is closely coupled with the highly structured magnetic fields.

1.2.1 Coronal Holes

In an X-ray image of the solar corona (Figure 1.2) we notice much darker regions, which have low-temperatures and low-density plasmas. Those regions are called coronal holes (Figure 1.3). In the polar coronal holes, plume structures are often observed in the white light observations during a solar eclipse. Coronal holes are thought to have magnetic fields open into the interplanetary space and be the origin

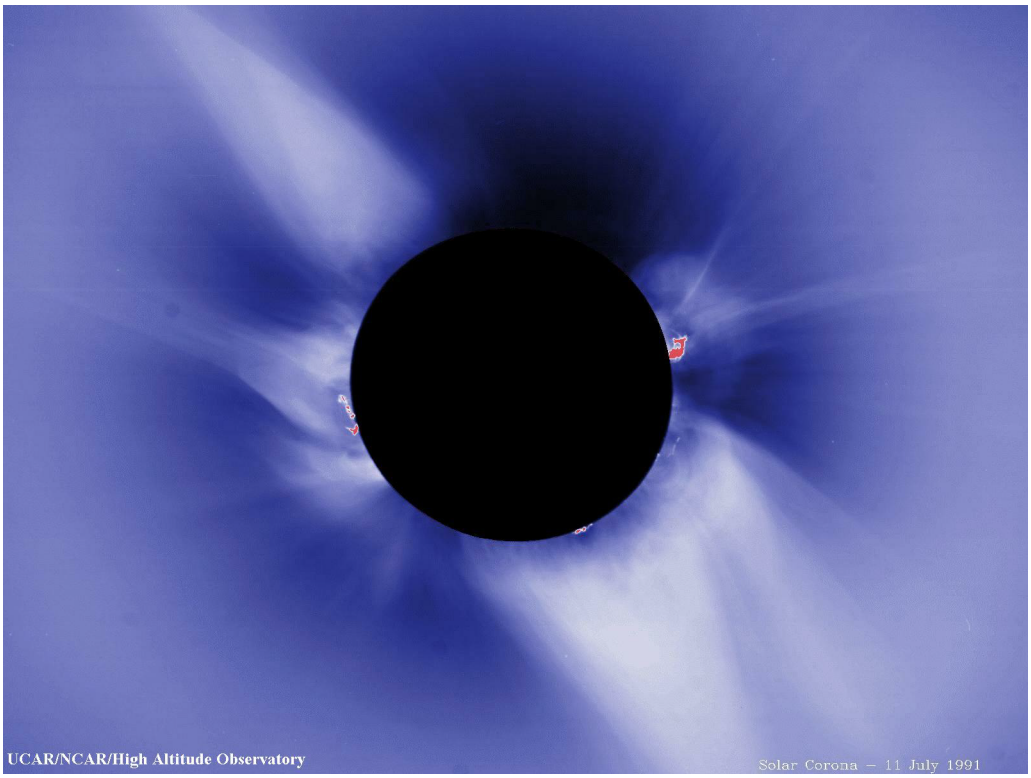

Figure 1.3: Image of the solar corona in white light. The subtle tendrils of the white light corona and the chromosphere. Courtesy of NASA. (http://solarscience.msfc.nasa.gov/corona.shtml)

of the fast solar wind. In particular, the polar coronal holes can be source regions of fast solar wind observed to flow in the high latitude region of heliosphere (Phillips et al. 1995a, b).

Coronal holes are not permanent structure which is formed and disappears one after the other. In an image of the photosphere, such as the white light image or magnetogram, there is no signature of the footprints of the coronal holes, while they are prominent in X-rays or extreme ultraviolet (EUV) images. The mechanism of the formations of the coronal holes remains to be a puzzle in solar physics. Coronal holes also show different spatial distribution depending on solar activities.

1.2.2 Active Regions

Active regions carried high magnetic flux with various magnetic concentrations such sunspots, plages, and pores. Sunspots are one of the most prominent magnetic structures in the surface of the Sun observed in magnetogram (Figure 1.2) and

in white light. The central dark regions of the sunspots are called umbra, whose brightness are about 0.3 times that of other regions of the Sun. The intrinsic field strength in the umbra generally reaches 2000 — 4000 Gauss, and their spatial scales are a few ten thousand kilometers. Pores are the smaller magnetic structures on the Sun. Their surface magnetic field strength is of the order of 1000 — 2000 Gauss and their diameter in continuum is typically only a few thousand kilometers.

The comparison between the two images in Figure 1.2 shows the correlation between magnetic flux on the photosphere and the accompanying X-ray brightness. A typical active region has a bipolar magnetic region. Although they are often complex in structure, they would contain equal amount of the positive and the negative magnetic fluxes. The overall diameter of an active region, within which the general magnetic field strength is about 100 Gauss, may be several hundred thousand kilometers.

Active regions (sunspots) are not permanent structure, i.e., they are formed and diffused. The number of active regions (sunspots) indicate degree of solar magnetic activity. The long term variation of the solar activity is described in the next section.

1.2.3 Quiet Sun

Quiet Sun refer to regions other than the active regions. Magnetic fields in the quiet Sun consist of much smaller scale magnetic concentrations which can be observed only in magnetogram. The magnetic fields in the quiet Sun concentrate at the boundary of the networks, which correspond to supergranulation. The network fields contain magnetic fluxes with both polarities, and the positive and negative magnetic fluxes are balanced on average. Magnetic flux per unit area is smaller than that of active regions, the temperature of the quiet Sun corona is lower than that of the active regions.

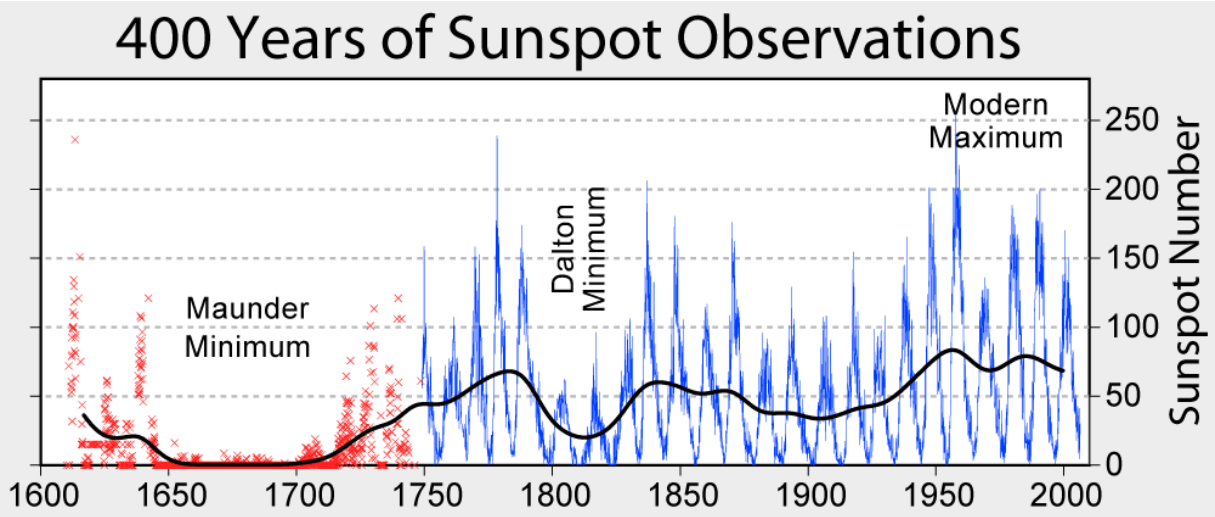

Figure 1.4: Yearly averages of historical sunspot number are derived from 1610 to 2010 (http://www.appinsys.com/GlobalWarming/GW_Part6_SolarEvidence.htm).

1.3 Cycle of Solar Activity

The cycle of the solar activity refers to a quasi-periodic variation with a span of about 11 years. The signatures of the cycle are apparent in many observational data. The best-known indicator of the solar cycle is the sunspot number. Figure 1.4 shows the yearly average of the sunspot number. The periodic variation is characterized by a rapid rise from the minimum to the maximum with peak phase, continuing 3–6 years (on average 4.8 years). The maximum is followed by a gradual decline lasting 5–8 years (on average 6.8 years). Individual sunspot cycles since 1710 range from 7 to 14 years (on average 11 years).

1.3.1 Variation of Sunspots Latitude (Butterfly Diagram)

The sunspots are formed as bipolar pairs, which consist of leading (West) and following (East) sunspots. The line connecting the center of a bipolar pair is slightly tilted to the equator, leading sunspots being nearest to the equator (Joy's rule).

Their latitudinal distribution changes with phase of the solar cycle. Figure 1.5 shows the latitudinal distribution of sunspots as a function of time. At the beginning of each cycle, the sunspots appear at about $30° - 35°$ latitude, in both hemispheres. Then sunspots appear in two belts parallel to the equator, whose midpoints are

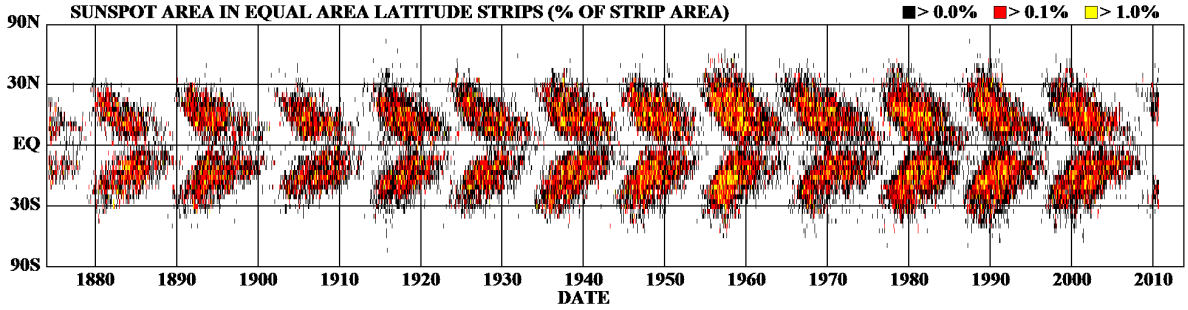

Figure 1.5: Image of the butterfly diagram of sunpots. The graph shows the position of sunspots in the years from 1870 to 2010. Notice that the centerline, from left to right, is the equator of the Sun and that sunspots occur North and South, above and below this line. Courtesy of NASA. (http://solarscience.msfc.nasa.gov/SunspotCycle.shtml)

located at $\pm 27°$ latitude in each hemisphere. As the solar activity grows, the latitude belts where sunspots emerge move equatorward down to about $\pm 8°$ (Spörer's law). This evolution shows a characteristic distribution which appears as a butterfly wing in Figure 1.5 this figure is called as the butterfly diagram.

1.3.2 Variation of Polarity of the Solar Magnetic Field

Figure 1.6 shows the time variation of the latitudinal distribution of signed magnetic field during the recent three solar cycles. All bipolar pairs of sunspots are substantially subject to the Hale-Nicholson polarity rules[*1]. The polarities of the bipolar regions in the northern and southern hemispheres of the butterfly diagram are opposite. The difference in latitude between the beginning and the end of a solar cycle allows an obvious distinction as to which of overlapping solar cycles a certain sunspots belongs. Considering the polarity reversal, the magnetic fields have a cycle period of about 22 years, which is referred to as the Hale cycle.

Leighton (1964) reported that the supergranular diffusion and the poleward meridional flow transport the magnetic fields disinterested from sunspots and active regions, and provides magnetic flux to the quiet Sun and possibly to the polar regions. Figure 1.6 also shows that magnetic flux, whose polarity is opposite to those of polar regions, are moved from the sunspot latitude to the pole in each hemisphere.

[*1]Hale-Nicholson polarity rules describe that the preceding polarity spots are usually the dominant leading spots in most groups for the 22 year sunspot cycle. The magnetic polarities of leading and trailing spots are opposite, and those of the leading spots in one hemisphere are opposite to those of the leading spots in the other hemisphere.

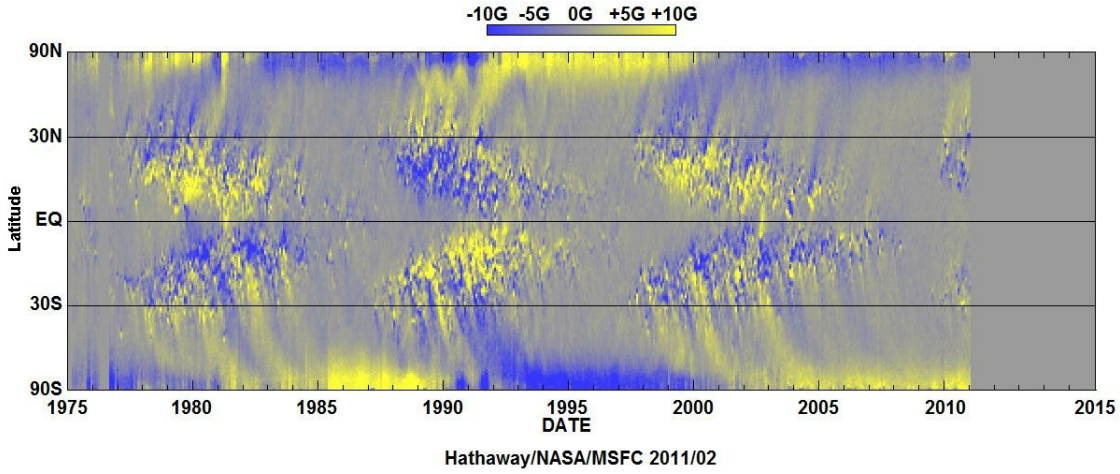

Figure 1.6: Image of the butterfly diagram of magnetic field strength. The graph shows the distribution from 1975 to 2011, last three solar cycles. Notice that the centerline, from left to right, is the equator of the Sun and that sunspots occur North and South, above and below this line. Courtesy of NASA. (http://solarscience.msfc.nasa.gov/SunspotCycle.shtml)

Then the polarity of the poles are reversed at the solar maximum in each cycle. The polar regions would play an important role to the cyclic behavior of the solar magnetic fields. However, the detailed process and timing of the polarity reversal still remain completely unknown due the severe limitation of the observation of the polar magnetic fields (Capter 2). In this study, we performed first comprehensive studies of the polar magnetic field overcoming the limitations using the high resolution observations with *Hinode* satellite.

1.4 The "Hinode" Satellite

Hinode was launched on September 23, 2006. The scientific goals of the *Hinode* mission are the following (Kosugi et al. 2007);

1. To understand the processes of magnetic field generation and transport including the magnetic modulation of the Sun's luminosity.

2. To investigate the processes responsible for energy transfer from the photosphere to the corona and for the heating and structuring of the chromosphere and the corona.

3. To determine the mechanisms responsible for eruptive phenomena, such as flares and coronal mass ejections, and understand these phenomena in the context of the space weather of the Sun — Earth System.

Hinode has three scientific instruments: Solar Optical Telescope (SOT), Extreme ultraviolet Imaging Spectrometer (EIS), and X-Ray Telescope (XRT), as is shown in Figure 1.7. The *Hinode* has a sun-synchronous polar orbit, allowing to observe the sun continuously.

SOT is the largest optical solar telescope ever sent to space, which has a 50cm aperture mirror (Tsuneta et al. 2008b). SOT has an 0".2 resolution with the image stabilization system (Correlation Tracker and Tip-tilt Mirror System; Shimizu et al. 2008) both for spectrograph and filtergram. SOT observes the layers from the photosphere to the chromosphere with two powerful focal-plane instruments; Spectro-Polarimeter (SP) and Filtergraph (FG). In the FG channel, a CCD camera is shared by the Broad-band Filter Imager (BFI) and the Narrow-band Filter Imager (NFI) (Table 1.1). BFI has 6 broadband filters which are centered on CN band, Ca II H, G band, blue continuum, green continuum, and red continuum, respectively. BFI can achieve the best spatial resolution of all the telescopes in the *Hinode*. Meanwhile, the goal of NFI is to obtain the velocity and the magnetic fields by shifting the wavelength of the observation using the tunable birefringent filter. NFI can detect Mg Ib, NaD, Hα, and three Fe I lines. Both BFI and NFI can achieve extremely high cadence ($\sim$ 4 second) observations. The FG permits to study events that dynamically vary in terms of their structure such as spicules (De Pontieu et al. 2007) and prominences (Okamoto et al. 2007; Berger et al. 2008). The SP

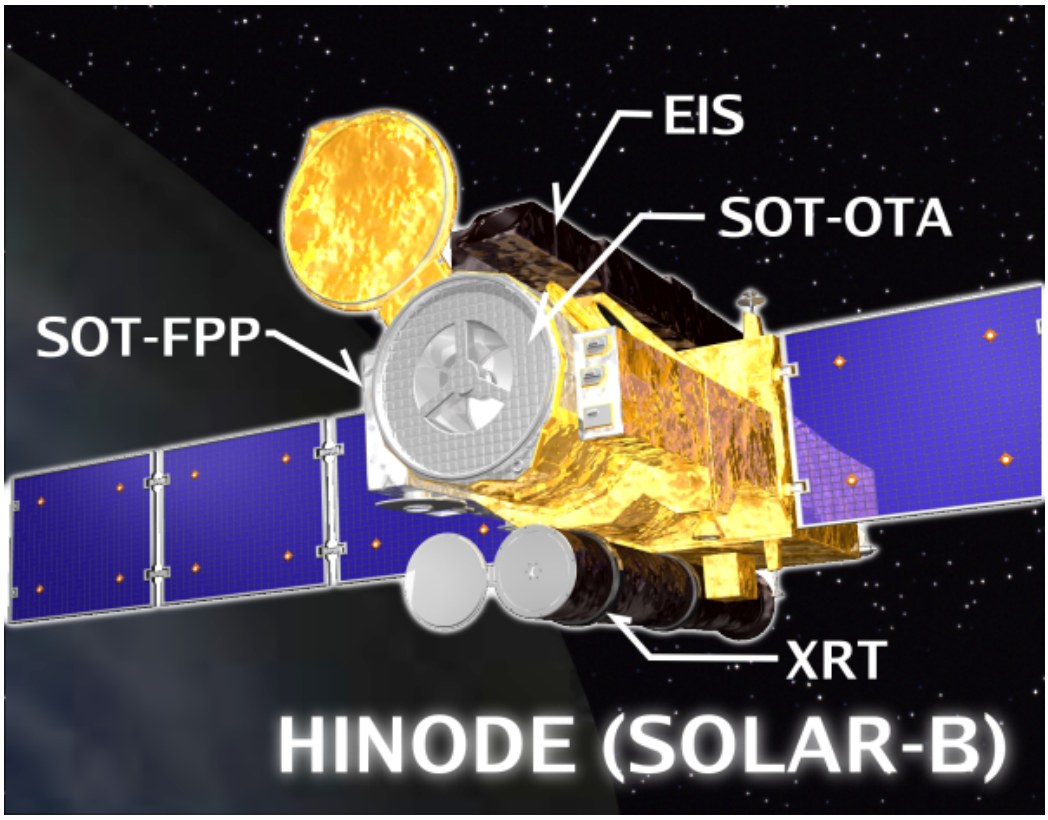

Figure 1.7: A illustration of the *Hinode* satellite. The Solar Optical Telescope (SOT) consists of the main telescope (the Optical Telescope Assembly; SOT-OTA) and the Focal Plane Package (SOT-FPP). The size of the satellite is 4.0 m (body length) × 1.6 m (body width) × 10 m (paddle length), and its weight is 900 kg. (Courtesy of *Hinode* science center; http://solar-b.nao.ac.jp/panf/)

obtains the full Stokes parameters using the Fe I 630nm absorption line with a polarization accuracy of $\sim$ 0.1 %. We can derive the physical parameters such as three dimensional magnetic field components, LOS velocity, temperature, source function, and the filling factor; assuming a certain atmospheric model with the inversion of the Stokes profiles. There are three observing modes, Normal mapping, Fast mapping and Dynamics, for the SP (Tsuneta et al. 2008b).

The EIS (Cluhane et al. 2007) is an imaging spectrometer designed to observe plasmas in the temperaturerange from 0.1 MK to 10 MK, and can observe the spectrums of the transition region and the corona. The detector covers the wavelength ranges of 170-210 Å and 250-290 Å, which cover the region from the higher chromosphere to the corona. The EIS has a slit and slot exchanger that contains two narrow slits (1" and 2" width) and two wide slots (40" and 266" width) to be

Table 1.1: Focal Plane Package (FPP) Overview (from Tsuneta et al. 2008b).

Spectro-Polarimeter (SP)			
Field of view along slit	164" (North-South direction)		
Spatial scan range	± 164" (transverse to slit)		
Spacial sampling	0".16		
Spectral coverage	6300.5 ∼ 6303.2 Å		
Spectral resolution / sampling	30 mÅ/ 21.5 Å		
Polarization signal to noise	10^{-3}		
Measurement polalization	Stokes I, Q, U, V simultaneously		
Broadband Filter Imager (BFI)			
Field of view	218" × 109" (Full FOV)		
CCD	4k × 2k pixels (Full FOV), shared with NFI		
Spacial sampling	0".054		
Spectral coverage			
Center (Å)	Width (Å)	Line of interest	Purpose
3833	7	CN I	Magnetic network image
3968	3	Ca II H	Chromospheric heating
4305	8	CH I	Magnetic elements
4504	4	Blue continuum	Temperature
5550	4	Green continuum	Temperature
6684	4	Red continuum	Temperature
Broadband Filter Imager (BFI)			
Field of view	328" × 164" (unvignetted 264" × 164")		
CCD	4k × 2k pixels (Full FOV), shared with NFI		
Spacial sampling	0".080		
Spectral coverage			
Center (Å)	Width (Å)	Line of interest	Purpose
5172	6	CN I	Chromospheric Doppler / magnetograms
5250	6	Fe I	Photospheric magnetograms
5576	6	Fe I	Photospheric Dopplergrams
5896	6	Na D	Chromospheric magnetograms
6302	6	Fe I	Photospheric magnetograms
6563	6	Hα	Chromospheric structure

chosen depending on the scientific purpose. From the observed emission lines, we can extract the physical parameters such as temperature, emission measure, plasma density, LOS velocity.

The XRT (Golub et al. 2007, Kano et al. 2008a) obtains high-resolution soft X-ray images that reveal magnetic field configuration and its evolution, permitting us to observe the energy buildup, storage and release process in the corona. The XRT has a 35 cm aperture grazing incidence mirror and can achieve 2" spatial resolution. One of the unique features of XRT is its wide temperature coverage to observe all the coronal features. The detector has nine analysis filters to diagnose a wide range of temperatures: thin-beryllium, med-beryllium, thick-beryllium, carbon-poly, thin-aluminum-poly, thin-aluminum-mesh, med-aluminum, thick-aluminum, and titanium-poly. In particular, the thin-aluminum-mesh filter made it possible to diagnose a cool plasma of 1 MK, which is beyond the temperature sensitivity of Yohkoh SXT (Savcheva 2008).

1.5 Purpose of This Study

The main purpose of this thesis is to obtain the properties of magnetic fields in the polar region of the Sun. The polar regions of the Sun have been given less attention despite the long time observations of the Sun. At present, while only active regions are extensively observed and investigated, the polar regions are still not sufficiently observed. As previously shown in sections 1.2 and 1.3, in both the polar regions, the stable and large coronal holes are present around the solar minimum. It is important to reveal the magnetic properties of the polar regions of the Sun to understand problems of solar dynamo, and fast solar wind acceleration.

Because of their location near the solar limb, it had been difficult to observe and analyze accurately the polar regions until *Hinode* was launched. In Chapter 2, we explain the methodology of the polar observations with *Hinode*/SOT. Second, we describe how we overcome the 180-degree ambiguity and determine the observed magnetic field vectors.

In Chapter 3, we present the magnetic field properties and distributions for the North polar region and the quiet region of the Sun. Tsuneta et al. (2008a) found many patchy concentrations of magnetic fields with field strengths exceeding 1 kG

in the polar region. We further clarify the properties of the polar region and the kG-patches in terms of those of the quiet Sun.

In Chapter 4, we describe the four-year-variation of the magnetic fields in the North and South polar regions. We monitor the fraction of the dominant magnetic flux in the two polar regions from 2006 to 2011. We discuss the North-South-asymmetry and the variation of the magnetic flux in the four years near the solar minimum. Chapter 5 is allocated to a brief summary of the thesis with the open issues for future works.

Chapter 2

Observation and Analysis

2.1 Spectropolarimetric Observations

As shown in Chapter 1, the magnetic fields of the Sun drives the activities of the Sun. The measurement of the magnetic fields is extremely important to understand the casual relationship. In this section, we describe the methodology for the measurement of the magnetic fields in the solar atmosphere.

In the solar spectrum, there are a large number of absorption lines. An absorption line is formed by a resonance between an atm and a photon whose energy corresponds to the energy of a transition between certain atomic levels of the atm. The presence of magnetic fields in the solar atmosphere splits the degenerated atomic levels, causing the slight wavelength shift of the transition. This effect is called the Zeeman effect. This process causes not only the wavelength shift but also a polarization. The polarized line profile contains information on the magnetic field information.

In the spectropolarimetry, polarization state (Stokes parameter) of the absorption profile is measured as a function of wavelength. Figures 2.1 and 2.2 are examples of the spectropolarimetric data. In order to observe large area on the plane of the sky, we have to scan the region of interest.

The polarization of the spectral lines (Figure 2.1) allows us to infer both the strength and the orientation of the magnetic fields. Polarized light can be described by the Stokes vectors $\mathbf{X} = [I, Q, U, V]^T$, where the superscript ^{T} is transpose of the four vectors. The components of the Stokes vector can be obtained by the following set of the polarization measurements (Figure 2.2): I is the intensity, Q is the difference of intensities measured with two orthogonal linear polarizers, U is similarly

obtained with the set of the orthogonal polarizers rotated by 45°, and V is the difference in intensities measured with two orthogonal circular polarizers. Figure 2.1 indicates that the linear polarization spectra (Stokes Q, U) tend to be symmetric about the center of these absorption lines, while the Stokes V is antisymmetric. The magnitude of the splitting is proportional to the intrinsic magnetic field strength; the linear polarization signal is detected only if the magnetic field vector is inclined to the line of sight (transverse component), and the circular polarization is present only if the magnetic field has a component along the line of sight (longitudinal component).

Ambiguity of 180 degree

The Stokes profiles contains information on the magnetic field strength and the orientation of the magnetic fields in the solar atmosphere. One drawback in the Stokes polarimetry is that for given Stokes Q and U, there is 180 degree ambiguity in the azimuth angle (rotation angle of the magnetic field vector around the line of sight) of the transverse magnetic field. This is because the linear polarization produced by the Zeeman effect is identical for either $\vec{B}_t$ or $-\vec{B}_t$. To resolve this ambiguity in the magnetic field azimuth angle ϕ, additional assumption is required. For example, one of the azimuth angles may be chosen such that it is closer to that of the potential magnetic field (Allen and Hagyard 1990; Moon et al. 2003). Note that the potential magnetic fields are obtained from the vertical component of the magnetic fields on the photosphere. Or one may choose the azimuth such that the discontinuity of the magnetic field vectors from one point to another is minimized (Metcalf 1994; Metcalf et al. 2006). However, there is no appropriate assumption in the polar region of the Sun. We will deal with this problem with different assumption as described in section 2.3.

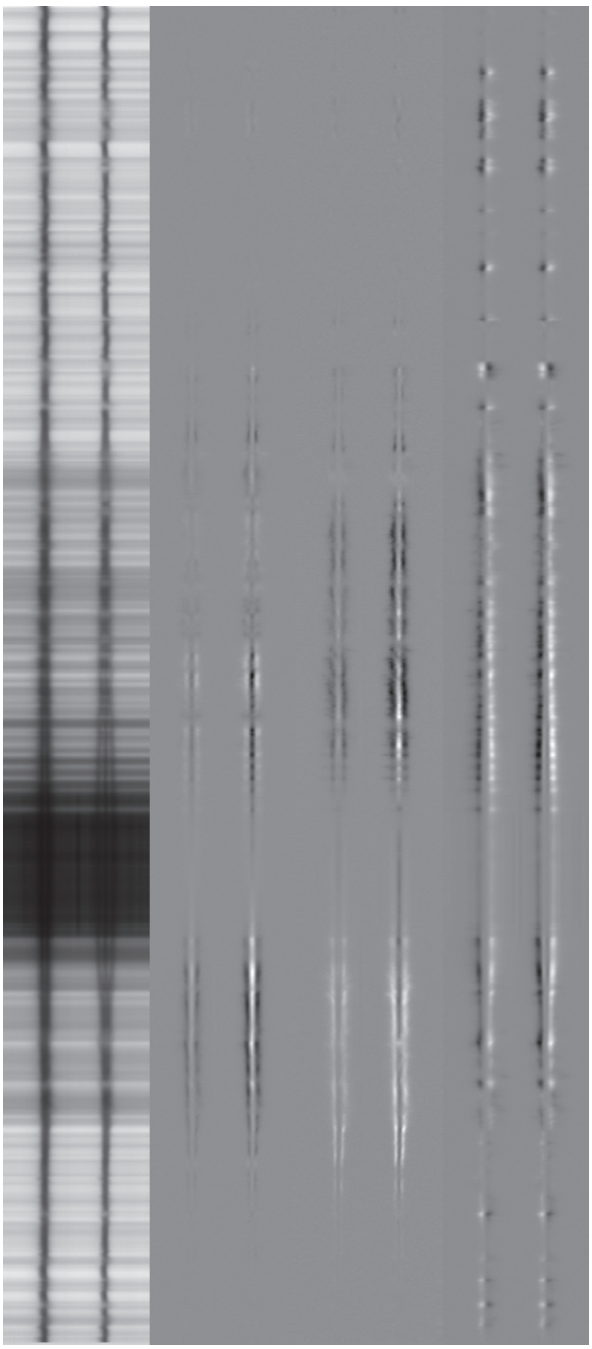

Figure 2.1: Polarization spectra of a sunspot. Four panels show spectral observations of Stokes parameters *I, Q, U, V* characterizing the state of polarization of a narrow range of a spectrum, 630.08 nm $\sim$ 630.32 nm. Courtesy of NAOJ. (http://hinode.nao.ac.jp/)

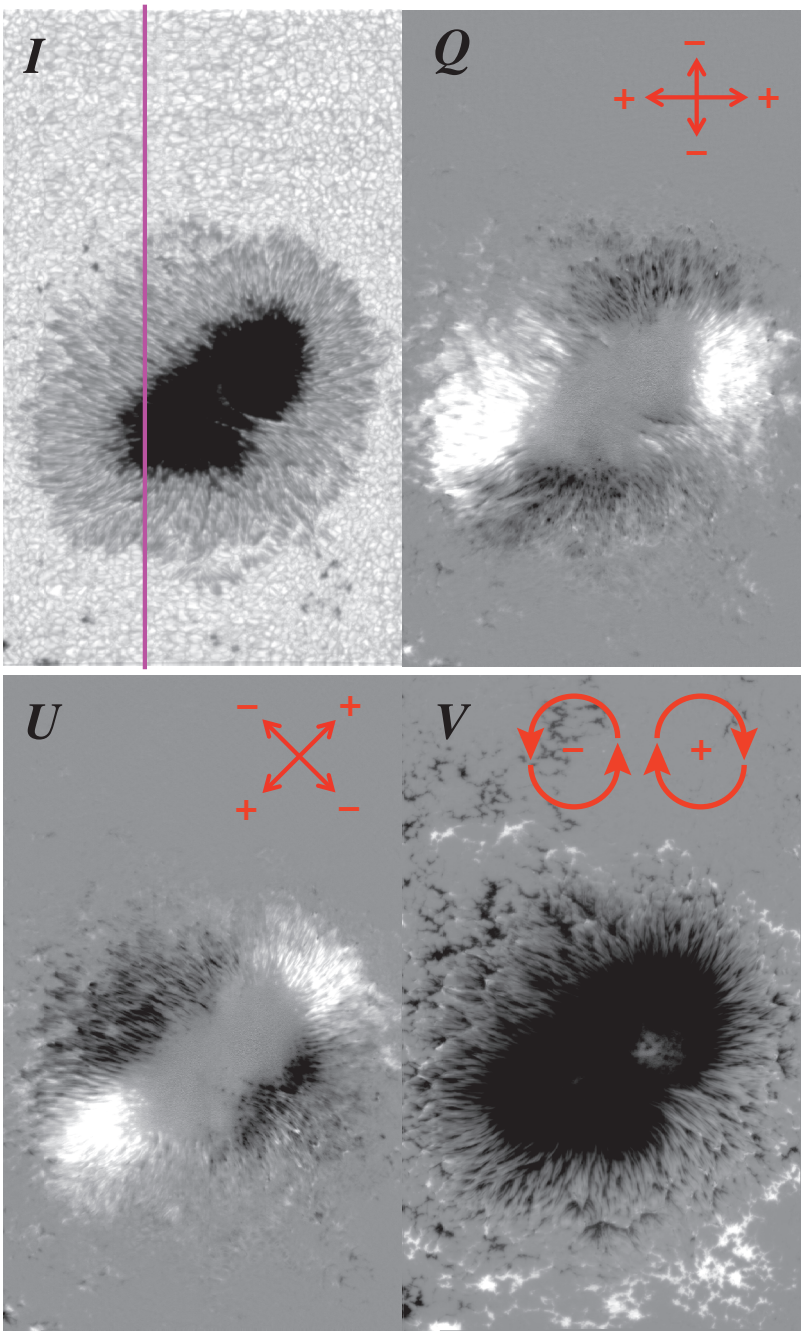

Figure 2.2: Maps of Stokes parameter *I, Q, U, V*. The purple line of left panel indicates the location of the spectra shown in Figure 2.1. Courtesy of NAOJ. (http://hinode.nao.ac.jp/)

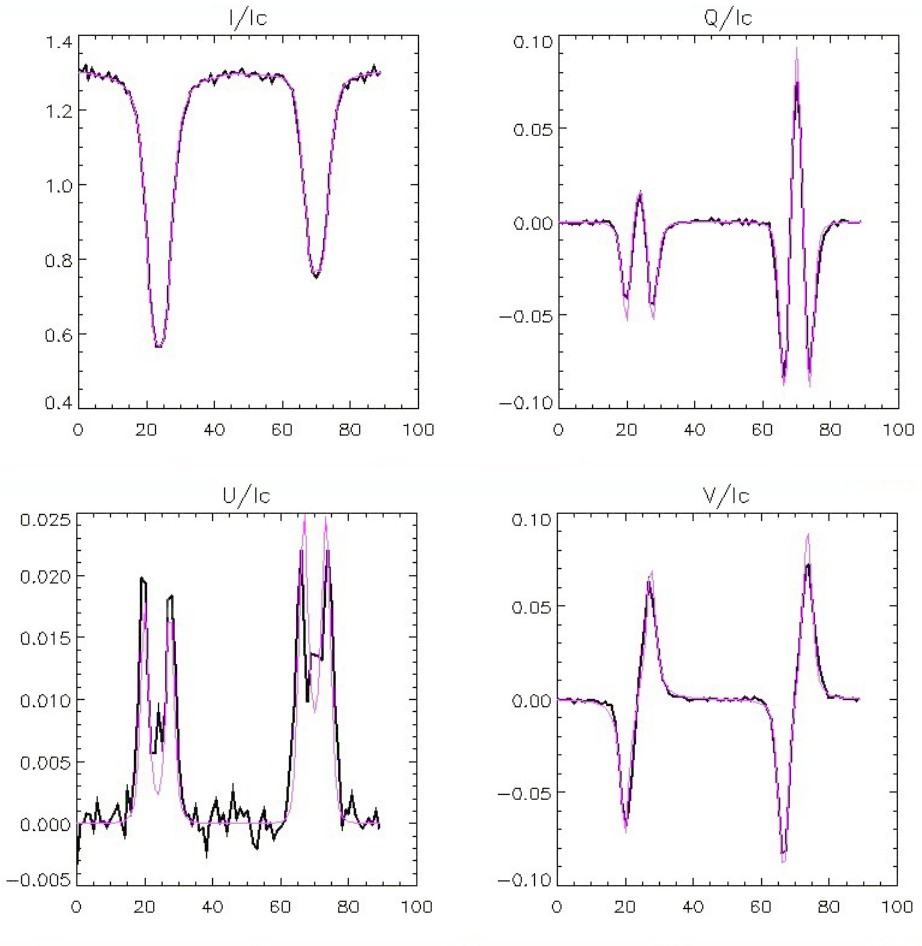

Figure 2.3: Observed polarization profiles (black) and the least-squares fits with Milne-Eddington approximation (purple). The extracted magnetic field parameters are $|B| = 1173$ G, $\theta = 111°$, $\phi = 86°$.

2.2 Milne-Eddington Atmosphere and Least-squares Fitting

We extract information on the vector magnetic fields and thermodynamic parameters from the Stokes profiles by the least-squares fitting to the observed Stokes profiles. The example of a fitting is shown in Figure 2.3. We need a model spectra for given parameters for this purpose. In this section, the magnetic field vectors are represented by the magnetic field strength $|B|$, the inclination angle θ relative to the line of sight, and the azimuth angle ϕ in the plane of the sky relative to a coordinate frame (generally measured counterclockwise from the solar west direction).

Let us condsider the radiative transfer of the polarized light. The model atmo-

sphere is represented as a function of the continuum optical depth τ_c. The Radiation Transfer Equation (RTE, del Toro Iniesta 2003) is given by

$$\frac{d\mathbf{I}}{d\tau_c} = \mathbf{K}(\mathbf{I} - \mathbf{S}), \tag{2.1}$$

where $\mathbf{K}$ is the propagation matrix and $\mathbf{S}$ is the source function vector. If we consider a ray propagating along the Z axis, an Stokes vector is given by the solution of the following equation:

$$\begin{aligned}\frac{\mathrm{d}}{\mathrm{d}z}\begin{pmatrix} I \\ Q \\ U \\ V \end{pmatrix} &= -\begin{pmatrix} \eta_I & \eta_Q & \eta_U & \eta_V \\ \eta_Q & \eta_I & \rho_V & -\rho_U \\ \eta_U & -\rho_V & \eta_I & \rho_Q \\ \eta_V & \rho_U & -\rho_Q & \eta_I \end{pmatrix}\begin{pmatrix} I \\ Q \\ U \\ V \end{pmatrix} \\ &= -\mathbf{K}\begin{pmatrix} I \\ Q \\ U \\ V \end{pmatrix},\end{aligned} \tag{2.2}$$

where η_I, η_Q, η_U, η_V, ρ_Q, ρ_U, and ρ_V are simply the matrix elements. Matrix $\mathbf{K}$ is decomposed into three matrices;

$$\begin{aligned}\mathbf{K} = &\begin{pmatrix} \eta_I & 0 & 0 & 0 \\ 0 & \eta_I & 0 & 0 \\ 0 & 0 & \eta_I & 0 \\ 0 & 0 & 0 & \eta_I \end{pmatrix} + \begin{pmatrix} 0 & \eta_Q & \eta_U & \eta_V \\ \eta_Q & 0 & 0 & 0 \\ \eta_U & 0 & 0 & 0 \\ \eta_V & 0 & 0 & 0 \end{pmatrix} \\ &+ \begin{pmatrix} 0 & 0 & 0 & 0 \\ 0 & 0 & \rho_V & -\rho_U \\ 0 & -\rho_V & 0 & \rho_Q \\ 0 & \rho_U & -\rho_Q & 0 \end{pmatrix}\end{aligned} \tag{2.3}$$

In Equation 2.3, diagonal matrix in the first term corresponds to absorption. The second symmetric matrix corresponds to dichroism. Finally, the third antisymmetric matrix corresponds to dispersion (del Toro Iniesta 2003).

The simplest case is that

$$\mathbf{K}(\tau_c) = \mathbf{K_0}. \tag{2.4}$$

We assume that the souce function vector $\mathbf{S}$, depends linearly on the optical depth,

$$\mathbf{S} \equiv \mathbf{S_0} + \tau_c\mathbf{S_1} = (S_0 + S_1)(1, 0, 0, 0)^T. \tag{2.5}$$

A medium satisfying Equation 2.4 and 2.5 is called *Milne-Eddington* atmosphere

(del Toro Iniesta 2003). The explicit expression of all four Stokes profiles is then

$$\begin{aligned}
I(0) &= \mathbf{S_0} + \Delta^{-1}\eta_I \left(\eta_I^2 + \rho_Q^2 + \rho_U^2 + \rho_V^2\right) \mathbf{S_1}, \\
Q(0) &= -\Delta^{-1}\left[\eta_I^2\eta_Q + \eta_I(\eta_V\rho_U - \eta_U\rho_V) + \rho_Q(\eta_Q\rho_Q + \eta_U\rho_U + \eta_V\rho_V)\right] \mathbf{S_1}, \\
U(0) &= -\Delta^{-1}\left[\eta_I^2\eta_U + \eta_I(\eta_Q\rho_V - \eta_V\rho_Q) + \rho_U(\eta_Q\rho_Q + \eta_U\rho_U + \eta_V\rho_V)\right] \mathbf{S_1}, \\
V(0) &= -\Delta^{-1}\left[\eta_I^2\eta_V + \eta_I(\eta_U\rho_Q - \eta_Q\rho_U) + \rho_V(\eta_Q\rho_Q + \eta_U\rho_U + \eta_V\rho_V)\right] \mathbf{S_1}, \quad (2.6)
\end{aligned}$$

where Δ is the determinant of the propagation matrix; explicitly,

$$\Delta = \eta_I^2\left(\eta_I^2 - \eta_Q^2 - \eta_U^2 - \eta_V^2 + \rho_Q^2 + \rho_U^2 + \rho_V^2\right) - (\eta_Q\rho_Q + \eta_U\rho_U + \eta_V\rho_V)^2. \quad (2.7)$$

Labeling the three components with subscripts "r" (for "red" or "right-handed"), "b" (for "blue"), and "p" (for "principle"), the elements of the propagation matrix are given by

$$\begin{aligned}
\eta_I &= 1 + \frac{\eta_0}{2}\left\{\phi_p \sin^2\gamma + \frac{1}{2}[\phi_\mathrm{b} + \phi_\mathrm{r}](1 + \cos^2\gamma)\right\}, \\
\eta_Q &= \frac{\eta_0}{2}\left\{\phi_p - \frac{1}{2}[\phi_b + \phi_r]\right\}\sin^2\gamma\cos 2\chi, \\
\eta_U &= \frac{\eta_0}{2}\left\{\phi_p - \frac{1}{2}[\phi_b + \phi_r]\right\}\sin^2\gamma\sin 2\chi, \\
\eta_V &= \frac{\eta_0}{2}[\phi_r - \phi_b]\cos\theta, \quad (2.8)
\end{aligned}$$

and

$$\begin{aligned}
\rho_Q &= \frac{\eta_0}{2}\left\{\psi_p - \frac{1}{2}[\psi_b + \psi_r]\right\}\sin^2\gamma\cos 2\chi, \\
\rho_U &= \frac{\eta_0}{2}\left\{\psi_p - \frac{1}{2}[\psi_b + \psi_r]\right\}\sin^2\gamma\sin 2\chi, \\
\rho_V &= \frac{\eta_0}{2}[\psi_r - \psi_b]\cos\theta, \quad (2.9)
\end{aligned}$$

where the angles γ and χ are the inclination angle of the magnetic field vector with respect to the LOS and the azimuth angle of the magnetic field vector, respectively. The absorption and dispersion profiles in equation 2.8 and 2.9 become

$$\phi_\delta(u_0, a) = \frac{1}{\sqrt{\pi}} H(u_0 + \delta u_B - u_{LOS}, a) \quad (2.10)$$

and

$$\psi_\delta(u_0, a) = \frac{1}{\sqrt{\pi}} F(u_0 + \delta u_B - u_{LOS}, a), \quad (2.11)$$

where δ is "-1", "0" or "+1", that are noted in Equations 2.8 and 2.9 with "r", "p" or "b", respectively. The u_0, u_B and u_{LOS} are represented by

$$u_0 \equiv \frac{\lambda - \lambda_0}{\Delta\lambda_D}, \tag{2.12}$$

$$u_B \equiv \frac{\lambda_B}{\Delta\lambda_D} = \frac{4.67 \times 10^{-13}\lambda_0^2 B}{\Delta\lambda_D}, \tag{2.13}$$

and

$$u_{LOS} \equiv \frac{v_{LOS}\lambda_{0,\alpha}}{c\Delta\lambda_D}, \tag{2.14}$$

where λ_0 is the wavelength in the absence of the magnetic field vector, and B is the magnetic field strength, $\Delta\lambda_D$ is the Doppler width of a line, u_{LOS} is the Doppler velocity to line of sight, and $\alpha = +1, 0, -1$. The right-handed circular component ($\delta = -1$) is shifted to the red (longer wavelengths) and the left-handed circular component ($\delta = +1$) to blue (shorter wavelengths). The linearly polarized componen ($\delta = 0$) in the directions of magnetic fields is unperturbed from the original position in the absence magnetic field. The Voigt function H and Faraday-Voigt function F in Equations 2.10 and 2.11 are given by

$$H(u, a) \equiv \frac{a}{\pi} \int_{-\infty}^{\infty} e^{-y^2} \frac{1}{(u-y)^2 + a^2}\, dy, \tag{2.15}$$

and

$$F(u, a) \equiv \frac{1}{\pi} \int_{-\infty}^{\infty} e^{-y^2} \frac{u-y}{(u-y)^2 + a^2}\, dy, \tag{2.16}$$

where a is the damping coefficient from the central wavelength of a line.

The solution (Equation 2.6) of the RTE in a Milne-Eddington atmosphere is known as the Unno-Rachkovsky solution, and is very useful because of its analytical character (del Toro Iniesta 2003). By changing parameters, we can obtain an approximate idea of how spetral lines is formed in different atmospheres. Ten parameters are needed to characterize the Stokes profiles (Table 2.1).

Table 2.1: Ten parameters to fit to the Stokes profiles (*I, Q, U, V*), using the *Milne-Eddington* atmosphere model.

Line-to-continuum absorption coefficient ratio	η_0
Magnetic field strength	$\|B\|$
Doppler velocity to line of sight	v_{LOS}
Doppler width of a line	$\Delta\lambda_D$
Damping coefficient (in unit of $\Delta\lambda_D$) from central wavelength of a line	a
Azimuth of magnetic field vector	χ
Inclination of magnetic field vector	γ
Filing factor (occupation rate of magnetic field per unit pixel)	f
Source function	S_0, S_1

2.3 Analysis

Tsuneta et al.(2008a) found with *Hinode* (Kosugi et al. 2007) that there are patchy concentrations of magnetic fields with field strengths exceeding 1 kG in the polar region, confirming the result of (Okunev and Kneer 2004). These magnetic fields are almost *vertical* to the local surface of the Sun. Ubiquitous magnetic concentrations with field strengths larger than 1 kG are known to exist in the quiet Sun as well (e.g., Orozco Suárez et al. 2007a). This paper focuses on determining whether there is any difference in the magnetic properties between the polar region and the quiet Sun. If there is a difference, what is the implication to the problems of solar dynamo and the acceleration of the fast solar wind? With this motivation, we observed the polar region and the quiet Sun as a fiducial data for the analysis of the polar region with the spectropolarimeter (SP; Lites et al. 2001) of the Solar Optical Telescope (SOT; Tsuneta et al. 2008a; Ichimoto et al. 2008; Shimizu et al. 2008) aboard *Hinode*.

The sensitivity to a given magnetic field vector depends on its orientation with respect to the observer and on the Stokes parameter used to detect it. Stokes Q and U signals are used to detect the field component perpendicular to the LOS, while Stokes V signal is used for the field component parallel to the LOS. Measurement through Stokes V is more sensitive than that through Stokes Q and U when the field is weak. We observed the quiet Sun located at the East limb instead of the quiet Sun at the disk center, so that the sensitivity to detect any weak magnetic field is the same for both the polar region and the quiet Sun. This allows a direct comparison between the polarimetric data for the polar region with that for the quiet Sun.

Hinode observed the North polar region of the Sun on 2007 September 25, when the North pole was located 7° inside the visible disk. The SP observed a field of view (FOV) of $320'' \times 163''.84$ in a very deep map mode (exposure time: 12.8 s). The SP records the Stokes spectral profiles (I, Q, U and V) of $\mathrm{Fe_I}$ 630.15 nm and 630.25 nm with a wavelength sampling of 2.15 pm pixel^{-1} and with a scan step of $0''.16$.

A least-squares fitting was applied to the Stokes spectra with the Milne−Eddington inversion of the Polarized Spectra (MILOS) code (Orozco Suárez and del Toro Iniesta 2007). The 10 free parameters are the three components describing the vector

magnetic field (strength B, inclination angle γ, and azimuth angle χ defined in Figure 2.7), the LOS velocity, two parameters describing the source function, the ratio of line-to-continuum absorption coefficient, the Doppler width, the damping parameter, and the stray-light factor α. A nonzero stray-light factor α may be interpreted as a parameter that represents both the filling factor of a nonmagnetized atmosphere along the line of sight and the stray-light contamination. The stray-light profile is evaluated individually for each pixel as the average of the Stokes I profiles observed in a $1''$ wide box centered on the pixel (Orozco Suárez et al. 2007b). This arrangement also allows us to accurately estimate the stray-light profiles of rapidly changing continuum intensity toward the limb.

To minimize the influence of noise leading to unreliable inversions, we analyze only pixels whose linear or circular polarization signal amplitudes exceed a given threshold above the noise level σ. The noise level σ is determined in the continuum wavelength range of the Stokes Q, U and V profiles. The noise level σ is given by $\sigma = \sqrt{\sum_i (V_i - \overline{V})^2/n}$, where V_i is the intensity of the Stokes V profile at continuum wavelength pixel i, $\overline{V}$ is the average Stokes V signal for the same wavelength range, and n is the number of wavelength data points. σ/I_c depends on the exposure time, where I_c is the continuum intensity, and is 0.0008 for the observation of the North polar region.

The fitting was performed for pixels whose Q, U or V peak is larger than $5\sigma/I_c$. The derived maps still contain pixels with physically unacceptable values. If there is a strong spike on top of the noisy Stokes profiles (due to Poisson fluctuation and cosmic-ray hits) exceeding the threshold, that pixel will pass the 5σ criteria. This is the reason why we cannot completely remove the bad pixels. Thus, we employ an additional filter to further remove the influence of the noise. We improved the statistics of the Stokes profiles by summing across 2 pixel in wavelength and then removed the pixels whose Q, U or V peak in the summed profiles is lower than $5\sigma/I_c$. All the good profiles that have passed the previous threshold should pass this criterion too: only the noisy profiles with high spike which have cheated the prior filter can be potentially removed in this stage. Note that we use the original Stokes profiles (not summed) for inversion.

Furthermore, we remove pixels with the absolute value of the Doppler velocity

higher than 10 km s^{-1} or the filling factor less than 0.01. Analysis of several samples indicates that the Stokes profiles of such pixels are not fitted well. The velocity of the horizontal flow due to granular motion observed with SOT/SP is smaller than 9 km s^{-1} (Bellot Rubio 2009), and the threshold of 10 km s^{-1} employed here is above this value. If the stray-light contamination is negligible, the filling factor of the magnetic atmosphere will be given by $f = 1 - \alpha$ (Orozco Suárez et al. 2007b). Tsuneta et al.(2008a) reported that the distribution of the filling factor f has a broad peak at $f = 0.15$ with FWHM range $0.05 < f < 0.35$ for another polar region, and the threshold given above for the filling factor is located far away from the typical range. Even if we erroneously remove valid pixels with this filter, the effect of the erroneous removal would be negligible, since the total number of pixels removed with this particular process is only 1.7% of the total number of pixels that passed the previous two criteria. A total of 21.0% of the pixels pass all the thresholds.

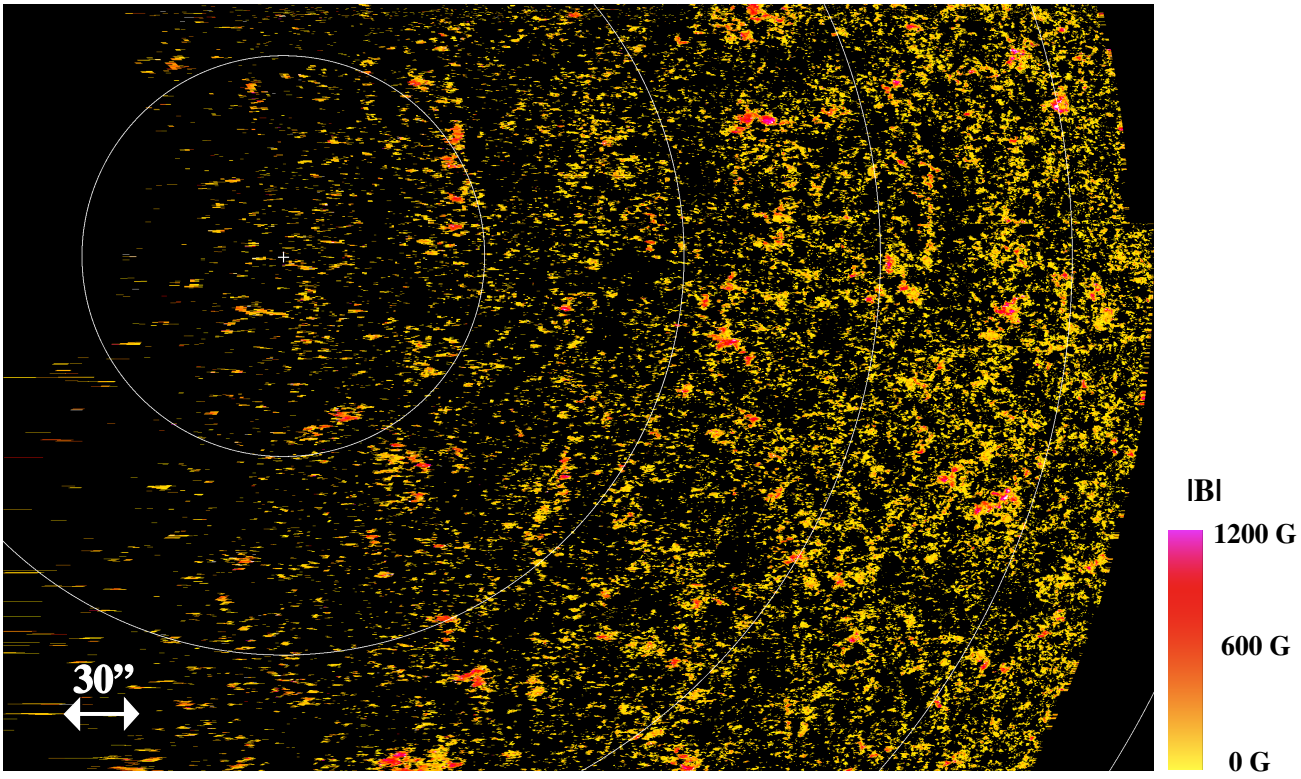

Figure 2.4: The map of signed strength of the magnetic field vectors classified as *vertical* (see section 2.4.1); the map of the magnetic field signed strength on the sky plane is converted to the map seen from above the North pole. The observations took place at 00:10—07:26 UT on 2007 September 25. North is to the left. The pixel size is 0″.16. The magnetic field strengths were obtained only for pixels whose polarization signal exceeds a given threshold (see the text). The size of the FOV for the east-west dierction is 320″. The size of the FOV for the North-South direction (163″.84) is expanded to 477″.6 as a result of correction for foreshortening. The circular arc is the latitudinal line per 5° from the North pole.

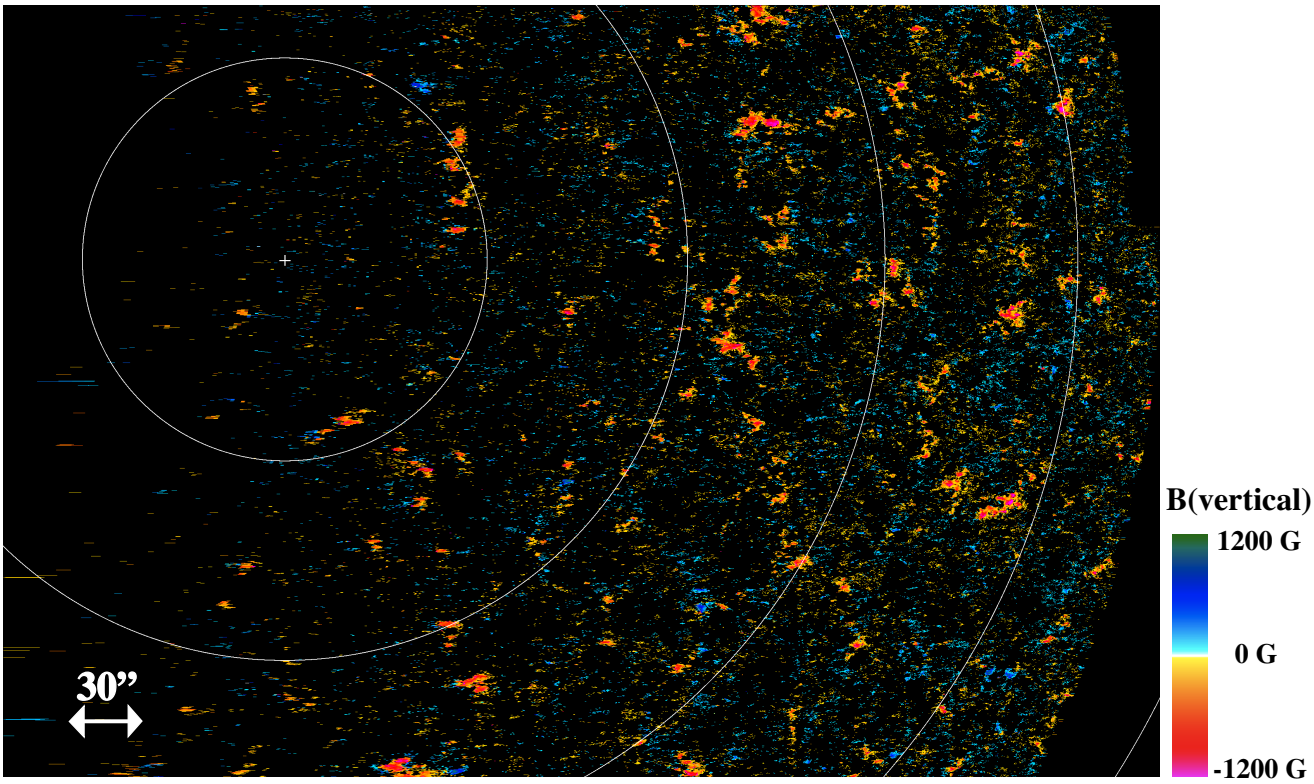

Figure 2.5: Map of signed strength of the magnetic field vectors classified as *vertical* in the polar region. The original data is the same as that of Figure 2.4. The pixel size is 0″.16. The magnetic field strength was obtained only for pixels whose polarization signal exceeds a given threshold (see the text). These panels can be directly compared with the quiet-Sun maps (Figure 2.10). The scale size and the color table for these maps are the same.

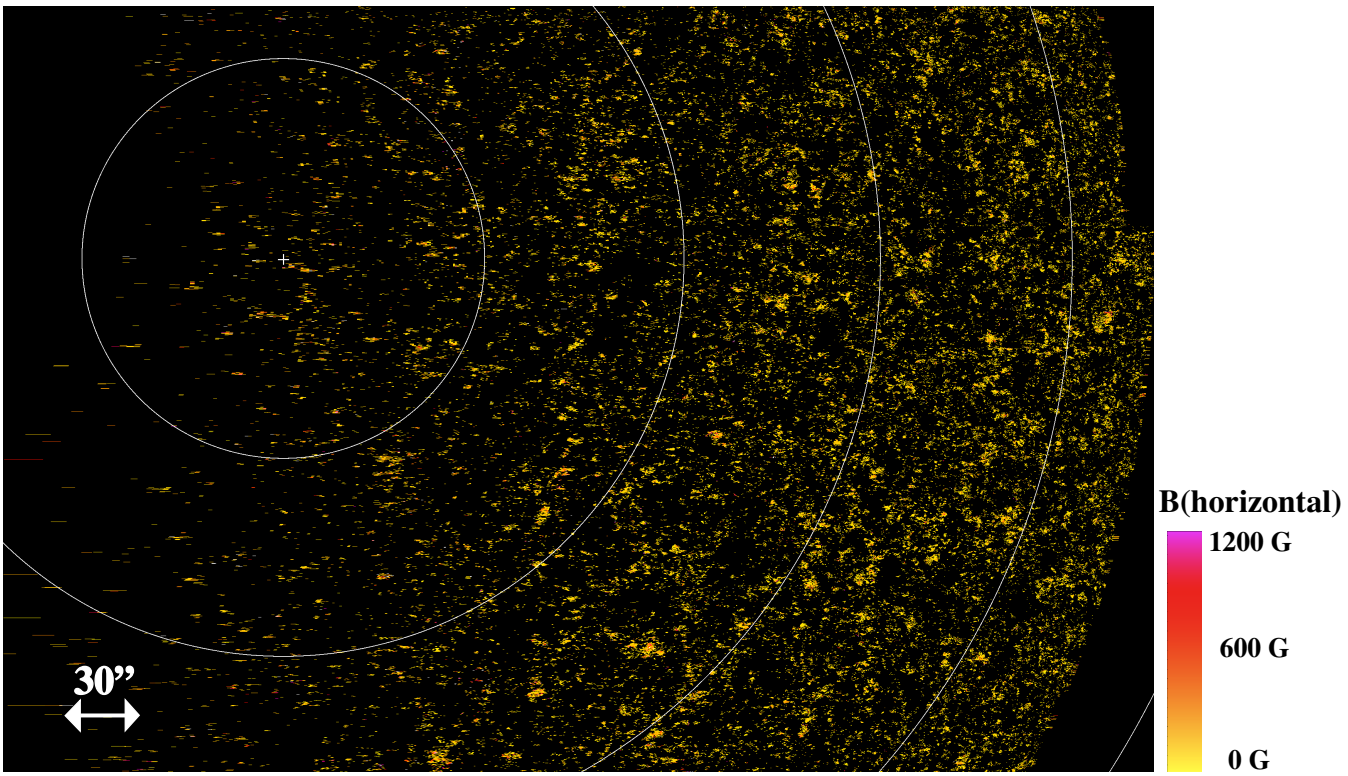

Figure 2.6: Map of the field strength of magnetic field vectors classified as *horizontal*. The scale size and the color table for these maps are the same as Figure 2.5.

2.4 North Polar Region

Figure 2.6 shows a map of the magnetic field strength as seen from just above the North pole. Such a polar projection is needed to correctly see the spatial extent and size distribution of magnetic patches in the polar region. Note that at a higher latitude the spatial resolution in one direction is compromised due to the projection effect. Large patches correspond to the kilo-Gauss (kG) magnetic fields with the fanning-out structure (Tsuneta et al. 2008a).

2.4.1 Vertical and Horizontal Magnetic Fields

The inclination (zenith) angle of the magnetic field vector with respect to the local normal has a wide distribution with two peaks around the local vertical and the local horizontal directions (Orozco Suárez et al. 2007a; Ishikawa and Tsuneta 2009). Since we are interested in any difference between the polar region and the quiet Sun, and the resulting consequence in the coronal magnetic fields, we obtain the zenith angle i of the magnetic field vector. Due to the 180° ambiguity in the direction of the magnetic field vector projected onto the sky plane, there are two solutions i_1 and i_2 ($0 \leq i_1 \leq \pi$, $0 \leq i_2 \leq \pi$; Figure 2.7) given by

$$i_1 = \arccos\{\cos\gamma\cos\theta + \sin\gamma\sin\theta\cos(\beta - \chi)\}, \tag{2.17}$$

$$i_2 = \arccos\{\cos\gamma\cos\theta + \sin\gamma\sin\theta\cos(\pi - (\beta - \chi))\}, \tag{2.18}$$

where θ is the angle between the local normal and the LOS and is given by $\theta = \cos^{-1}(\cos\delta\cos\varphi)$, where δ and φ are heliographic latitude and longitude for a pixel, respectively, γ is the inclination of the magnetic field vector with respect to the line of sight ($0 \leq \gamma \leq \pi$), and χ is the azimuth angle ($0 \leq \chi \leq \pi$). The β angle ($0 \leq \beta \leq \pi$) is defined in Figure 2.7 and is given by $\beta = \cos^{-1}(\cos\delta\sin\varphi/\sin\theta)$.

We now introduce one assumption that the magnetic field vector is either *vertical* or *horizontal* to the local surface (or undetermined). The zenith angle is defined to be from 0° to 40° and from 140° to 180° for the *vertical* magnetic field. The zenith angle of the *horizontal* field is defined to be between 70° and 110°, following (Ishikawa and Tsuneta 2009). Magnetic field vectors with an inclination angle between 40° and 70° are not used in the subsequent analysis. According to this definition, every pixel has magnetic field vector classified as either *vertical* or *horizontal* (or undetermined).

Figure 2.8 shows the scatter plots of the two solutions i_1 and i_2 for the zenith angle. If both the solutions are vertical, the one closer to the local normal is taken. In case one solution is vertical and the other horizontal, it is not possible to distinguish one from each other. Pixels with those solutions are not used. If one of the solutions is either vertical or horizontal and the other solution is neither vertical nor horizontal, we will choose the solution of either vertical or horizontal. In addition, the kG-patches with quasi-symmetric fanning-out structure allows us to manually correct the zenith angle by visually inspecting the thus-determined zenith angle map.

There is concentration of pixels (about 3% of the pixels) along the white line of $i_1 \sim i_2$ in Figure 2.8. These pixels along the line have only valid Stokes V signal without Stokes Q and U signals. The inversion code correctly produces either $\gamma \sim 0$ or $\gamma \sim \pi$ for these pixels, so that $i_1 \sim i_2$ from Equations 2.17 and 2.18. There is a gap in population around the line $i_1 + i_2 \sim \pi$. If the inclination angle with respect to the line of sight is $\gamma \sim \pi/2$, i.e. the magnetic field vector is on the sky plane, it turns out that $i_1 + i_2 \sim \pi$ from Equations 2.17 and 2.18. There may be two reasons for the gap; (1) The noise in Stokes V makes the derived magnetic vector impossible to reach an inclination of 90° (ie. the sky plane). (2) Stokes V is much more sensitive than Stokes Q and V for weak magnetic field strength, so that the magnetic field vectors tend to deviate the sky plane.

It is possible to check the consistency of the 180° ambiguity resolution done here with the information on the sign of the Stokes V signal (Tsuneta et al. 2008a). We compare the polarity of the magnetic field vectors classified as *vertical* shown in Figure 2.5 with the Stokes V map such as the one shown in Figure 2 of (Tsuneta et al. 2008a) and confirm that 96% of the pixels shown in Figure 2.5 have the correct sign indicated by the polarity of the Stokes V signal. In particular, we confirm that all the apparent kG-patches have the correct sign. This indicates that the assumptions and the rules employed to classify the *vertical* and *horizontal* magnetic field vectors are valid.

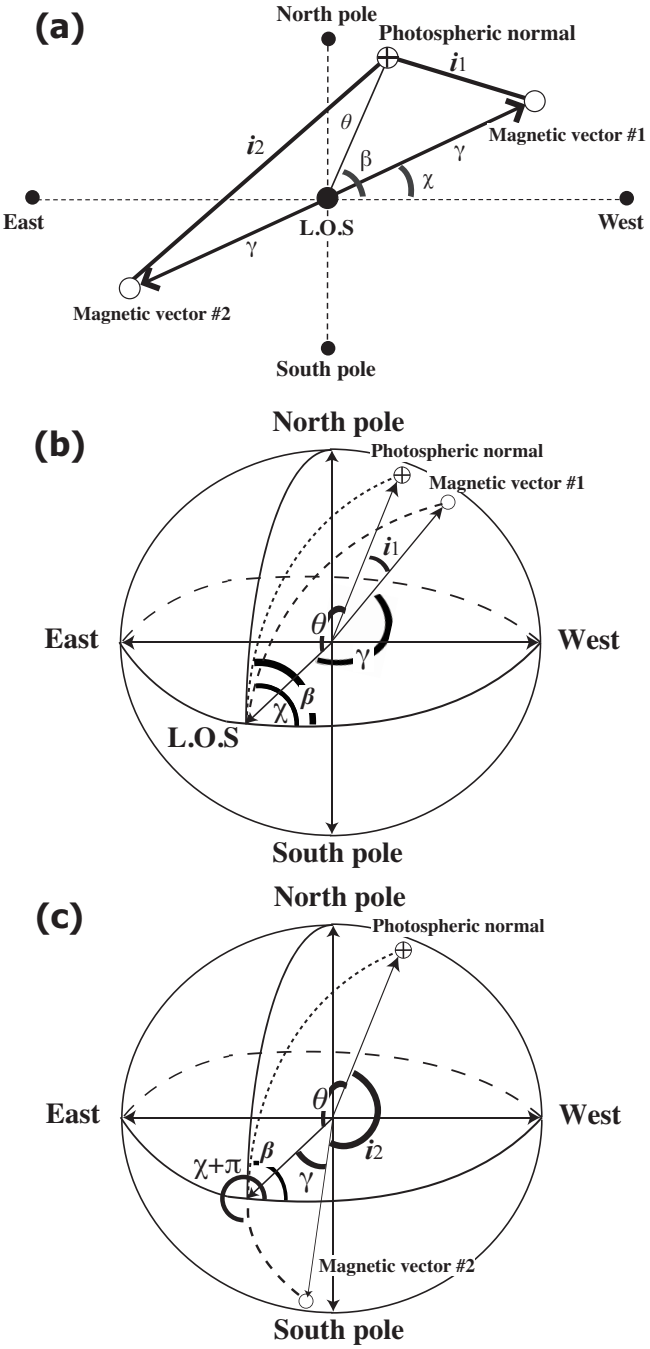

Figure 2.7: Two solutions of the magnetic field vectors ♯1 and ♯2 with the inclination angles of i_1 and i_2 with respect to the photospheric normal for the two possible azimuth angles of χ and $\chi + \pi$ due to the 180° ambiguity, respectively. θ is the angle between the local normal and the LOS, γ the inclination ($0 \leq \gamma \leq \pi$) of the magnetic field vector with respect to LOS, and χ is the azimuth angle ($0 \leq \chi \leq \pi$). Panel (a) shows these angles on the sky plane. Note that the lines indicating angles are represented by the straight lines, not by the segments of arc, for simplicity. Panel (b) indicates the same information in terms of vectors at the position of any observing pixel. The dotted and dashed lines represent Great circles connecting the LOS direction and the photospheric normal and the magnetic vector ♯1, respectively. Panel (c) is the same as panel (b) but for the magnetic vector ♯2. These two representations shown in the panel (a) and panels (b) and (c) are equivalent.

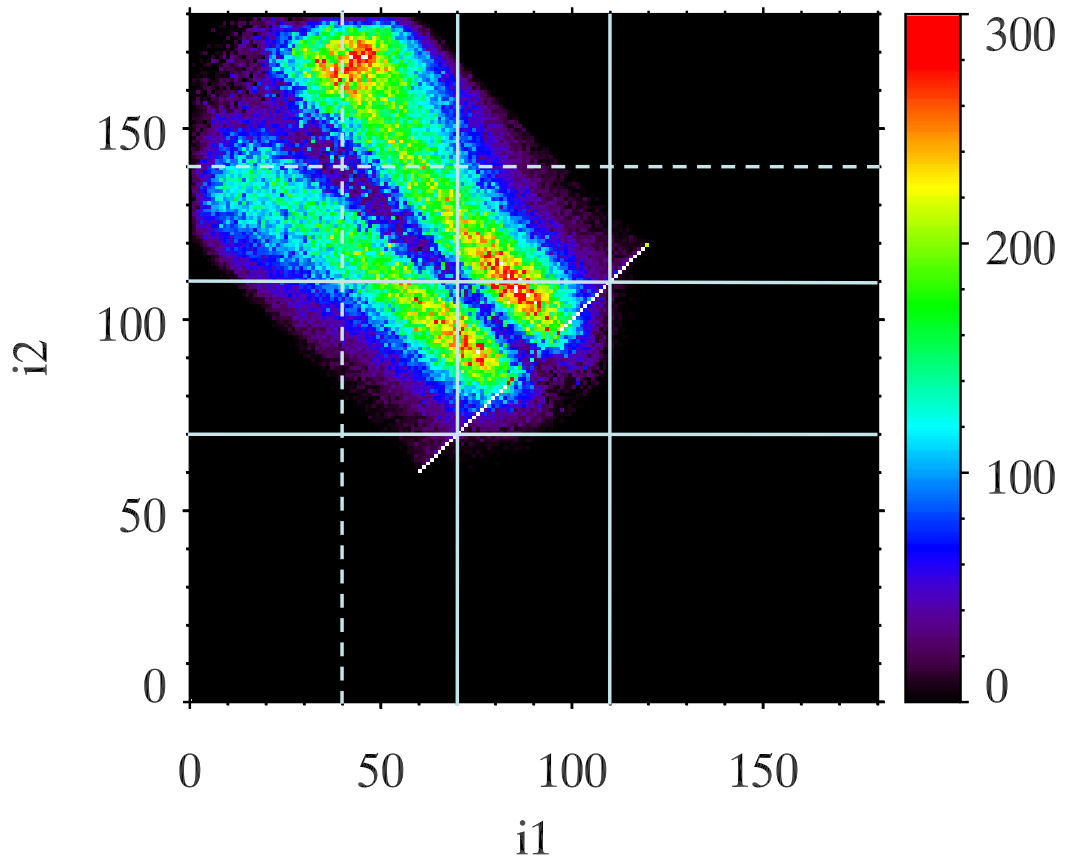

Figure 2.8: Scatter plot of the two solutions i_1 and i_2 of the inclination angles with respect to the local normal to the photosphere for the North pole. The color table indicates the density of the data points per $1° \times 1°$. Magnetic fields are classified as *vertical* to the local surface if they are located either close 0° or 180° (dashed lines) and as *horizontal* if located near 90° (bold lines). For the concentration along the line $i_1 \sim i_2$ as indicated by the white line, see the text.

2.4.2 Configuration of Magnetic Fields in the North Polar Region

Two maps of the strengths of the magnetic field vectors classified as *vertical* and *horizontal* for the North polar region are shown in Figure 2.5 and 2.6. Comparison of Figure 2.4 with two panels of Figure 2.5 and 2.6 shows that the vertical and horizontal magnetic fields are well decoupled: For instance, we do not see any inclined fanning-out structure around the magnetic concentrations of the vertical magnetic fields in the map of the horizontal magnetic fields due to the separation band prepared in between the vertical and horizontal zones in the inclination of the magnetic field vectors.

As for the vertical magnetic fields, almost all the large patches have the same polarity, while both polarities exist for the smaller patches. There appears to be more mixed polarities in lower latitude, while the region in higher latitude is dominated by negative kG patches. The horizontal magnetic fields appear to be much more uniform in size and in spatial distribution as compared with the vertical magnetic fields.

2.5 Quiet Sun at the East Limb

The quiet Sun at the East limb was observed on 2007 November 28 using the SOT/SP in the very deep map mode. The exposure time is 12.8 s, which is the same as that of the polar observation. We confirm with that there is no coronal activity (enhanced brightness) in the region with the data from the X-ray telescope (XRT) aboard *Hinode* . The σ/I_c for the quiet Sun at the East limb is 0.0008. The signal-to-noise ratio is the same as that for the North polar region, simply because the exposure time and the observing mode for the two observations are the same. The size of the FOV was $100''(\text{east} - \text{west}) \times 162''.84(\text{North} - \text{South})$. As we did for the North polar region, a least-squares fitting is applied to the Stokes spectra with the MILOS code. Figure 2.9 shows the map of the magnetic field strength as seen from just above the East limb to allow us to compare the spatial extent and size distribution of magnetic patches in the quiet Sun and the polar region. In the region closer to the limb, the spatial resolution in one direction is reduced due to the projection effect just like in the North pole region. Similarly, there are two solutions of the zenith angle for the magnetic field vectors. We have followed the same assumptions that were employed for the North pole. Two maps of the strengths of the magnetic field vectors classified as *vertical* and *horizontal* are shown in Figure 2.10.

The spatial distribution of the vertical magnetic fields at the East limb appears to be different from those in the North pole. The map of the quiet Sun shows the mixture of magnetic patches with both polarities. The magnetic concentrations at the East limb are apparently smaller in size than those at the North pole. The number of the patches is also smaller in this particular quiet-Sun region. In contrast, the horizontal magnetic fields of the two regions appear to be strikingly similar.

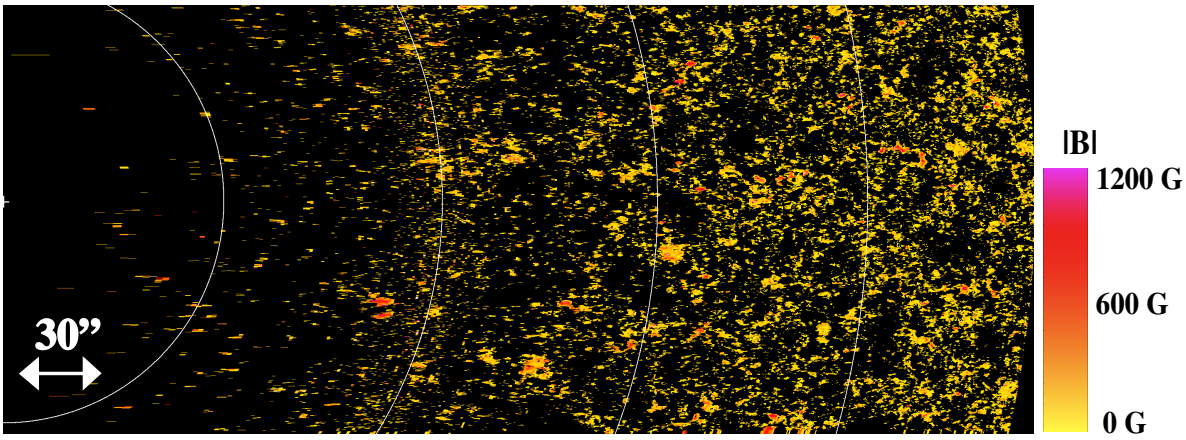

Figure 2.9: Magnetic landscape of the quiet Sun near the East limb; the map of the magnetic field strength on the sky plane is converted to the map seen from above the East limb. The observations are done at 21:00—23:16 UT on 2007 November 28. North is up. The pixel size is 0″.16. The field of view is 100″ (the east−west) by 162″.84 (North−South). The size of the FOV for east−west direction (100″) is expanded to 397″.6 as a result of correction for foreshortening. The circular arc is the latitudinal line per 5° from the East limb. The magnetic field strengths were obtained only for pixels whose polarization signal exceeds a given threshold (see the text). This figure can be directly compared with the polar map (Figure 2.4). The scale size and the color table for these maps are the same.

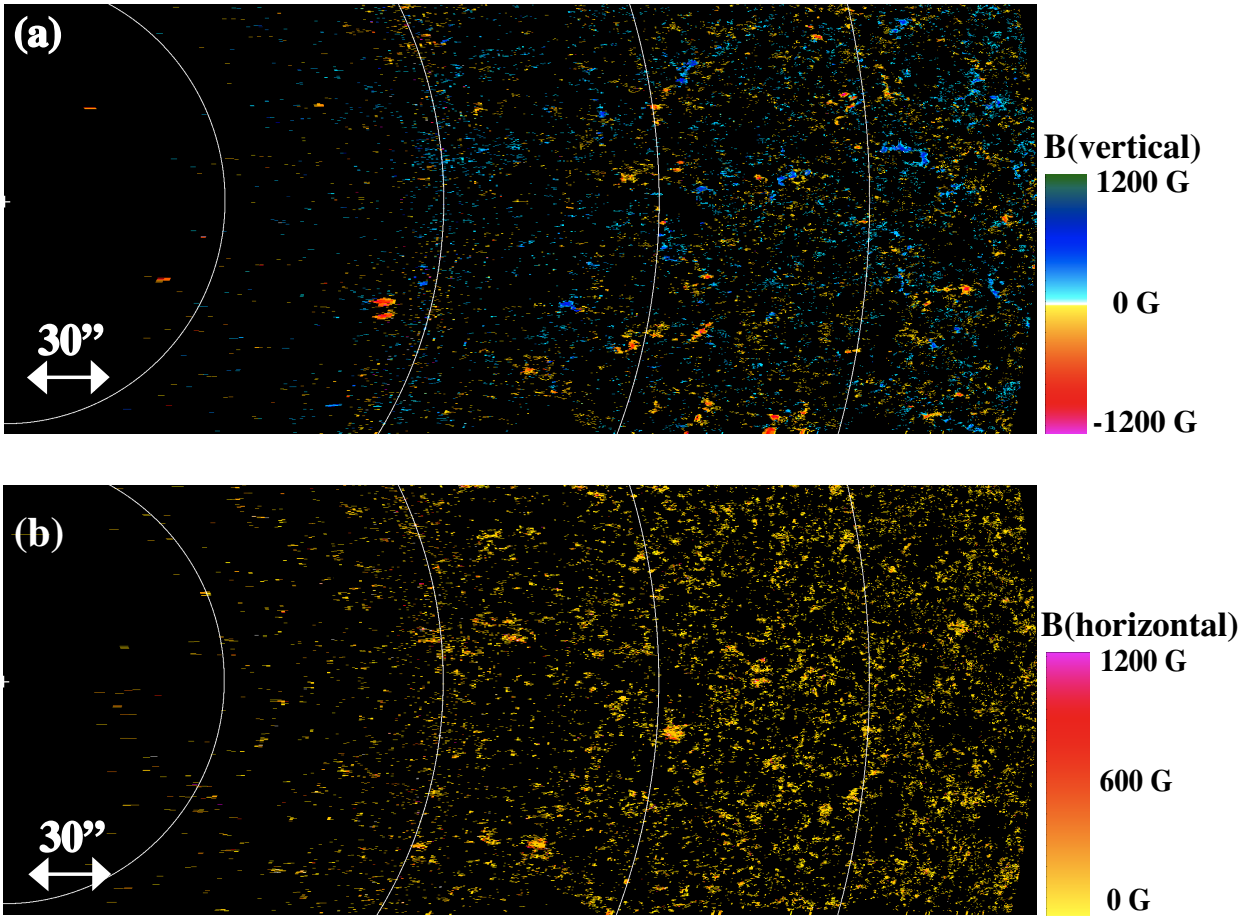

Figure 2.10: (a) Map of signed strength of the magnetic field vectors classified as *vertical* near the East limb. (b) Map of strength of the magnetic field vectors classified as *horizontal* near the East limb. The original data are the same as that of Figure 2.9. The pixel size is $0''.16$. The magnetic field strengths were obtained only for pixels whose polarization signal exceeds a given threshold (see the text). These panels can be directly compared with the polar maps (Figure 2.5). The scale size and the color table for these maps are the same.

Chapter 3

Comparison between the Polar Region and the Quiet Region of the Sun

3.1 Kilo-Gauss Magnetic Patches

Figures 3.1 and 3.2 show arbitrarily chosen kG-patches in the North polar region and in the quiet Sun at the East limb. These patches are located between 0° and 23° from the pole and the East limb. We notice complex internal structures of the kG-patches (Okunev and Kneer 2004, 2005). Histograms of the magnetic field strengths for the two regions are apparently different. The magnetic concentrations in the polar region have an enhancement at around 800 G, while in the quiet Sun such deviations are not apparent. The statistics is poor in the quiet Sun, and this could be the reason why no deviation is seen. The intrinsic magnetic field strengths are at their maximum value around the center of the kG-patches, and decrease toward the edge. Likewise, the filling factors essentially reach a maximum around the center of the kG-patches and decrease toward the edges. The true areas, the maximum magnetic field strengths, and the average field strengths of each kG-concentration shown in Figures 3.1 and 3.2 are shown in Table 3.1 (from 1 to 5).

To investigate the properties of typical large kG-patches, we chose additional five large patches at latitudes between 75° and 90° in the North polar region (Figure 2.5). These are added to Table 3.1 (from 6 to 10). (In total, we have 10 data sets.) The average maximum intrinsic magnetic field strength is 1600 G, and the average intrinsic magnetic field strength is 500 G. The average area is about $2.3 \times 10^{17}\mathrm{cm}^2$. The total magnetic flux of a kG-patch is estimated with $\sum B_j \cos i_j f_j s_j$, where B_j,

i_j and f_j are the intrinsic magnetic field strength, the inclination angle obtained with Equations 2.17 and 2.18, and the filling factor of the j-th SOT pixel inside the kG-patch, respectively, and s_j is the pixel size. Average magnetic flux of the 10 large patches in the polar region is 2.0×10^{19} Mx per patch. These fluxes estimated here and below are the minimum values in the sense that the sizes of the patches are determined with the 5σ threshold.

We also include additional five large patches located in the belt between 67° to 90° (Figure 2.10) in the quiet Sun at the East limb (Table 3.1, from 6 to 10). The average maximum intrinsic magnetic field strength is 1200 G, and the average intrinsic magnetic field strength is 400 G. The average area is 6.9×10^{16}cm^2. Average magnetic flux of the 10 large patches in the quiet Sun is 4.2×10^{18} Mx per patch. The intrinsic magnetic field strengths of the polar magnetic patches are larger than those of the quiet Sun. The average area and the total magnetic flux have considerable difference between the two regions: kilo-Gaussj magnetic concentrations in the polar region have a factor of 3.3 larger average area and have a factor of 4.8 larger magnetic flux than those in the quiet Sun.

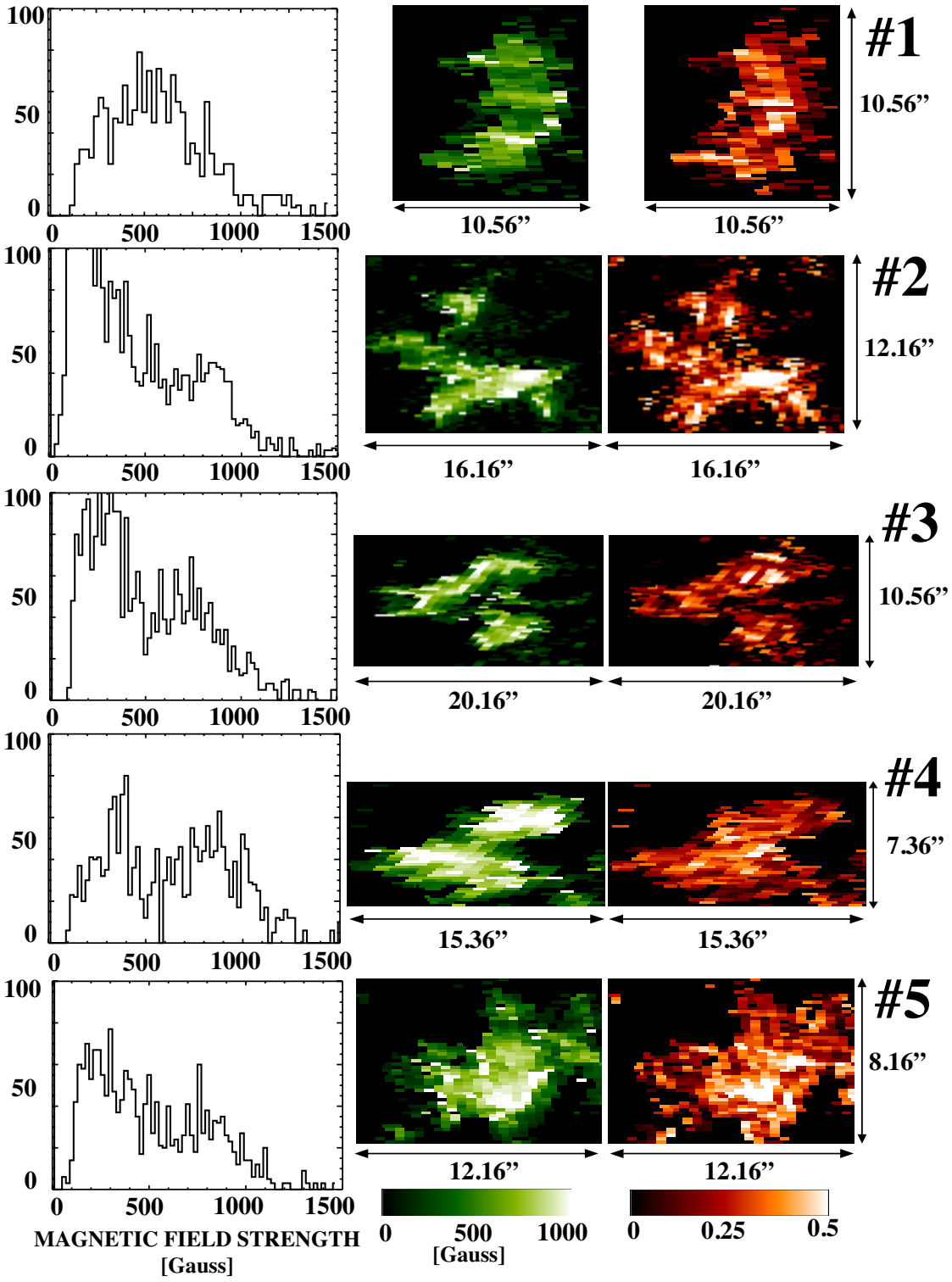

Figure 3.1: Data from the kG magnetic concentrations arbitrarily chosen in the North polar region (Figure 2.4); the histograms of intrinsic magnetic fields strength (left), maps of intrinsic magnetic field strength (center) and the filing factor (right) seen from above the pole. The pixel size of the maps is $0''.16$.

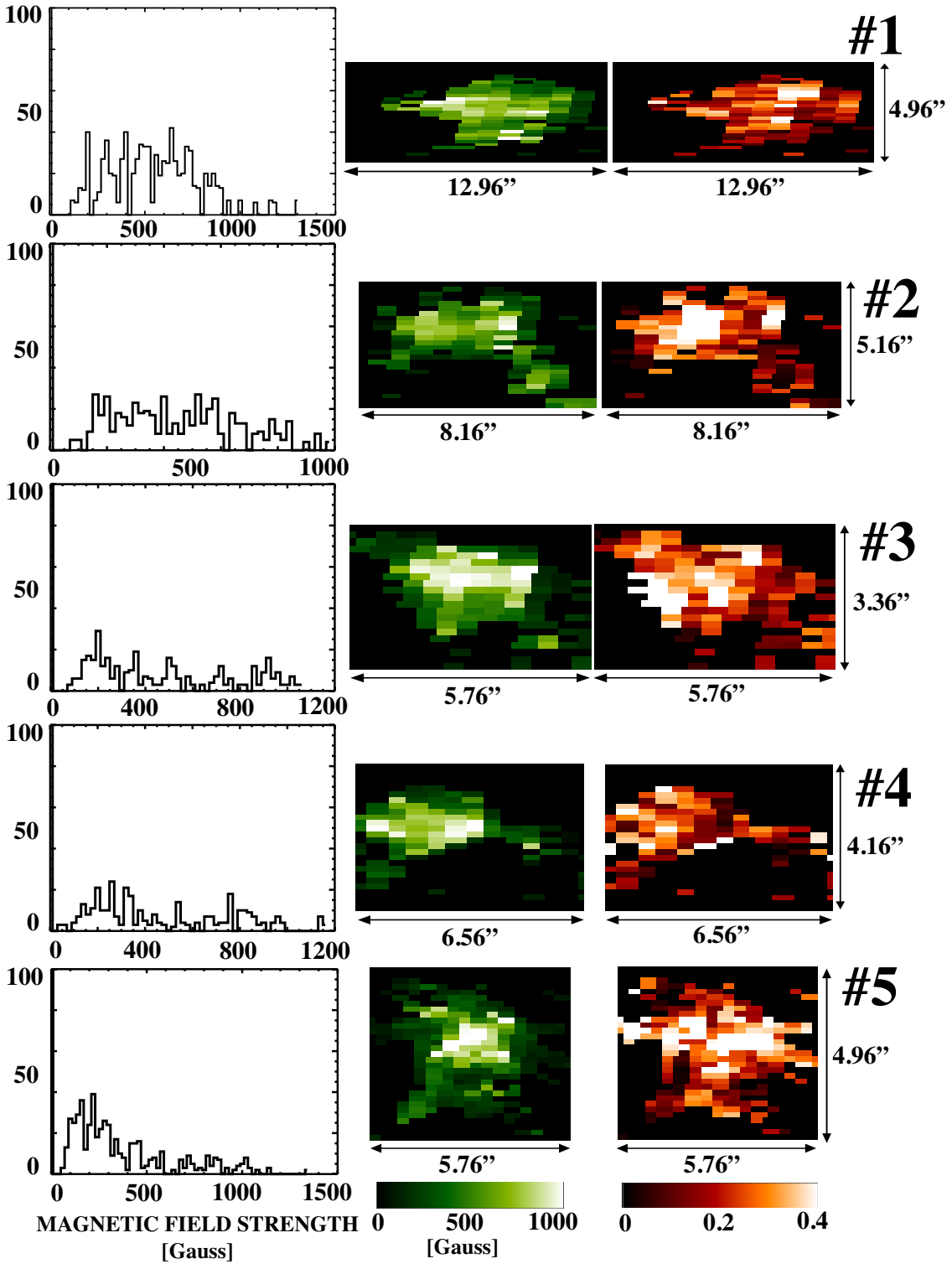

Figure 3.2: Data from the kG magnetic concentrations arbitrarily chosen in the quiet Sun (Figure 2.9); the histograms of intrinsic magnetic fields strength (left), maps of intrinsic magnetic field strength (center) and the filing factor (right) seen from above the East limb. The quiet Sun has the kG-patches with both positive and negative magnetic polarities, and the absolute intrinsic magnetic field strengths are shown. The pixel size of the maps is $0''.16$.

Table 3.1: Properties of kG-patches

Number	Area (cm^2)	Maximum Field Strength (G)	Average Field Strength (G)
North Polar Region			
1	2.1×10^{17}	1166	460
2	4.0×10^{17}	2217	444
3	3.6×10^{17}	1657	504
4	2.7×10^{17}	1678	638
5	2.6×10^{17}	1461	507
6	1.6×10^{17}	2052	529
7	1.6×10^{17}	1363	430
8	1.3×10^{17}	1942	524
9	1.5×10^{17}	1370	713
10	2.1×10^{17}	1764	414
Average	2.3×10^{17}	1648	516
East limb			
1	11.3×10^{16}	1290	549
2	7.2×10^{16}	982	452
3	5.1×10^{16}	1063	481
4	4.6×10^{16}	1167	477
5	7.5×10^{16}	1336	373
6	7.2×10^{16}	1242	522
7	5.7×10^{16}	805	351
8	6.1×10^{16}	1139	401
9	4.2×10^{16}	1049	355
10	9.7×10^{16}	1917	440
Average	6.9×10^{16}	1179	440

3.2 Histgram of Magnetic Field Strength

We observed the quiet Sun located at the extreme East limb to provide a reference data set for the polar region. Figure 3.3 shows the areal fraction (histogram) of the intrinsic magnetic field strength. The histograms are normalized to the total number of pixels in each SOT/SP map including those pixels for which Milne−Eddington inversion is not carried out, so that we can directly compare the two distributions. There is a large difference in the distribution of the magnetic fields classified as *vertical*: the distribution for the quiet Sun at the East limb is symmetric around zero, clearly showing balanced polarity in the magnetic flux, while the distribution for the North polar region is highly asymmetric, showing a predominance of a single polarity. The distributions for the positive polarity are similar between the quiet Sun and the polar region, while in the negative polarity regime, the amount of the flux is higher in the polar region than in the quiet Sun. For instance, fractional number of pixels with intrinsic field strength of -1 kG in the polar region is about five times larger than that in the quiet Sun.

We also point out that the distributions of the magnetic fields classified as *horizontal* (Ishikawa and Tsuneta 2009, and references therein) in both the regions are strikingly similar in spite of the considerable difference in the amount of the *vertical* magnetic fields between the quiet Sun and the polar region.

Figure 3.4 shows fraction of the negative *vertical* magnetic fields with the intrinsic field strength stronger than the value in the horizontal axis. The fraction at 0 G indicates that the area covered by the negative polarity is 63.7 % (polar region) and 53.1 % (quiet Sun). The polar region is more dominated by negative-polarity magnetic field with increasing field strength, while in the quiet Sun, magnetic fields of both polarities are equally distributed independent of field strength. In the polar region, the fraction of the negative magnetic flux reaches about 90 % at 1 kG. Clearly, bipolar fields are dominant in the quiet Sun, while the unipolar fields are predominant above 500 G in the polar region.

The total magnetic flux for the magnetic field vectors classified as *vertical* in the entire FOV is defined to be $\sum B_j \cos i_j f_j s_j$, where B_j, i_j, and f_j are the intrinsic magnetic field strength, the inclination angle obtained with Equations 2.17 and 2.18, and the filling factor of the j-th SOT pixel inside the SOT/SP FOV, respectively,

and s_j is the pixel size. The true size of the FOV is 8.4×10^{20} cm^2 (polar region) and 3.5×10^{20} cm^2 (East limb). The total magnetic flux in the SOT/SP FOV is 1.7×10^{21} Mx for the polar region and 4.0×10^{20} Mx for the quiet Sun. (Note the factor of 2.4 difference in the observed area between the polar region and the quiet Sun.)

The total magnetic flux for the magnetic field vectors classified as *horizontal* is more difficult to estimate. To make a crude estimate, we define it to be $\sum B_j \sin i_j L_j H_j$ (Ishikawa, Tsuneta, & Jurčák 2010), where B_j and i_j are the intrinsic magnetic field strength and the inclination angle obtained with Equations 2.17 and 2.18, respectively (e.g., Figure 9 of Ishikawa, Tsuneta, & Jurčák 2010). L_j is the linear size of the pixel size and is commonly $0''.16$. H_j is the diameter of the horizontal flux tubes and is commonly assumed to be 190 km, following Ishikawa, Tsuneta, and Jurčák (2010). Here, the filling factor f_j is replaced with the representative diameter H_j of the horizontal flux tubes. The diameter is smaller than the thickness of the line forming layer, contributing to the apparent filling factor $f_j < 1$ for horizontal magnetic fields. The total magnetic flux thus estimated is 9.9×10^{21} Mx for the polar region, and 4.0×10^{21} Mx for the quiet Sun. The ratio in magnetic flux (*horizontal/vertical*) is 10 (quiet Sun) and 5.8 (polar coronal hole), and the magnetic flux classified as horizontal is larger than that of the magnetic flux classified as vertical by a factor 5.8–10 (e.g., Lites et al. 2008)

The present result also shows that the estimation of the radial magnetic flux in the polar regions, if measured only with longitudinal magnetographs, may be contaminated by the massive presence of the horizontal magnetic fields.

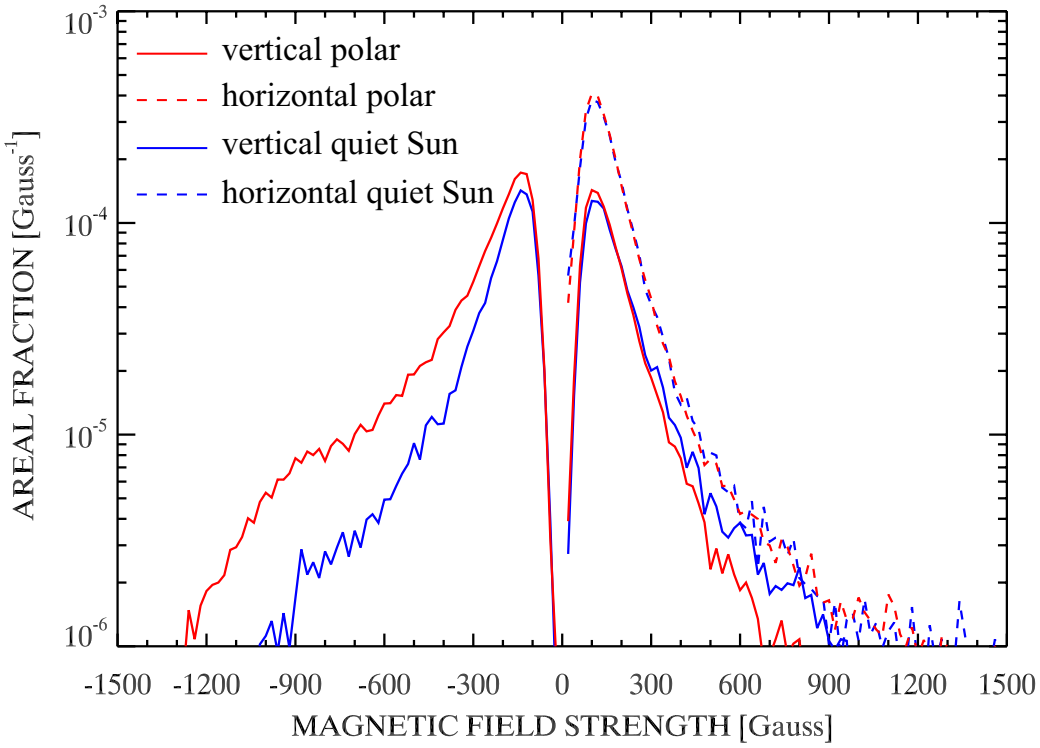

Figure 3.3: Areal fraction of the intrinsic magnetic field strength. The red and blue lines represent the North polar region and the quiet Sun at the East limb, respectively. The solid and dashed lines represent the magnetic fields classified as *vertical* and *horizontal* in this work (see section 2.4.1 for details), respectively. Vertical magnetic field has a sign that indicates either plus or minus polarities, while horizontal magnetic field does not have sign. Vertical axis is the number of pixels divided by total number of pixels (including the pixels for which inversion is not performed) in the respective FOV.

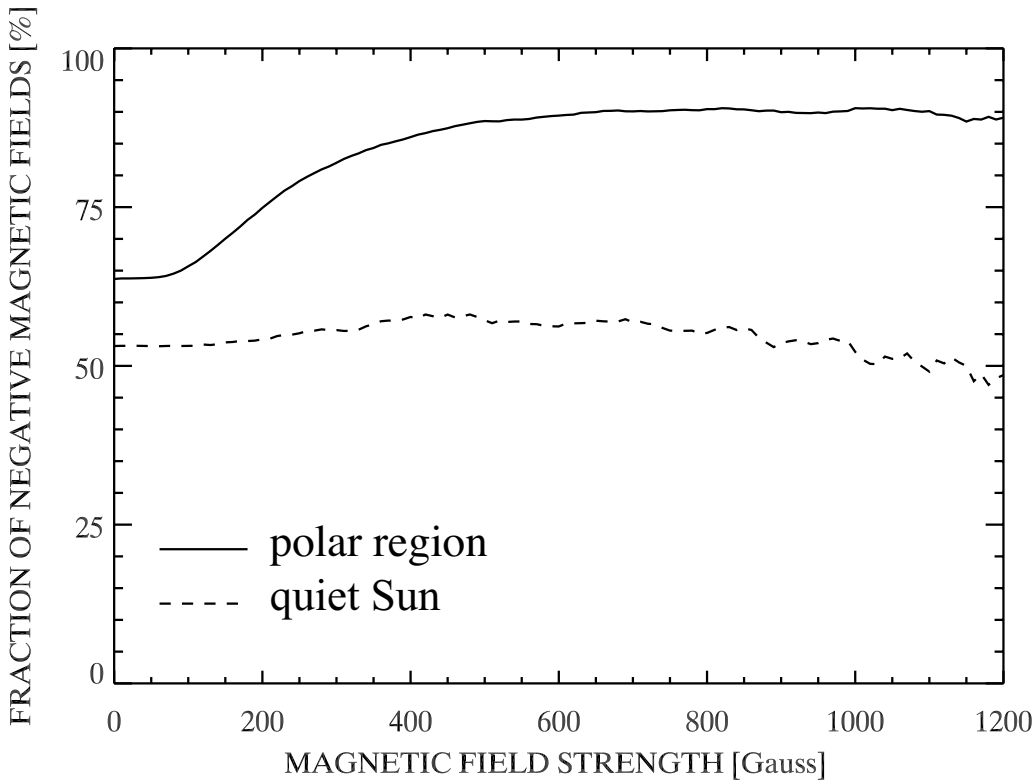

Figure 3.4: Fractional number of pixels that have negative vertical magnetic field with the intrinsic strength stronger than the value in the horizontal axis; North polar region (bold line) and the quiet Sun at East limb (broken line).

3.3 Coronal Magnetic Field Structure

A three-dimensional coronal magnetic field is reconstructed using a high-resolution potential field source surface (PFSS) model recently developed by D. Shiota (2009, private communication). The *Hinode* vertical magnetic field data are embedded in the high-resolution *MDI* synoptic maps[*1] of the Carrington rotation 2061 (for the polar region) and 2063.35 (for the quiet Sun at the East limb). The size of the *MDI* maps is (3600, 1080) pixel. The synoptic map at the Carrington rotation 2063.35 is the combined map of the Carrington rotations 2063 and 2064 such that the embedded *Hinode* region is located in the center of the synoptic map. We assume that the filling factor of the *Hinode* data is equal to 1, and that the magnetic field vectors classified to vertical are vertical relative to the local photospheric normal. The synoptic maps are expanded with spherical harmonics of extremely high degree ($L_{\max} = 2048$) whose equatorial resolution is ~ 1072 km.

Figure 3.5 shows the snapshots of the inferred three-dimensional coronal magnetic fields reconstructed with the PFSS model where the source surface is assumed to be located at 2.5 $R_\odot$. We can clearly see that the majority of magnetic field lines from the kG-patches in the polar coronal hole are open with canopy structures just above the photosphere. There are some closed magnetic field lines in the polar coronal hole as well. On the contrary, in the quiet Sun, almost all the field lines are closed. (We confirm that some field lines going outside the box are connected to other parts of the Sun.) The bipolar nature of the quiet Sun, and the unipolar nature of the polar coronal hole is one of the significant differences between the two regions.

Alfvén waves are believed to be responsible for the acceleration of the fast solar wind (Suzuki and Inutsuka 2006). Whether the Alfvén waves generated in the photosphere are reflected back (Fujimura and Tsuneta 2009) at the photosphere/corona boundary may depend on the degree of the expansion of the flux tubes as a function of height. Open field lines from the kG-patches in the polar region may expand at very low altitude, so that there will be less discontinuity in the Alfvén velocities. Magnetic flux tubes with fanning-out structures in the very low atmosphere may serve as a chimney for the Alfvén waves to propagate to the corona (Tsuneta et al.

[*1] http://soi.stanford.edu/magnetic/index6.html

2008a).

Figure 3.6 shows the average magnetic field strength as a function of height in the North polar region and the quiet Sun at the East limb. $|Br|$ and $|Bl|$ represent the averaged radial and lateral components of the coronal magnetic field obtained by the high resolution PFSS model, respectively, where $|B| = \sqrt{Br^2 + Bl^2}$. The radial magnetic field strength decreases with altitude significantly slower in the polar region than in the quiet Sun, and magnetic field strength above the polar region is much higher than that in the quiet Sun.

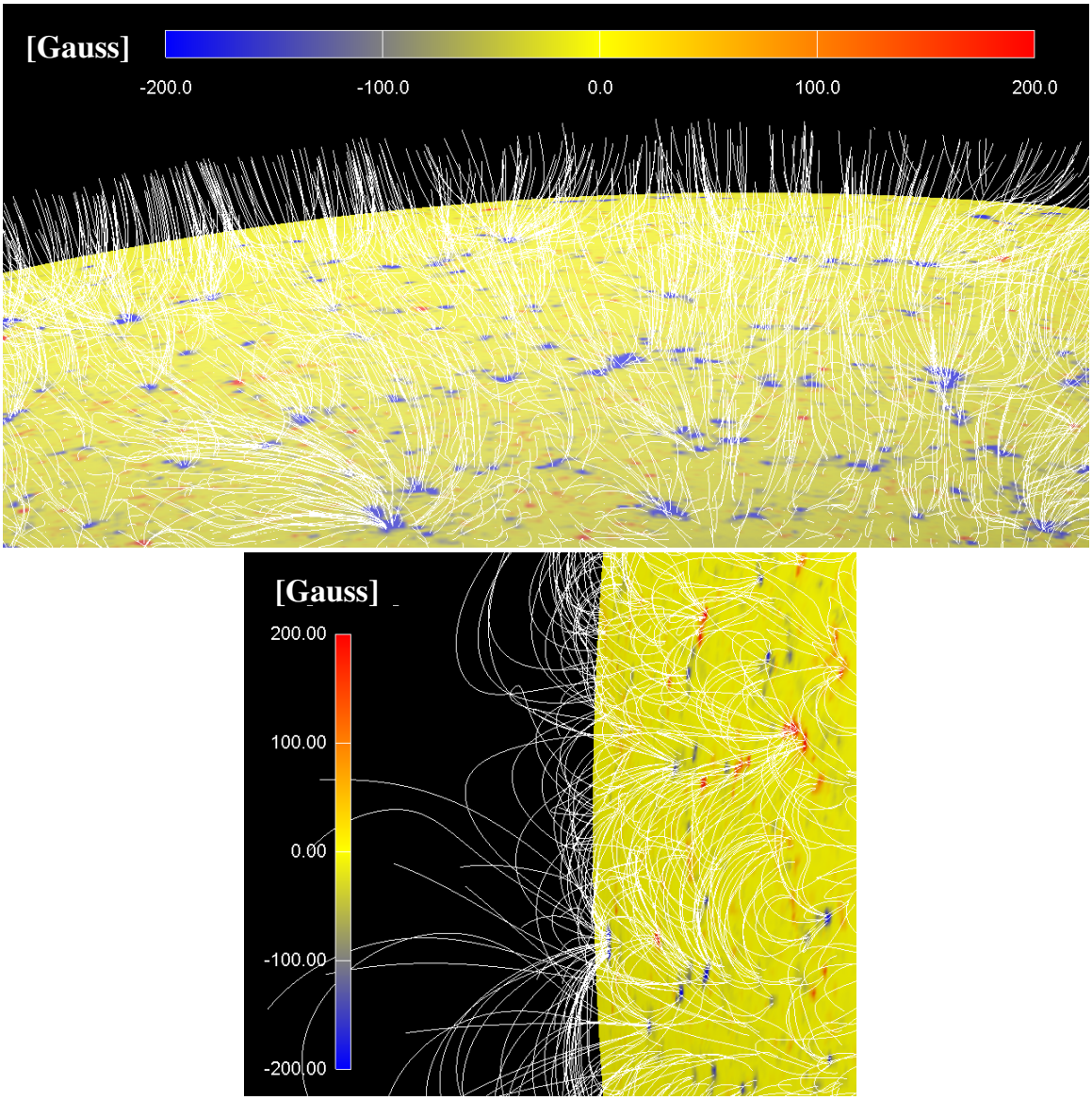

Figure 3.5: Coronal magnetic field structure with the data shown in Figures. 2.5 and 2.10 for the quiet Sun at the East limb (lower panel) and the North polar coronal hole (upper panel), respectively. The color of the magnetic patches indicates intrinsic field strength of the magnetic field vectors classified as vertical. The red patches are positive magnetic concentrations, and the blue ones are negative.

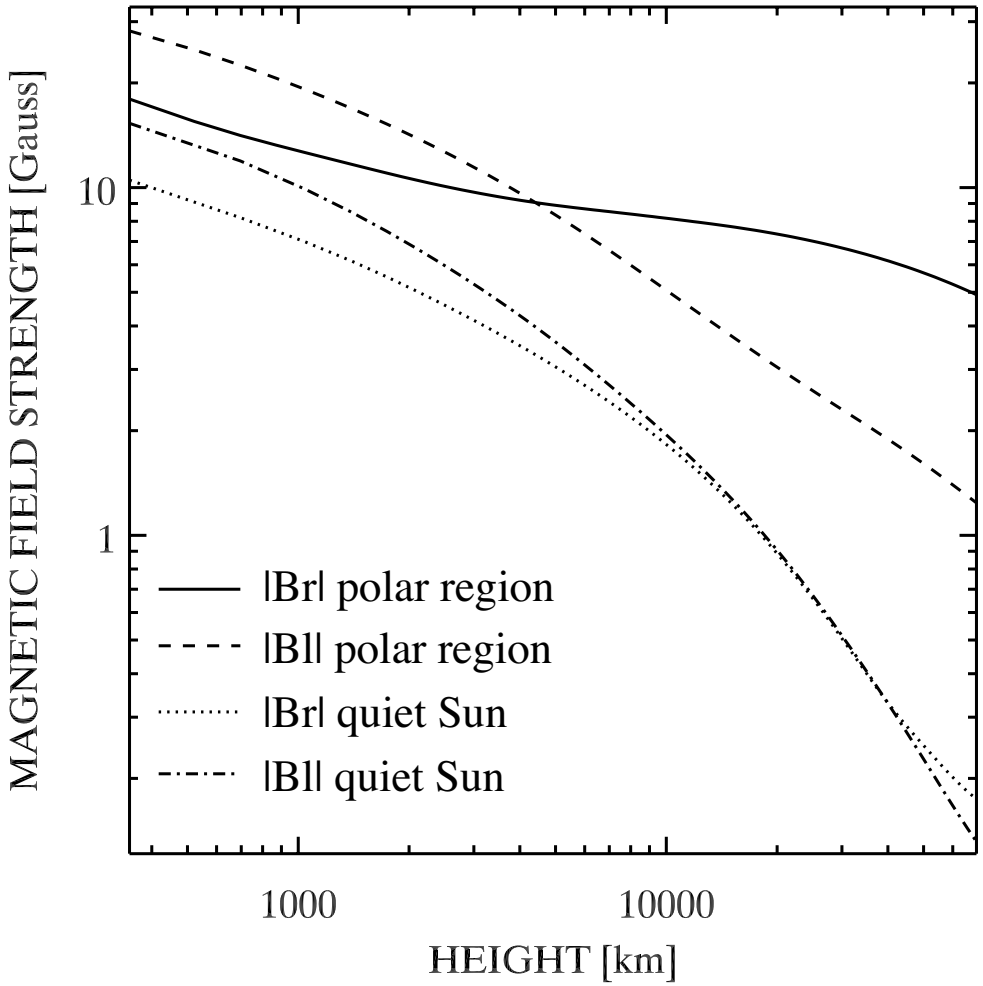

Figure 3.6: Average magnetic field strength as a function of height for the North polar region and the quiet Sun at the East limb. The dashed and dash-dotted lines represent the lateral component $|Bl|$ of the average magnetic field, and the solid and dotted lines indicate the radial component $|Br|$ at each height.

3.4 Discusion and Conclusion

In this paper, we have made a detailed comparison of the photospheric magnetic properties between the polar region and the quiet region. We found that the magnetic properties of the polar region are significantly different from those of the quiet Sun. Positive and negative magnetic fields are well balanced in the quiet Sun, while in the North polar region, negative-polarity magnetic fields dominate the other polarity. The excess negative magnetic field makes both total unsigned magnetic flux and net (signed) magnetic flux larger than those of the quiet Sun.

3.4.1 Kilo-Gauss Magnetic Patches

All the large magnetic concentrations in the polar region essentially have the same magnetic polarity, while the smaller patches have the same and the opposite magnetic polarities. Shimojo and Tsuneta (2009) reported bipolar emergence of magnetic fields in the polar region, and this may contribute to the conspicuous minority polarity patches. The average area and the average magnetic flux of the kG-patches appear to be considerably different between the two regions: the sample data set tabulated in Table 3.1 shows that kilo-Gauss magnetic concentrations in the polar region have a factor of 3.3 larger average area and have a factor of 4.8 larger total magnetic flux than those in the quiet Sun. The number of the kG-patches in the polar region appears to be larger than that of the quiet Sun.

The origin and/or evolution of the kG-patches would be different between the polar region and the quiet Sun. The different properties of the kG-patches in the polar regions and the quiet Sun could be due to the different environment in which they evolve. There may be a higher chance in the quiet Sun that the positive and negative patches collide, reconnect, and lose magnetic energy or submerge as a result. As such, the environment in the quiet Sun may not allow the elemental magnetic concentrations to grow.

3.4.2 Horizontal Magnetic Fields

From Figure 3.3, 98% of the horizontal magnetic fields have the intrinsic field strengths smaller than 700 G both in the quiet Sun at the limb and the polar region. Here the horizontal magnetic fields refer to the magnetic field vectors classified as horizontal. Ishikawa and Tsuneta (2009) reported that 93% of horizontal magnetic fields have intrinsic field strengths smaller than 700 G and 98% smaller than 1 kG in the quiet Sun and a plage region both located near the center of the solar disk. Magnetic field strength of 700 G corresponds to the typical equipartition field strength at the level of granules, where the density is 10^{-6} g cm^{-3} at the depth of 500 km and the velocity is 2 km s^{-2}. If we take the mean density 2.7×10^{-7} g cm^{-3} at the base of the photosphere, the equipartition field strength is 350 G. Even in this case, 92% of the horizontal magnetic fields have the intrinsic field strengths smaller than 350 G both in the quiet Sun at the limb and the polar region. Although

the vertical magnetic flux in the polar region is larger than that of the quiet Sun, the horizontal magnetic flux in the polar region is remarkably similar to that of the quiet region. The small difference between the two results (98% in the present paper and 93% in Ishikawa and Tsuneta (2009) at 700 G) could be due to the following two factors: (1) A higher atmosphere is observed in the limb observations, so that the measured magnetic field strength may be smaller in the limb observations. (2) The horizontal magnetic fields are observed through Stokes Q and U in the disk center observations, while Stokes V is involved in the limb observations. Thus, the limb observations may have higher sensitivity to the horizontal magnetic fields.

Ishikawa and Tsuneta (2009) proposed that a local dynamo process be uniformly operating in the photosphere or below based on the observations that the probability distribution function of the transient horizontal magnetic fields in the quiet Sun is the same as that in a plage region. If we assume that the magnetic properties of the quiet Sun in the disk center analyzed by Ishikawa and Tsuneta (2009) are the same as those of the quiet Sun at the East limb analyzed in this paper, we would conclude that the distribution function of the horizontal magnetic fields and the amount of the magnetic flux are exactly the same in the quiet Sun, a plage region and in the polar region. This provides a firmer evidence that a local dynamo process driven by the granular motion is responsible for the generation of the horizontal magnetic fields.

3.4.3 Polar Coronal Holes

Kano et al.(2008b) obtained the temperatures and the densities of the polar coronal hole and the quiet Sun with the XRT (Golub et al. 2007; Kano et al. 2008a) aboard *Hinode*. These are the most accurate measurements carried out using the broadband filters by correcting for the effect of scattered X-rays with the lunar occultation. The temperatures and electron densities then derived are 1.0 MK and $1.0-1.5 \times 10^8 \mathrm{cm}^{-3}$ for the polar coronal hole, and 1.5−2.0 MK and $2.0-3.0 \times 10^8 \mathrm{cm}^{-3}$ for the quiet Sun. The plasma pressures are $1.4-2.1 \times 10^{-2} \mathrm{dyne} \cdot \mathrm{cm}^{-2}$ and $4.1-8.3 \times 10^{-2} \mathrm{dyne} \cdot \mathrm{cm}^{-2}$ for the coronal hole and the quiet Sun, respectively. Thus, plasma pressure in the coronal hole is a factor of 3−6 smaller than that of the quiet Sun.

The coronal hole in the upper corona inside the Alfvénic sphere should have collapsed due to the lateral pressure from the surrounding quiet Sun corona, if the

magnetic field strength in the polar coronal hole is much smaller than that of the quiet corona. The polar coronal hole is stable for a long time, and the coronal hole and the surrounding corona of the quiet Sun must be in pressure equilibrium. In this paper, we showed that the magnetic flux of the polar region in the photosphere is larger than that in the quiet Sun (Figure 3.3). Indeed, magnetic pressure estimated from Figure 3.6 is 1 dyn cm^{-2} in the polar region and 3×10^{-3} dyn cm^{-2} above the quiet Sun at the height of 7×10^4 km. The boundary of the polar coronal hole and the quiet Sun must be determined by the total pressure balance between the coronal hole and the corona in the quiet Sun, and the polar corona expands to the lower latitude until it reaches the magnetic plus plasma pressure equilibrium with the quiet-Sun corona. This may be the reason why the fast solar wind from the polar region reaches the lower latitude (McComas et al. 2000).

3.4.4 Polar Coronal Activities

DeForest et al. (1997) investigated the correlation between solar plumes and polar magnetic field with *SOHO* and found that there is opposite magnetic flux close to the foot point of solar plumes. In the polar coronal hole, X-ray jets are observed with high occurrence rate (60 polar X-ray jets per day on average; Kamio et al. 2007; Cirtain et al. 2007; Savcheva et al. 2007). Shimojo and Tsuneta (2009) revealed that the opposite magnetic fields close to the kG-patches are related to the occurrence of the X-ray jets. Distribution of such opposite magnetic fields around a kG-patch is indeed seen in the (signed) magnetic field map in the North polar region (Figure 2.5) and may be responsible for various coronal activities.

Chapter 4

Four-year-variation of Magnetic Fields in the Polar Regions

4.1 Introduction

In this chapter, we have analyzed long term variation of the magnetic field in the North and South polar regions. The evolution of the magnetic fields in the polar regions is closely related to the global solar cycle as described in section 1.3. The coronal hole in each pole is usually formed in the declining phase of the solar cycle, and disappears before the solar maximum. Harvey and Recely (2002) described in detail on the reversal of the polar magnetic fields (see also Timothy et al. 1975). At around the solar maximum, the magnetic fields in the polar regions are complex, and a number of smaller mid-latitude holes eventually from the polar coronal holes (Webb et al. 1984). The polar coronal hole grows during the declining phase and its area becomes maximum at the solar minimum. During the rising phase, the polar coronal hole area begins to decrease and then disappears just before the solar maximum. Therefore the polar coronal holes have represented an important proxy to the polarity reversal.

In the meantime, the polar regions had been observed with ground-based magnetograms (Babcock and Babcock 1955; Severny 1971; Svalgaard et al. 1978; Tang and Wang 1991; Lin et al. 1994; Homann et al. 1997; Fox et al. 1998; Okunev and Kneer 2004; Blanco Rodriguez et al. 2007). These observations as well as the recent observations with SOHO/MDI (Benevolenskaya 2004) have provided the measurements of the line-of-sight (LOS) magnetic component. As shown in previous chapters, the high-resolution observation of the vector magnetic fields with SOT

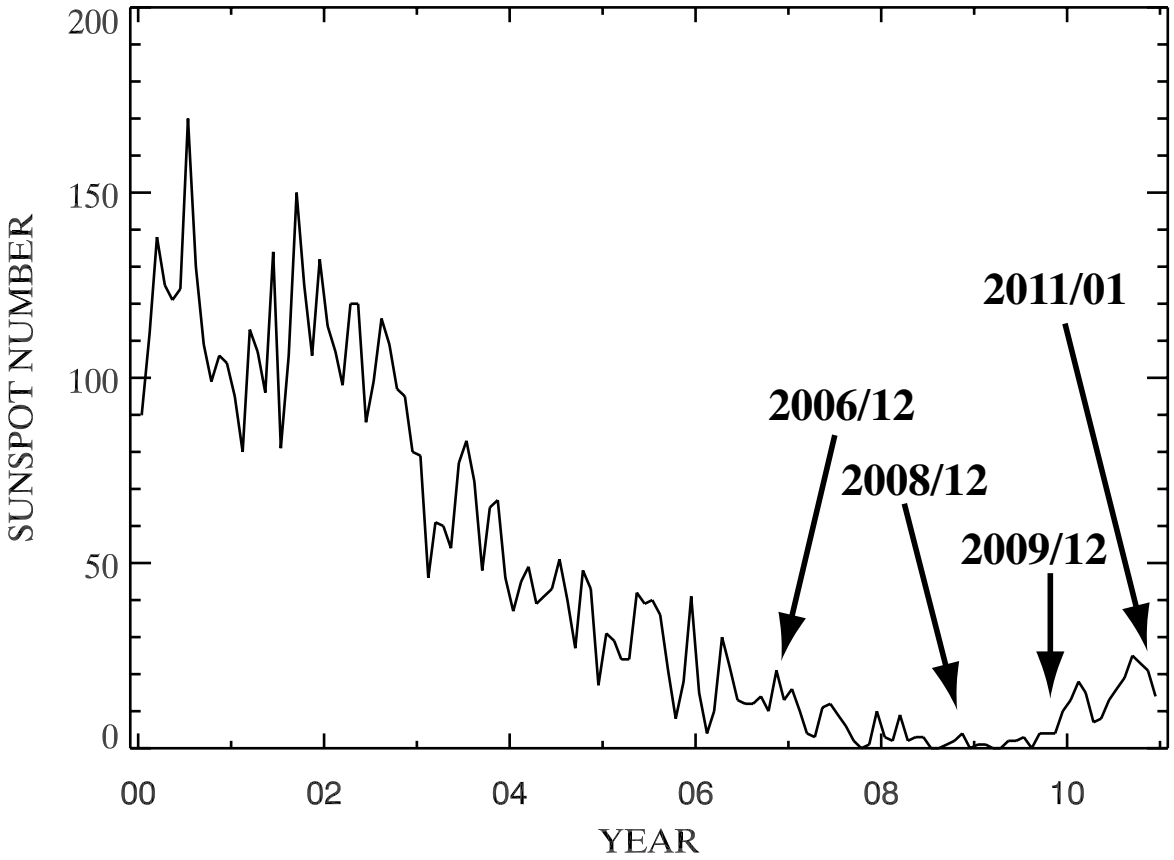

Figure 4.1: The number of sunspot between 2000 and 2011. (Coursty of National Geophysical Data Center; ftp://ftp.ngdc.noaa.gov/STP/SOLAR_DATA/SUNSPOT_NUMBERS/INTERNATIONAL/monthly/MONTHLY.PLT) The observations used in this study are shown by arrows. *Hinode* was launched on September, 2006.

aboard *Hinode* revealed a totally new view of the magnetic fields of the polar regions (Tsuneta et al. 2008; Ito et al. 2010). However, their long term variation their has not been investigated with *Hinode*/SOT. Figure 4.1 shows the monthly variation of the sunspot number. The previous cycle (Cycle 23) ended, and the new cycle (Cycle 24) started on December 2008 when the sunspot number began to increase. At present, the sunspot number continues to increase, and is apparently in the rising phase of the solar cycle. In this chapter, we present the long term variation of the magnetic field and their latitudinal distribution in both polar regions over four years.

4.2 Observations

We use 8 SOT/SP data sets. The North polar region was observed at 2006 December 20, 2008 December 19, 2009 December 25 and 2011 January 6 (hereafter labeled as N06, N08, N09, and N11, respectively). Magnetic fields in the South polar region are observed at 2006 December 21, 2008 December 20, 2009 December 26 and 2011 January 7, which are labeled as S06, S08, S09, and S11, respectively. There are more data sets for the polar regions. We mainly choose the data taken in December as far as possible, since the B-angle*[1] for December is about -2, about -2 degree, and we are able to equally see both the North and South polar regions (see also Table 4.1).

The SP records the Stokes spectral profiles (*I, Q, U* and *V*) of FeI 630.15 nm and 630.25 nm with a wavelength sampling of 2.15 pm pixel^{-1} and with a scan step of $0''.16$ and exposure time of 4.8 s. Note that some observational parameters of each data set were not the same. For example, there are differences in the location of the observed field of view (FOV) on the solar disk and the observation mode. We tabulate the detailed information of the 8 data sets in Table 4.1. The observation mode in 2006 (N06 and S06) are different. The data in 2006 are obtained using the double-side CCD mode, where photons with orthogonal polarization are acquired by the CCD, so that we do not lose any photons. Another difference is that these two observations in 2006 have higher spatial resolution with $0''.16$ pixel size, while other observations have of $0''.32$ pixel size.

A least-squares fitting was applied to the Stokes spectra with the MILOS code (Orozco Suárez and del Toro Iniesta 2007). We calculate the magnetic field strength and the inclination and azimuth angle with respect to the LOS with the Milne-Eddington least-squares fitting described in Chapter 2. RMS photon noise σ/I_c depends on the exposure time, where I_c is the continuum intensity, and slightly varies in each observation. The parameter σ/I_c is also tabulated in Table 4.1.

Hereafter, we describe the polar landscape from 2006 through 2011 and comparethem.

*[1]The hliographic latitude of the centre of the solar disk; also called the B-angle. The range of the B-angle is ± 7.23 degrees, correcting for the tilt of the ecliptic with respect to the solar equatorial plane. If B-angle is minus, the North rotational pole is not visible.

Table 4.1: Hinode SOT/SP polar observations used in this chapter.

North polar region				
Date	2006/12/20 (N06)	2008/12/19 (N08)	2009/12/25 (N09)	2011/01/06 (N11)
B-angle	-1.51°	-1.45°	-2.16°	-3.55°
Field of View	$327''.52 \times 163''.84$	$323''.2 \times 163''.84$	$314''.24 \times 163''.84$	$326''.72 \times 163''.84$
Observation mode	Normal mode	Fast Deep mode	Fast Deep mode	Fast Deep mode
CCD mode	Double side	Single side	Single side	Single side
Pixel size	0."16	0."32	0."32	0."32
σ/I_c (1)	0.00123	0.00078	0.00079	0.00083
South polar region				
Date	2006/12/21 (S06)	2008/12/20 (S08)	2009/12/26 (S09)	2011/01/07 (S11)
B-angle	-1.64°	-1.58°	-2.29°	-3.66°
Field of View	$327''.52 \times 163''.84$	$325''.76 \times 163''.84$	$320''.64 \times 163''.84$	$292''.48 \times 163''.84$
Observation mode	Normal mode	Fast Deep mode	Fast Deep mode	Fast Deep mode
CCD mode	Double side	Single side	Single side	Single side
Pixel size	0."16	0."32	0."32	0."32
σ/I_c (1)	0.00126	0.00084	0.00087	0.00086

Note: (1) see text.

2006 December (declining phase of Cycle 23)

Figure 4.2 (N06) and Figure 4.3 (S06) are the maps of the signed vertical magnetic fields which are converted as seen from just above each pole. The negative polarity of magnetic fields is dominant in the North polar regions, while the positive polarity is dominant in the South polar region. It is clearly seen that there are plenty of large patchy magnetic field concentrations (kG patches; Tsuneta et al. 2008) of the dominant polarities. As we are closer to limb, the limb formation height becomes higher in the photosphere. Since the flux tube expands with height, the detected magnetic flux per pixel would be smaller. If we consider the effect of noise, this may be equivalent to that the sensitivity to detect magnetic flux concentrations is compromised with latitude. Figure 4.4 shows the areal fraction of the siged intrinsic magnetic field strength, and Figure 4.5 is the areal fraction of the vertical magnetic flux. The dominance of one polarity in the vertical magnetic fields is also clearly seen in the strong field regime in the histogram ($\sim$ 300G). Figure 4.6 shows the areal fraction of the horizontal magnetic flux. Figure 4.4 shows that of the horizontal intrinsic magnetic field strength. These appears to be little difference between the North and the South. This is quite contrasting to the distribution of the vertical magnetic flux.

We calculated the averaged fraction of the magetic flux with the dominant polarity in every 5 degree of latitude within the FOV (Figure 4.7). In the low latitude region (60 $\sim$ 65 degree), the fraction is 70 % to 80 %, and the fraction increases smoothly up to $\sim$ 90% in the high latitude region (80 $\sim$ 85 degree). The difference in the fraction between North and South are slightly seen although the fluctuation way exist.

Because the N06 and S06 observations were carried out with normal mode, and the resultant numbers of photons was about a half of those in other data. Hence, σ/I_c (photon noise) in N06 and S06 data were approximately the $\sqrt{2}$ times larger than those in other data sets. The difference may cause difference in polarization sensitivity.

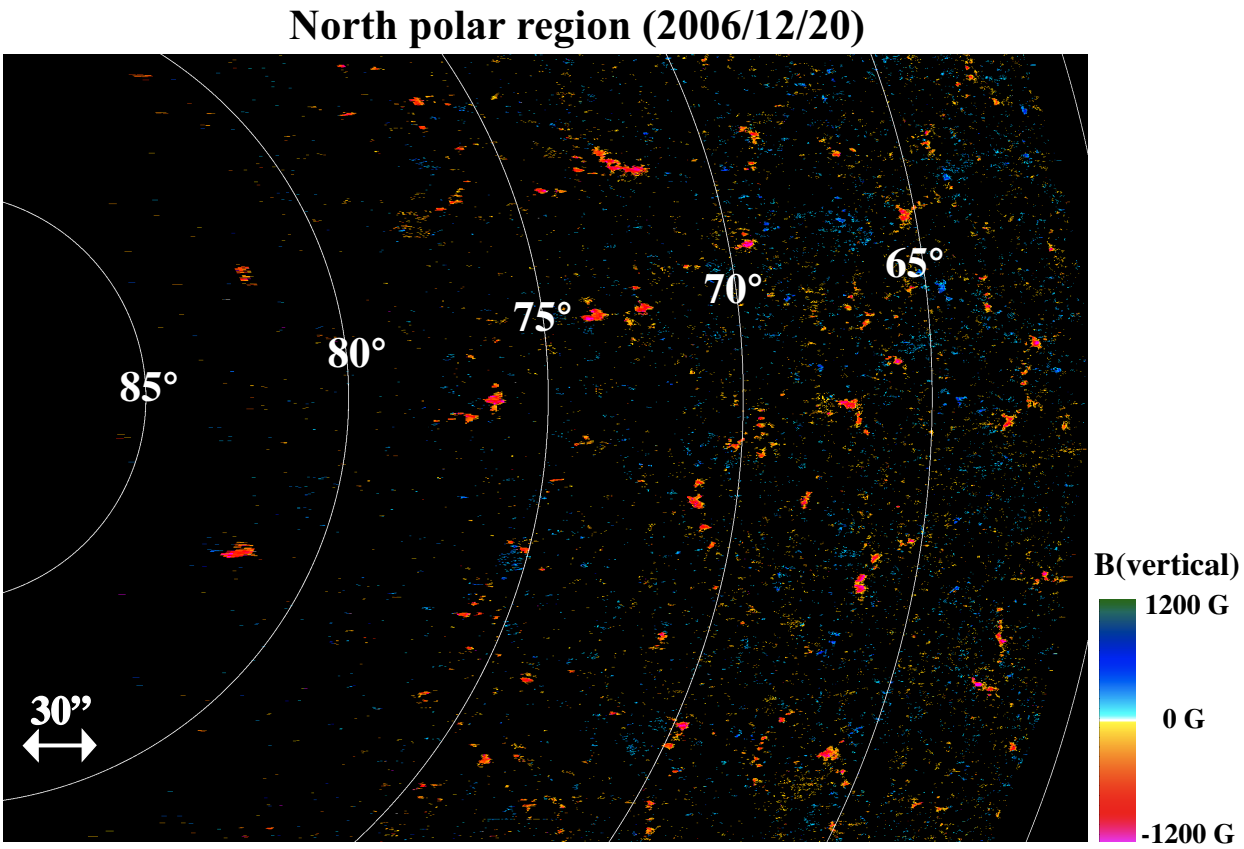

Figure 4.2: The map of signed strength of the magnetic field vectors classified as *vertical* (see section 2.4.1); the map of the magnetic field signed strength on the sky plane is converted to the map seen from above the North pole. The observations took place at 23:42—02:35 UT on 2006 December 20. North is to the left. The pixel size is 0″.16. The magnetic field strengths were obtained only for pixels whose polarization signal exceeds a given threshold (see section 2.3). The size of the FOV for the east-west dierction is 327″.52. The size of the FOV for the North-South direction (163″.84) is expanded to 451″.52 as a result of correction for foreshortening. The circular arc is the latitudinal line per 5° from the North pole.

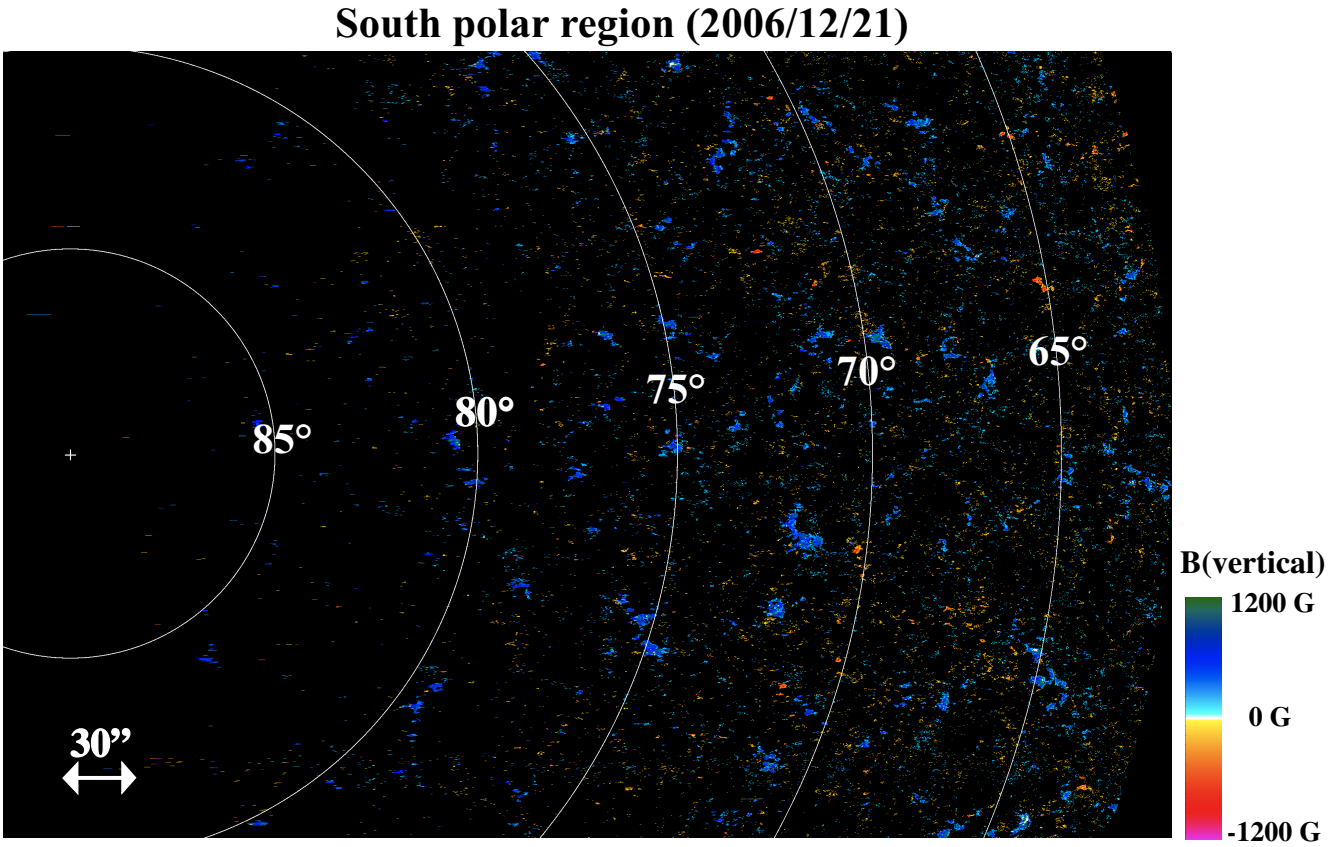

Figure 4.3: The map of signed strength of the magnetic field vectors classified as *vertical* (see section 2.4.1); the map of the magnetic field signed strength on the sky plane is converted to the map seen from above the North pole. The observations took place at 16:50—19:43 UT on 2006 December 21. South is to the left. The pixel size is 0″.16. The magnetic field strengths were obtained only for pixels whose polarization signal exceeds a given threshold (see the section 2.3). The size of the FOV for the east-west dierction is 327″.52. The size of the FOV for the North-South direction (163″.84) is expanded to 486″.4 as a result of correction for foreshortening. The circular arc is the latitudinal line per 5° from the South pole.

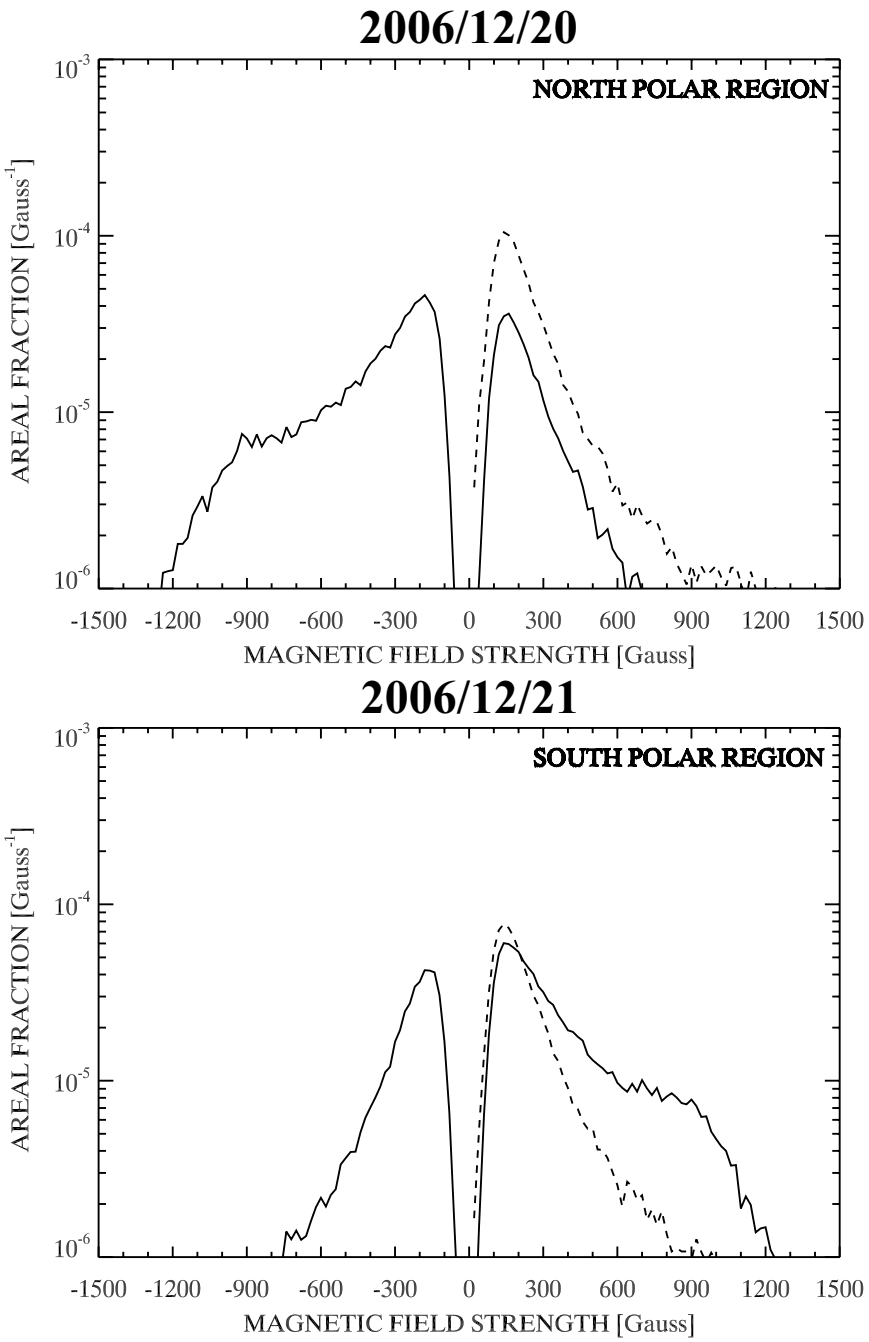

Figure 4.4: Areal fraction of the intrinsic magnetic field strength on 2006 December 20 for the North polar region (upper panel) and on 2006 December 21 for the South polar region (bottom panel). The solid and dashed lines represent the magnetic fields classified as *vertical* and *horizontal* in this work (see section 2.4.1 for details), respectively. Vertical magnetic fields have a sign that indicates either plus or minus polarities, while horizontal magnetic fields do not have sign. Vertical axis is the number of pixels divided by total number of pixels (including the pixels for which inversion is not performed) in the respective FOV.

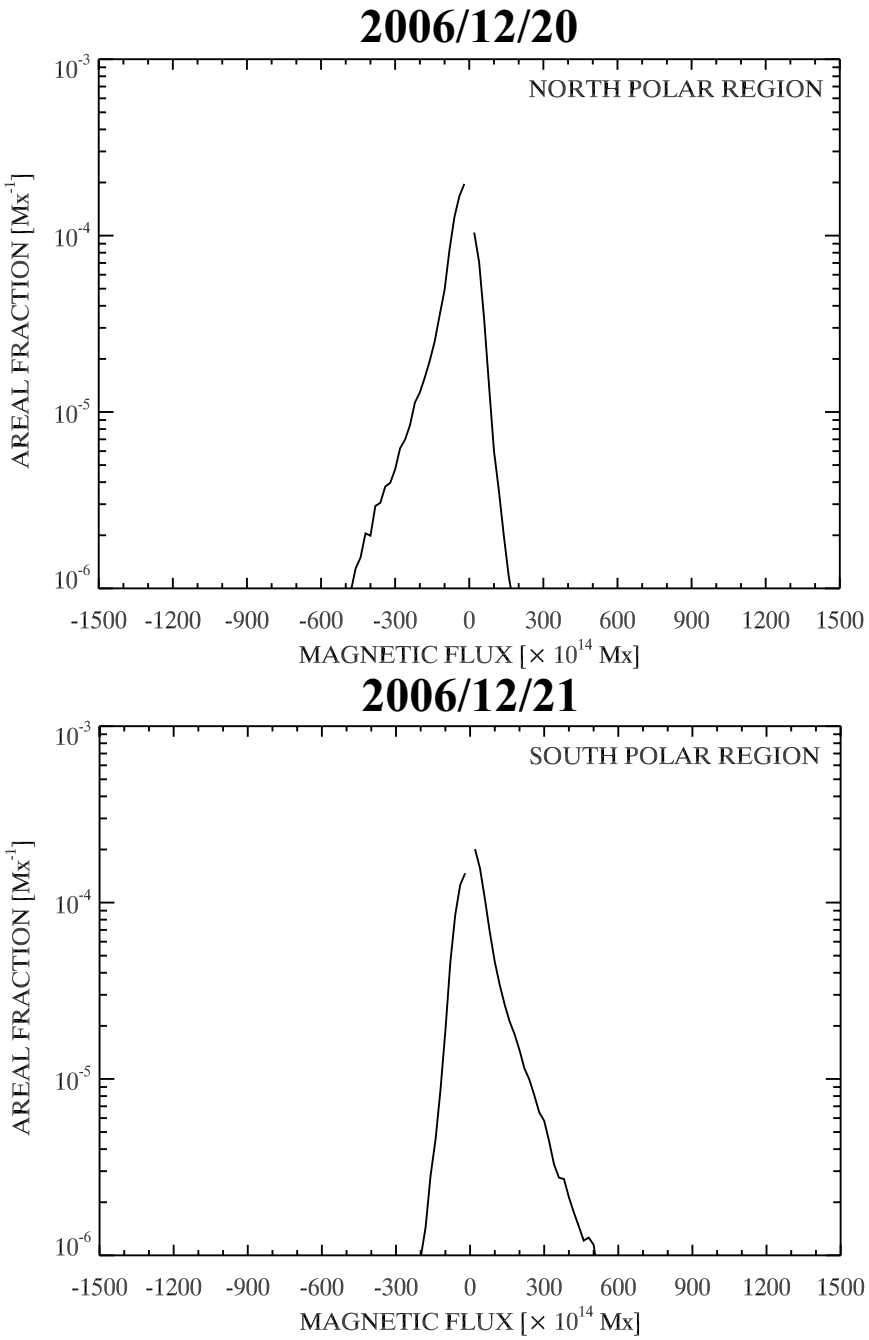

Figure 4.5: Areal fraction of the *vertical* magnetic flux on 2006 December 20 for the North polar region (upper panel) and on 2006 December 21 for the South polar region (bottom panel). The solid line represent the magnetic fields classified as *vertical* in this work (see section 2.4.1 for details). Vertical magnetic flux has a sign that indicates either plus or minus polarities. Vertical axis is the number of pixels divided by total number of pixels (including the pixels for which inversion is not performed) in the respective FOV.

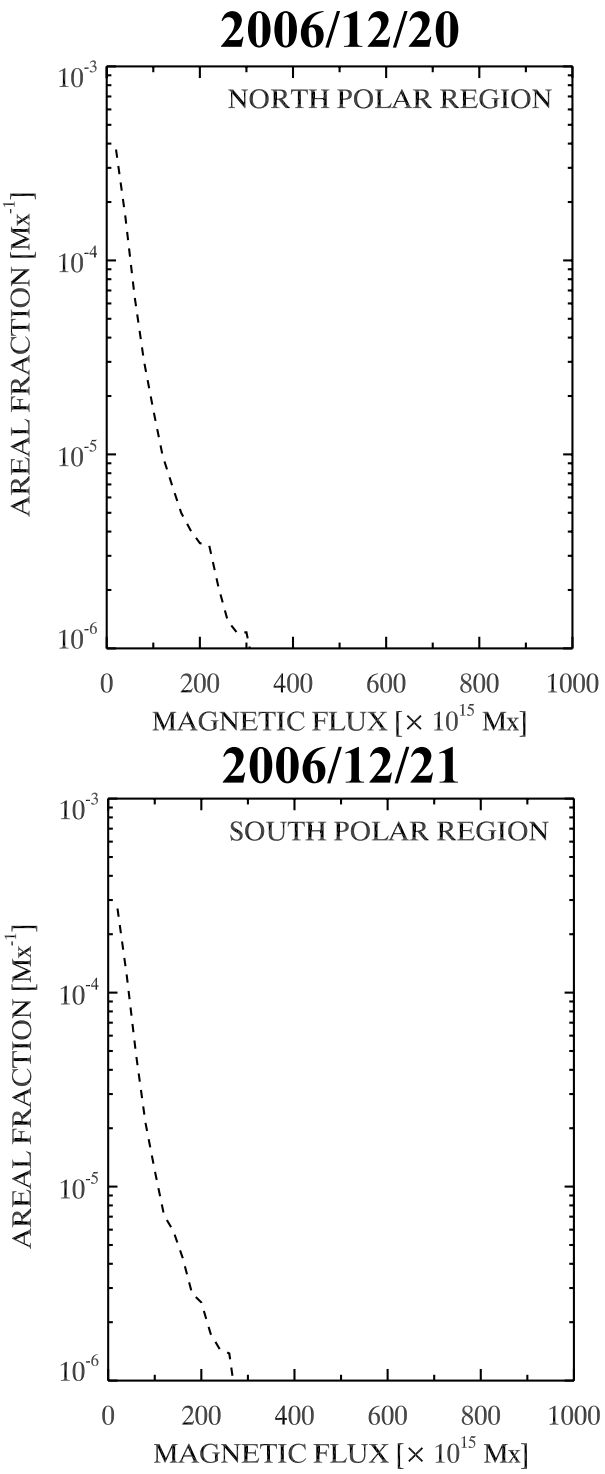

Figure 4.6: Areal fraction of the *horizontal* magnetic flux on 2006 December 20 for the North polar region (upper panel) and on 2006 December 21 for the South polar region (bottom panel). The dashed lines represent the magnetic fields classified as *horizontal* in this work (see section 2.4.1 for details). Horizontal magnetic flux does not have sign. Vertical axis is the number of pixels divided by total number of pixels (including the pixels for which inversion is not performed) in the respective FOV.

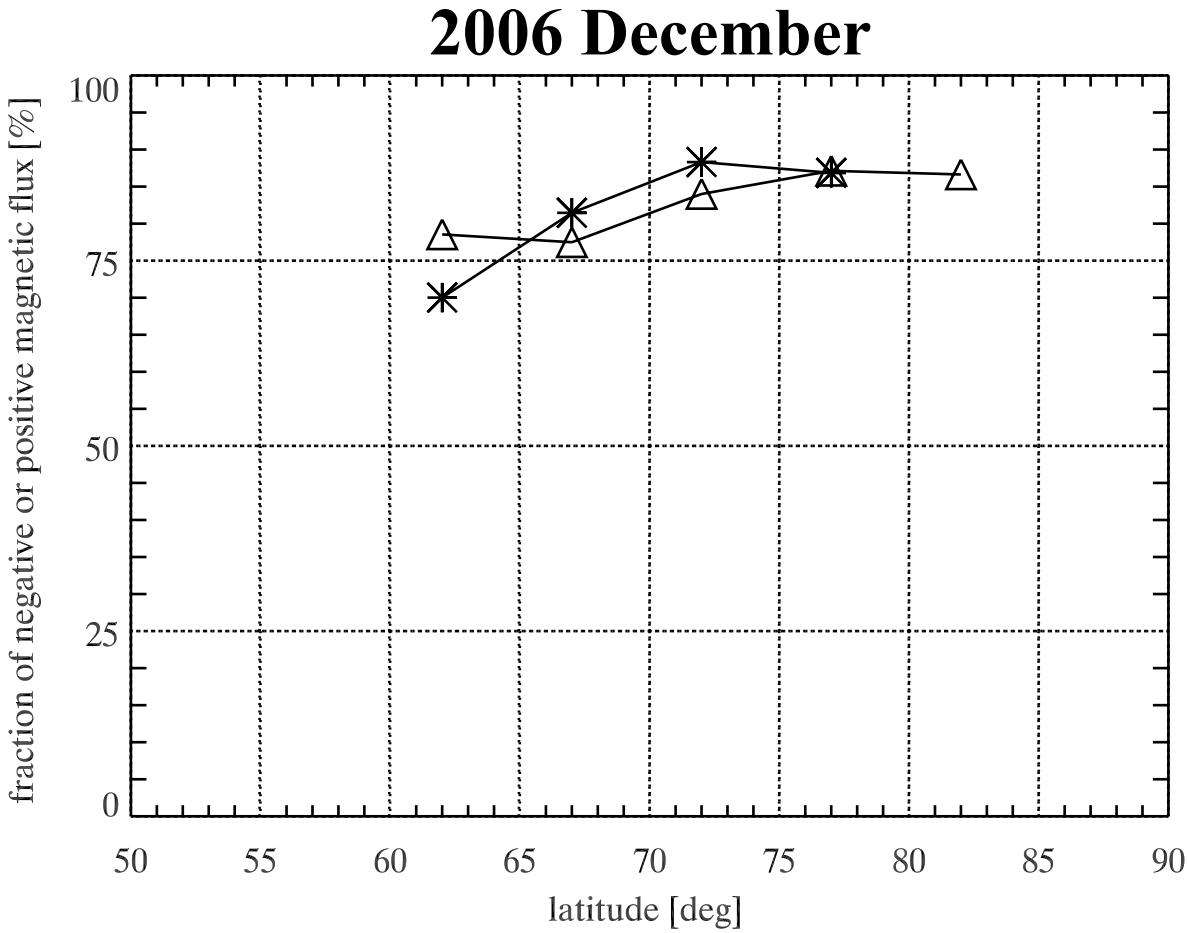

Figure 4.7: Areal fraction of the dominant magnetic flux in both the polar regions in 2006 December. The asterisks and triangles represent the averaged areal (over 5 degree) fraction of the magnetic flux with the dominant polarity in the North and South polar regions, respectively.

2008 December (minimum of solar activity)

The minimum of the solar activity between Cycle 23 and Cycle 24 (Figure 4.1) took place on December, 2008. The global magnetic field is expected to be close to the dipole configuration. We present the maps of the signed vertical magnetic fields in the North polar region N08 (Figure 4.8) and in the South polar region S08 (Figure 4.9), the areal fraction of the intrinsic magnetic field strength (Figure 4.10), the areal fraction of the vertical magnetic flux (Figure 4.11), the areal fraction of the horizontal magnetic flux (Figure 4.12), and the fraction of the dominant magnetic flux in each polar regions (Figure 4.13) with the format same as those of the 2006 data.

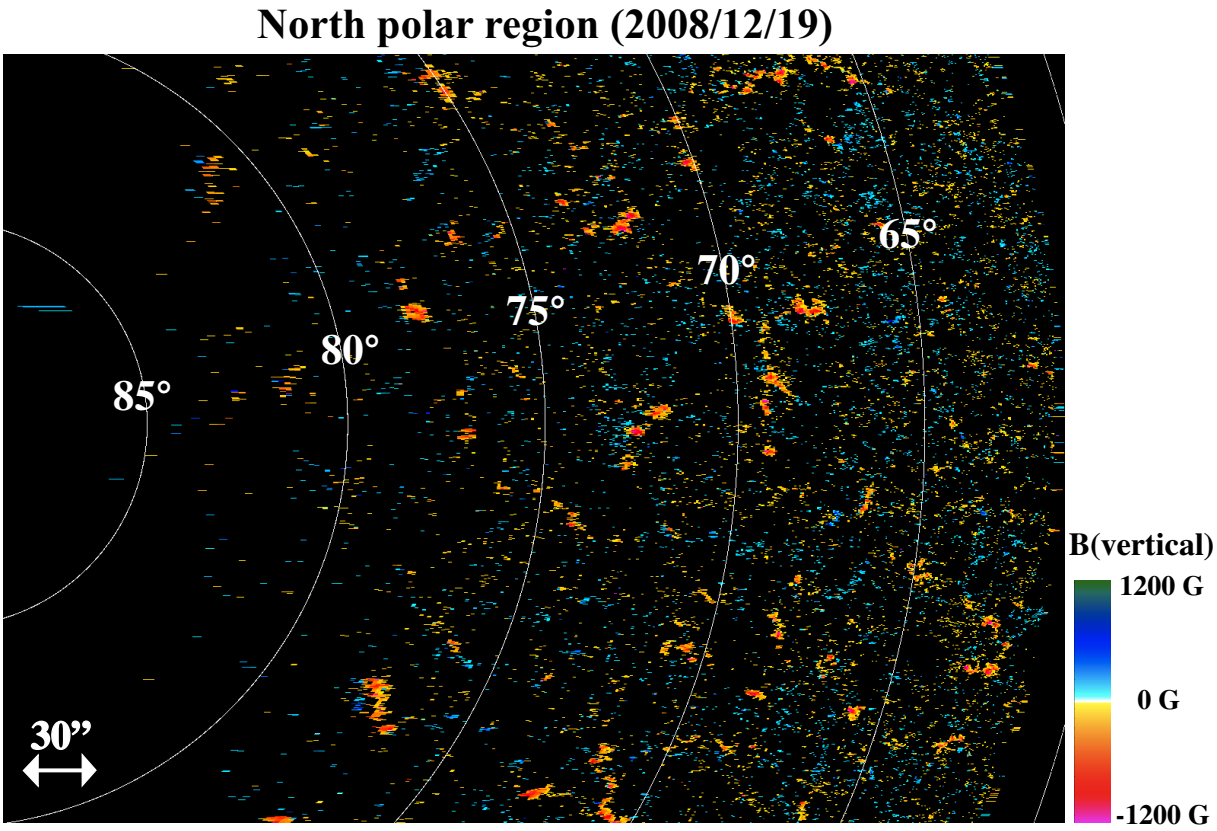

Figure 4.8: Map of signed strength of the magnetic field vectors classified as *vertical* (see section 2.4.1) in the North polar region of the Sun at 10:12—13:05 UT on 2008 December 19. North is to the left. The pixel size is 0″.32. The magnetic field strengths were obtained only for pixels whose polarization signal exceeds a given threshold (see section 2.3). The size of the FOV for the east-west direction is 323″.2. The size of the FOV for the North-South direction (163″.84) is expanded to 446″.72 as a result of correction for foreshortening. For other notations of the image, see the caption of Figure 4.2.

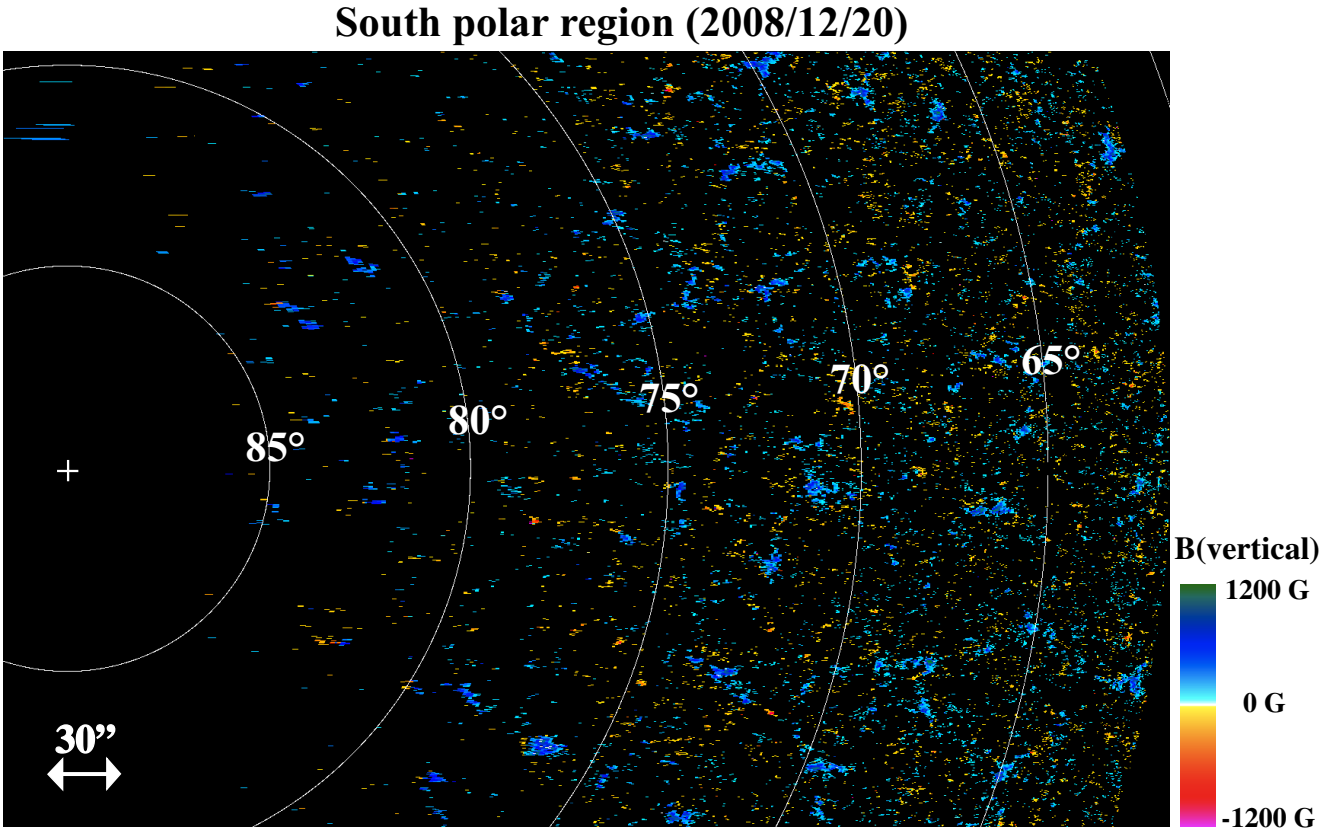

Figure 4.9: Map of signed strength of the magnetic field vectors classified as *vertical* (see section 2.4.1) in the South polar region of the Sun at 10:47—13:40 UT on 2008 December 20. The size of the FOV for the east-west direction is 325″.76. The size of the FOV for the North-South direction (163″.84) is expanded to 490″.56 as a result of correction for foreshortening. For other notations of the image, see the caption of Figure 4.3.

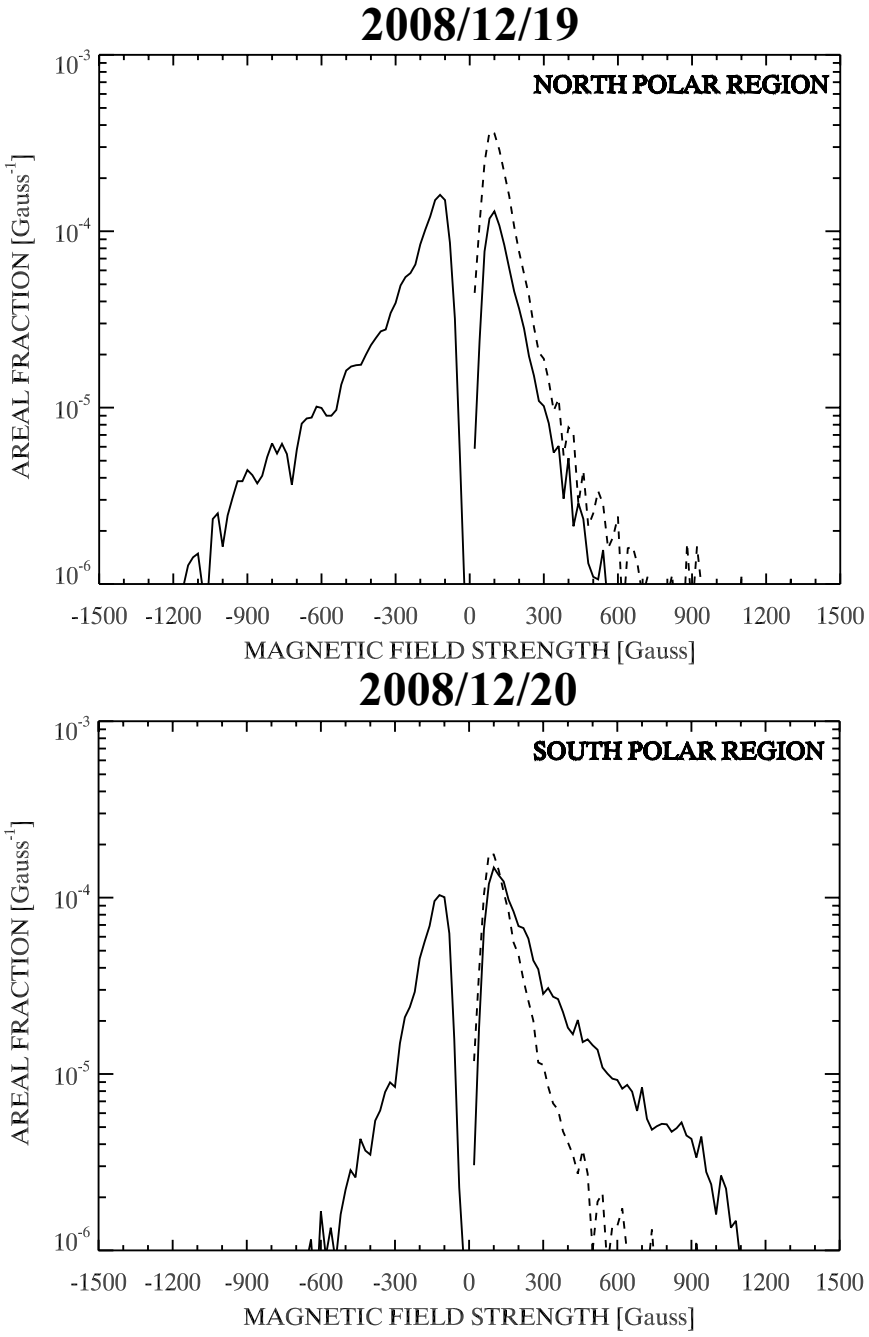

Figure 4.10: Areal fraction of the intrinsic magnetic field strength on 2008 December 19 for the North polar region (upper panel) and on 2008 December 20 for the South polar region (bottom panel). The meanings of the data are same as in Figure 4.4.

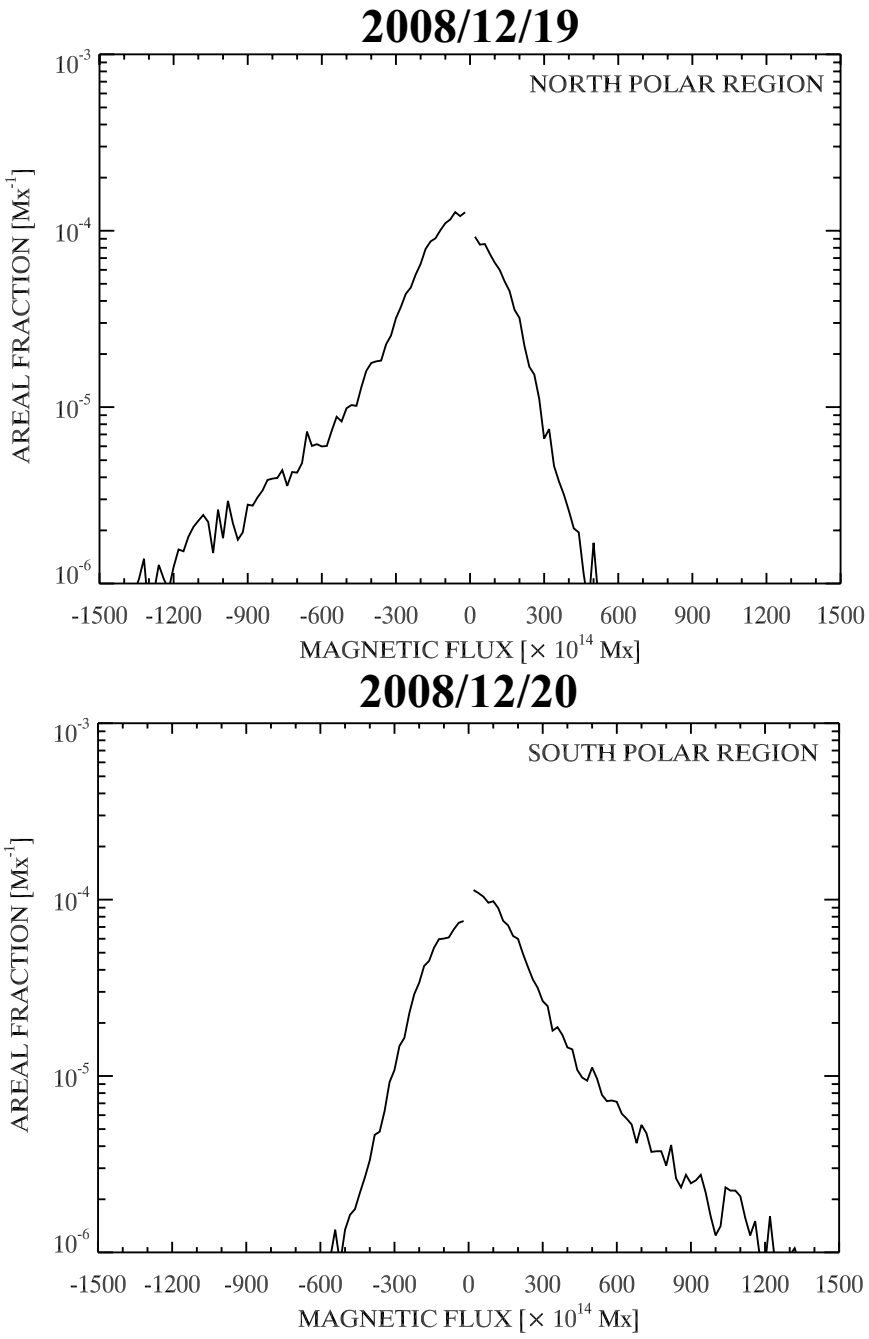

Figure 4.11: Areal fraction of the *vertical* magnetic flux on 2008 December 19 for the North polar region (upper panel) and on 2008 December 20 for the South polar region (bottom panel). The meanings of the data are same as in Figure 4.5.

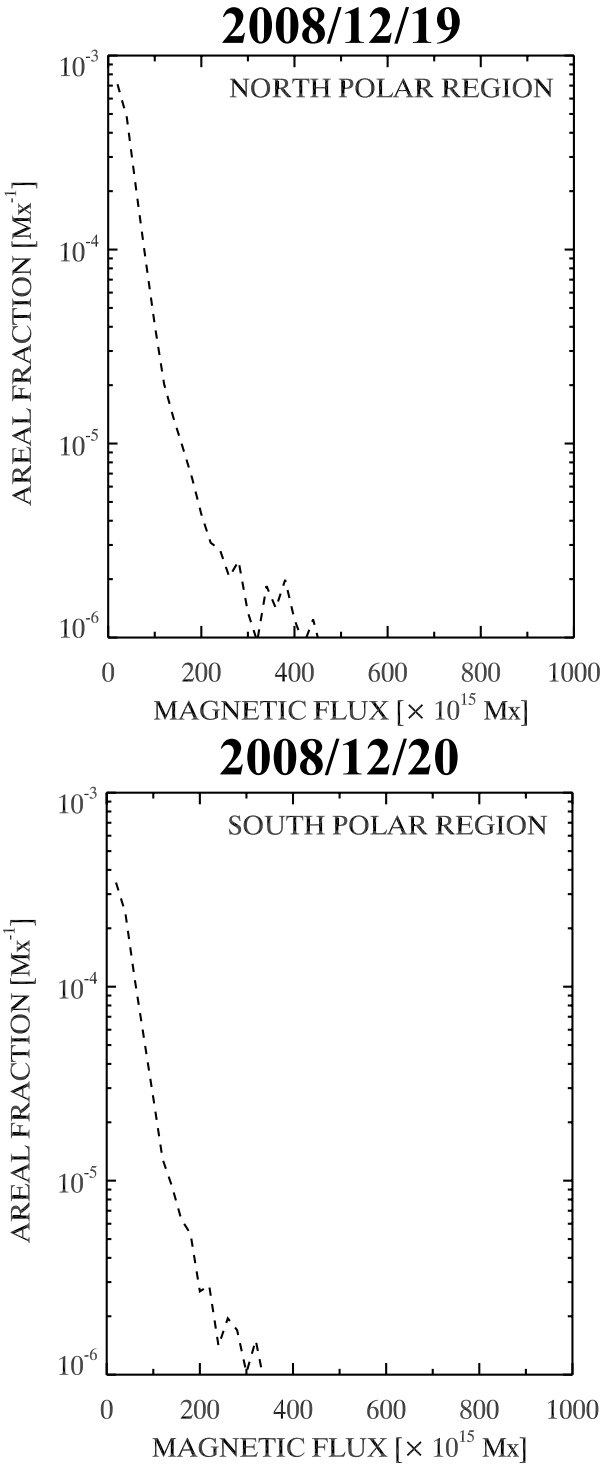

Figure 4.12: Areal fraction of the *horizontal* magnetic flux on 2008 December 19 for the North polar region (upper panel) and on 2008 December 20 for the South polar region (bottom panel). The meanings of the data are same as in Figure 4.6.

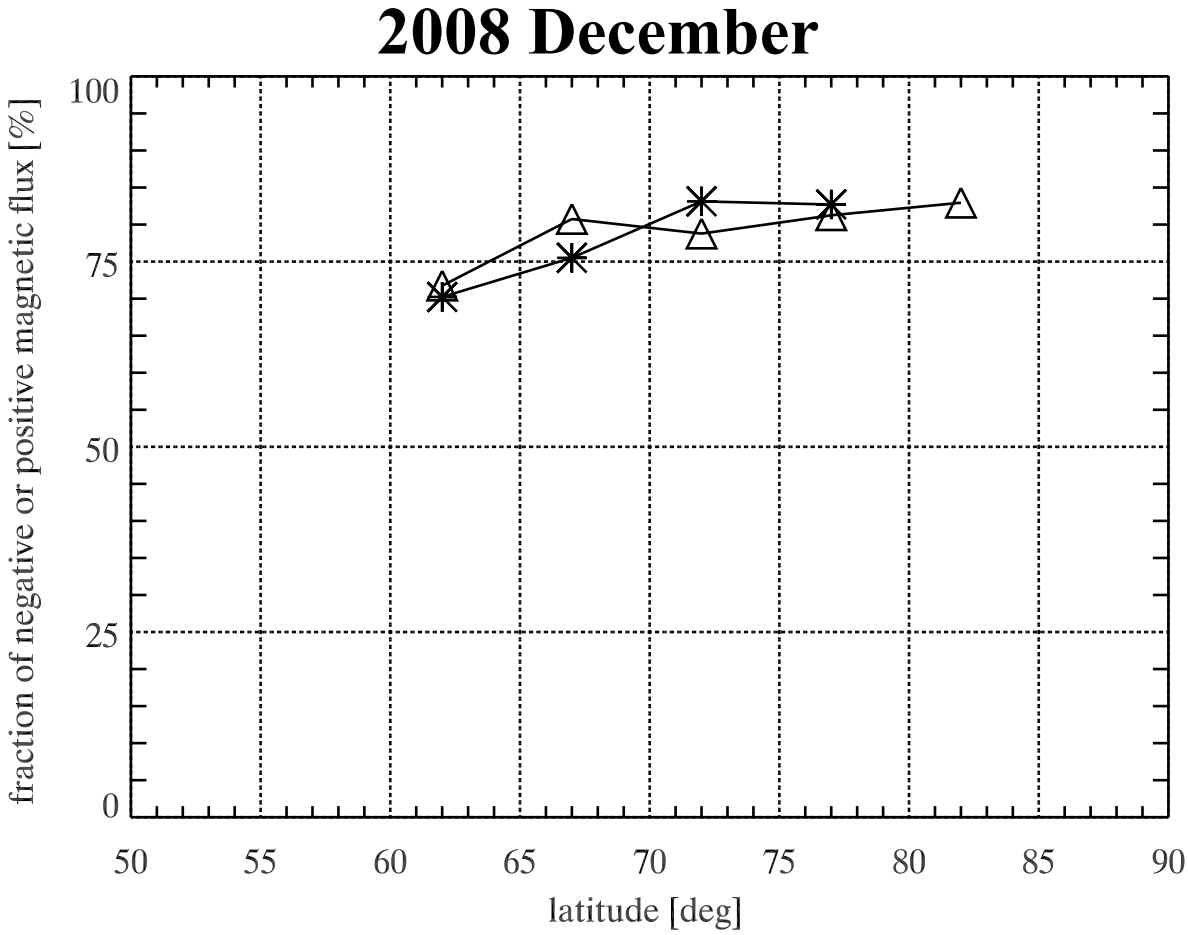

Figure 4.13: Areal fraction of the dominant magnetic flux in both the polar regions in 2008 December. The asterisks and triangles represent the averaged areal (over 5 degree) fraction of the magnetic flux with the dominant polarity in the North and South polar regions, respectively.

2009 December (beginning of Cycle 24)

December 2009 is the beginning of the Cycle 24. However the solar activity remains still low (Figure 4.1). We report the images and the histograms with format same as before (Figures 4.14 $\sim$ 4.19).

We find that the fraction of the dominant magnetic flux in the North polar region does not smoothly increase with latitude in the December 2009 data (Figure 4.19). We also notice some significant difference as compared with previous observations presented in this paper. In earlier observations, we do not find any kG-patches with minority polarity in the FOV, while in the December 2009 observations, we recognize kG-patch-like concentrations with opposite polarity at around 61 degree in the North polar region, and at around 74 degree in the South polar region. This may be consistent with the start of the Cycle 24, but we do not know how such kG-patch-like concentrations with minority polarity have formed. Figure 4.16 shows imbalance of the magnetic flux in kG-regime; excess at kG-regime is maintained in the South polar region, while that in North appears to be diminishing.

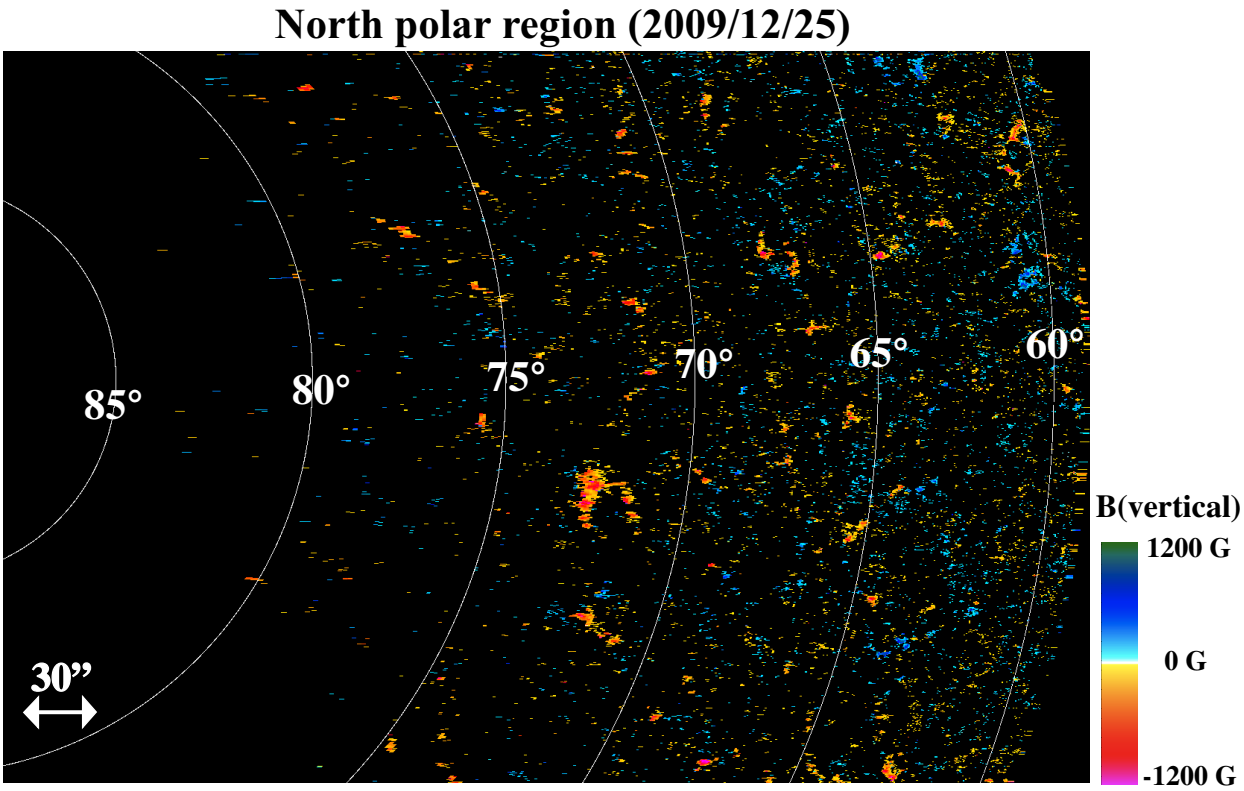

Figure 4.14: Map of signed strength of the magnetic field vectors classified as *vertical* (see section 2.4.1) in the North polar region of the Sun at 10:07—12:55 UT on 2009 December 25. The size of the FOV for the east-west direction is 314″.24. The size of the FOV for the North-South direction (163″.84) is expanded to 467″.2 as a result of correction for foreshortening. For other notations of the image, see the caption of Figure 4.2.

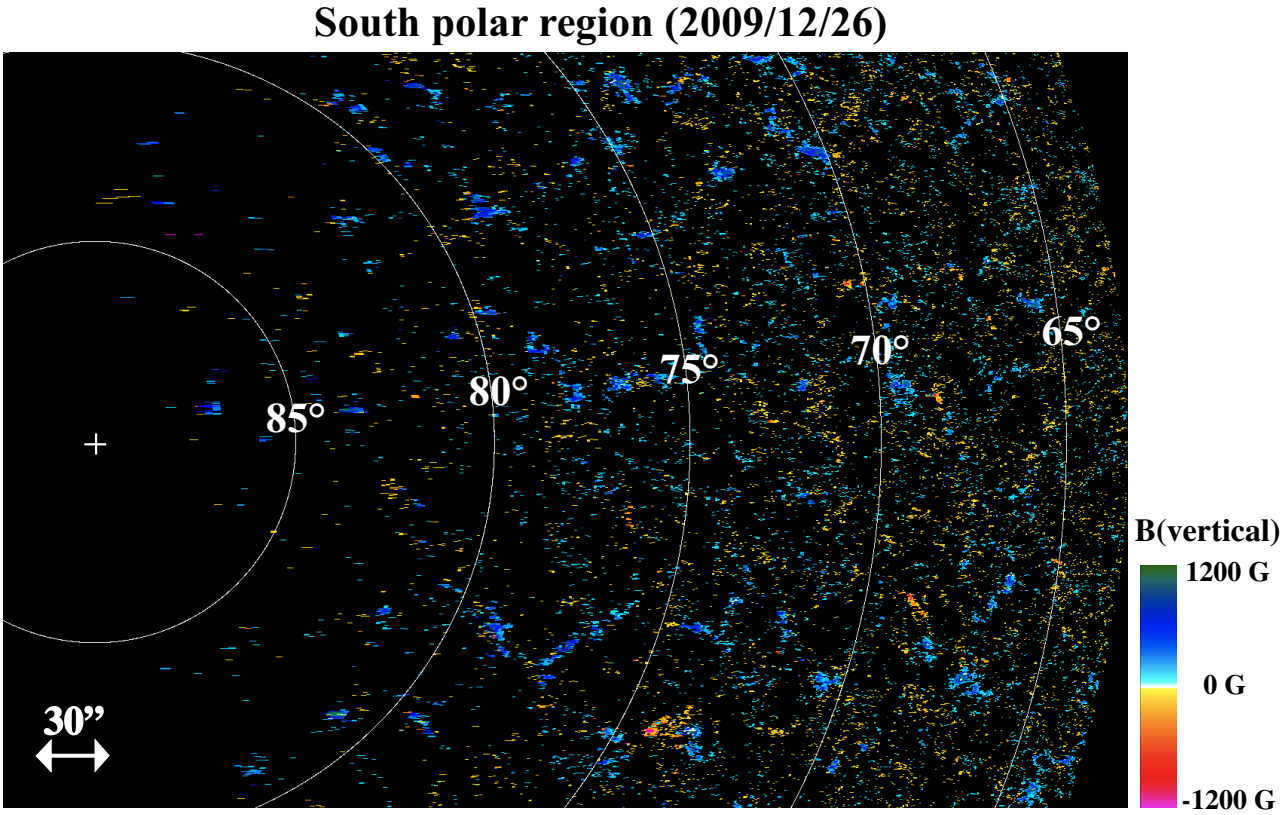

Figure 4.15: Map of signed strength of the magnetic field vectors classified as *vertical* (see section 2.4.1) in the South polar region of the Sun at 14:10—17:03 UT on 2009 December 26. The size of the FOV for the east-west direction is 320″.64. The size of the FOV for the North-South direction (163″.84) is expanded to 477″.76 as a result of correction for foreshortening. For other notations of the image, see the caption of Figure 4.3.

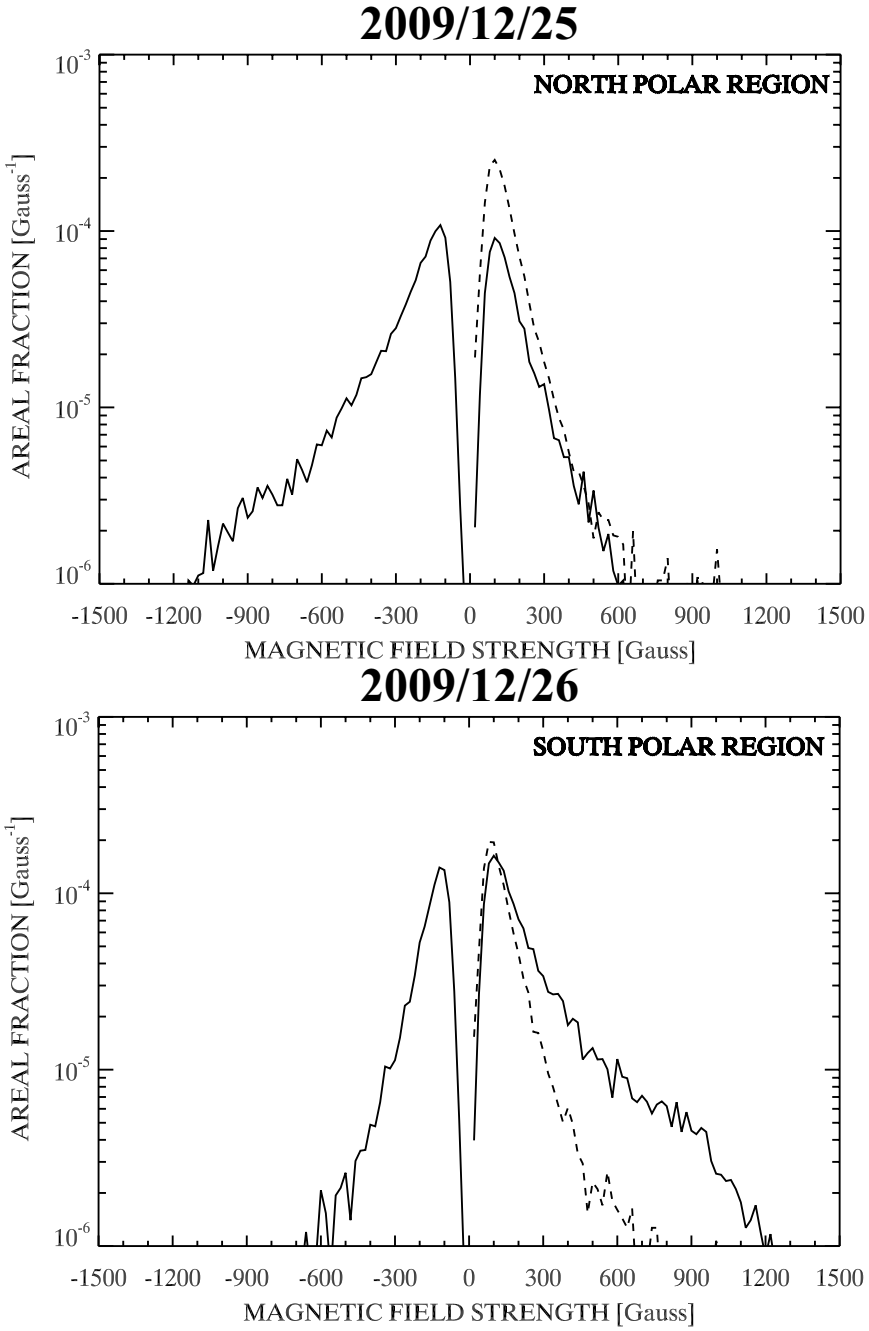

Figure 4.16: Areal fraction of the intrinsic magnetic field strength on 2009 December 25 in the North polar region (upper panel) and on 2009 December 26 in the South polar region (bottom panel). The meanings of the data are same as in Figure 4.4.

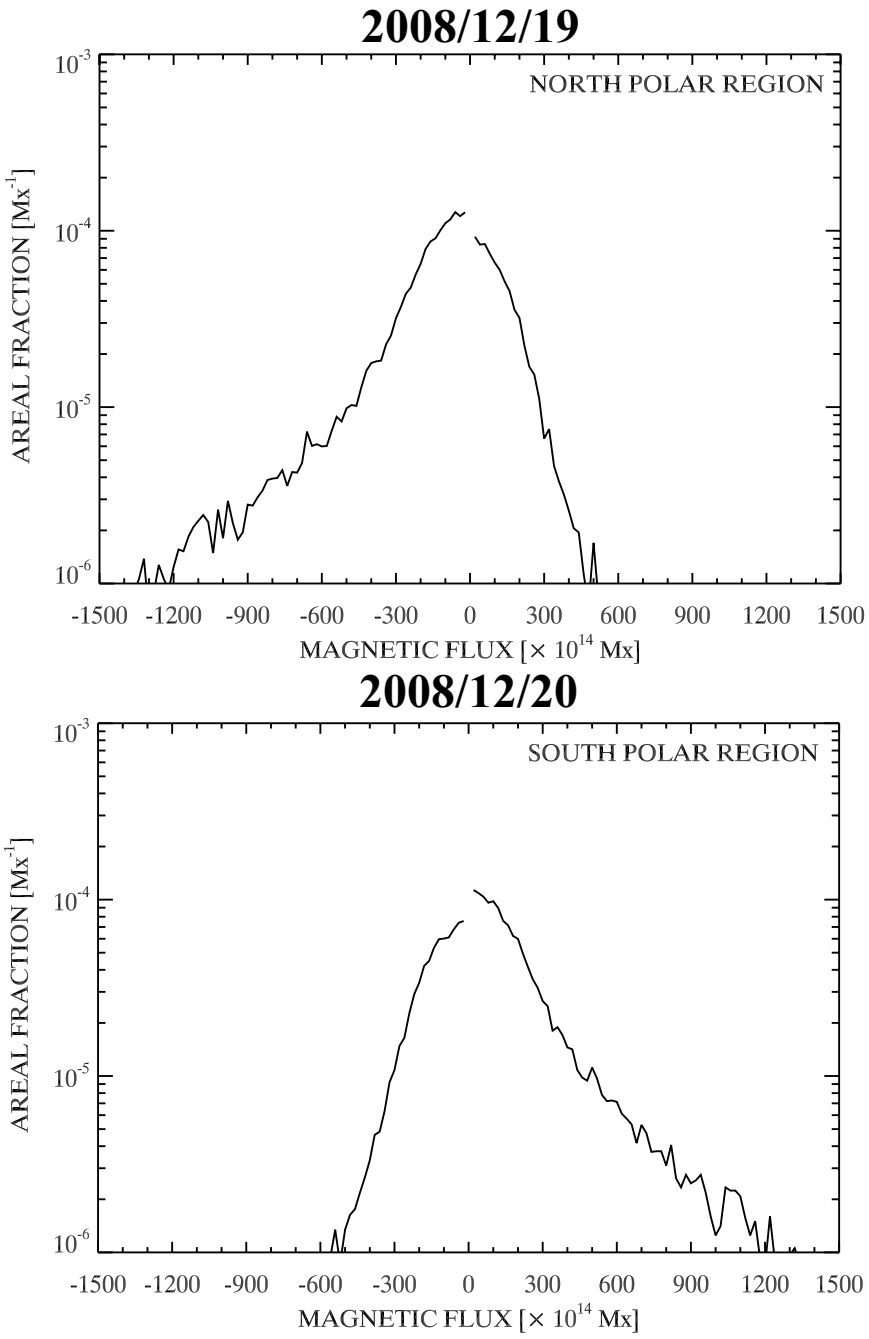

Figure 4.17: Areal fraction of the *vertical* magnetic flux on 2009 December 25 for the North polar region (upper panel) and on 2009 December 26 for the South polar region (bottom panel). The meanings of the data are same as in Figure 4.5.

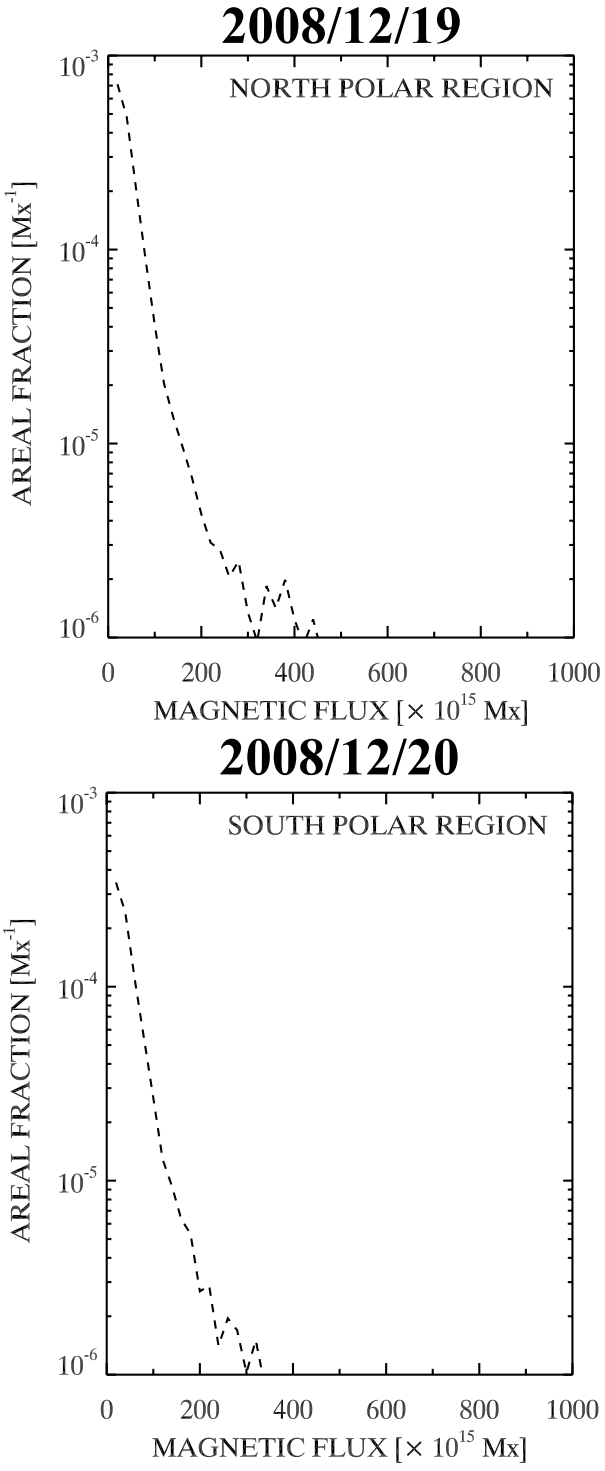

Figure 4.18: Areal fraction of the *horizontal* magnetic flux on 2009 December 25 for the North polar region (upper panel) and on 2009 December 26 for the South polar region (bottom panel). The meanings of the data are same as in Figure 4.6.

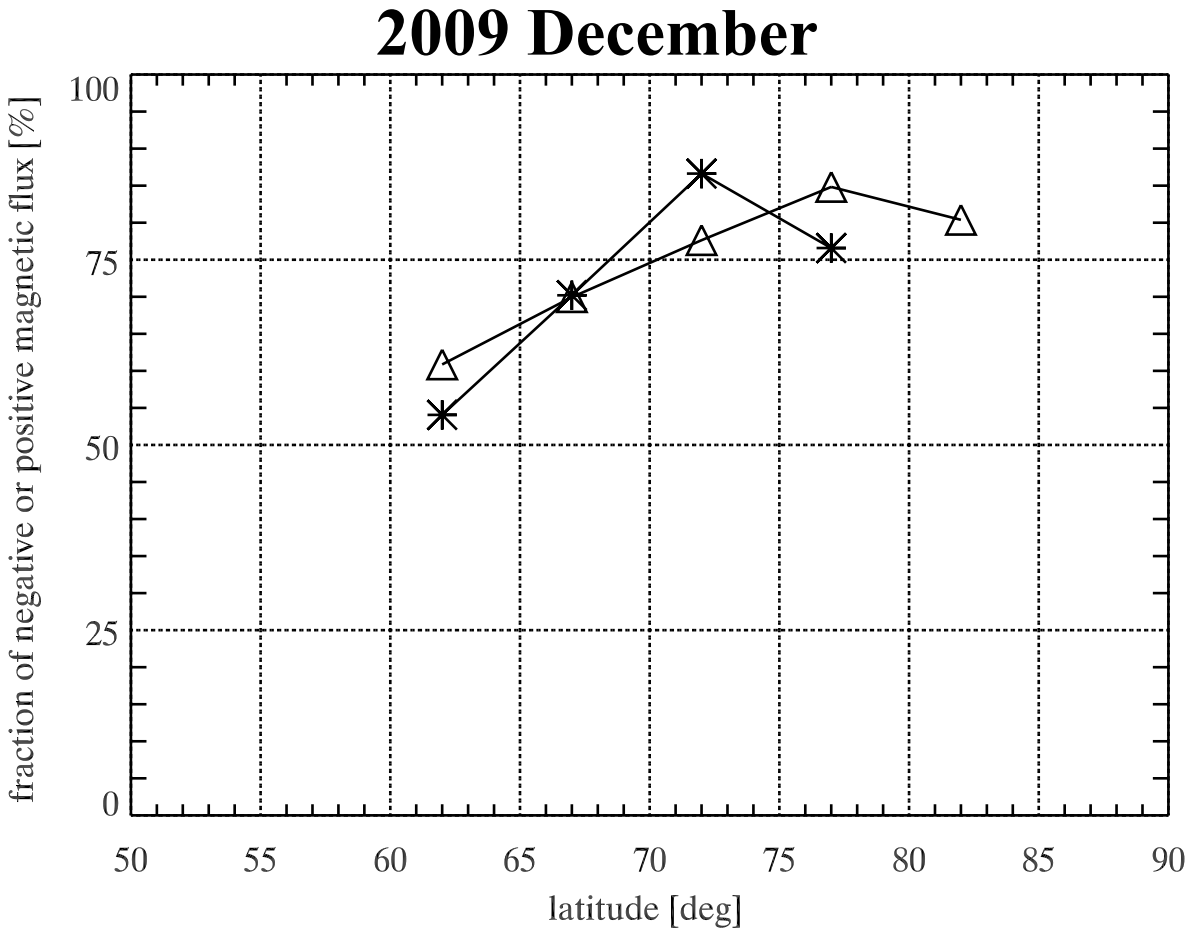

Figure 4.19: Areal fraction of dominant magnetic flux in both the polar region on 2009 December. The asterisks and triangles represent the averaged areal (over 5 degree) fraction of the magnetic flux with the dominant polarity in the North and South polar regions, respectively.

2011 January (rising phase of Cycle 24)

Observation January 2011 take place in the rising phase of the Cycle 24, and provide as with the latest date at the writing of this thesis. Since the solar activity increases (Figure 4.1), global magnetic field may begin to change. As usual, we present all the data sets.

The fraction between 70 and 80 degree in the North polar region is almost similar to that for the South polar region (Figure 4.25), while the fraction between 60 and 70 degree in the North polar region is smaller than that for the South polar region. This indicates that the magnetic fields of the minority polarity in between 60 and 70 degree are more enhanced in the North polar region than in the South polar region even in the very early phase of the solar cycle. There is no clearly definable boundary between the quiet Sun and the polar region. It is an extremely increasing and important topic on where the boundary of the polar coronal hole is located and what the corresponding photospheric signeture would be, if any.

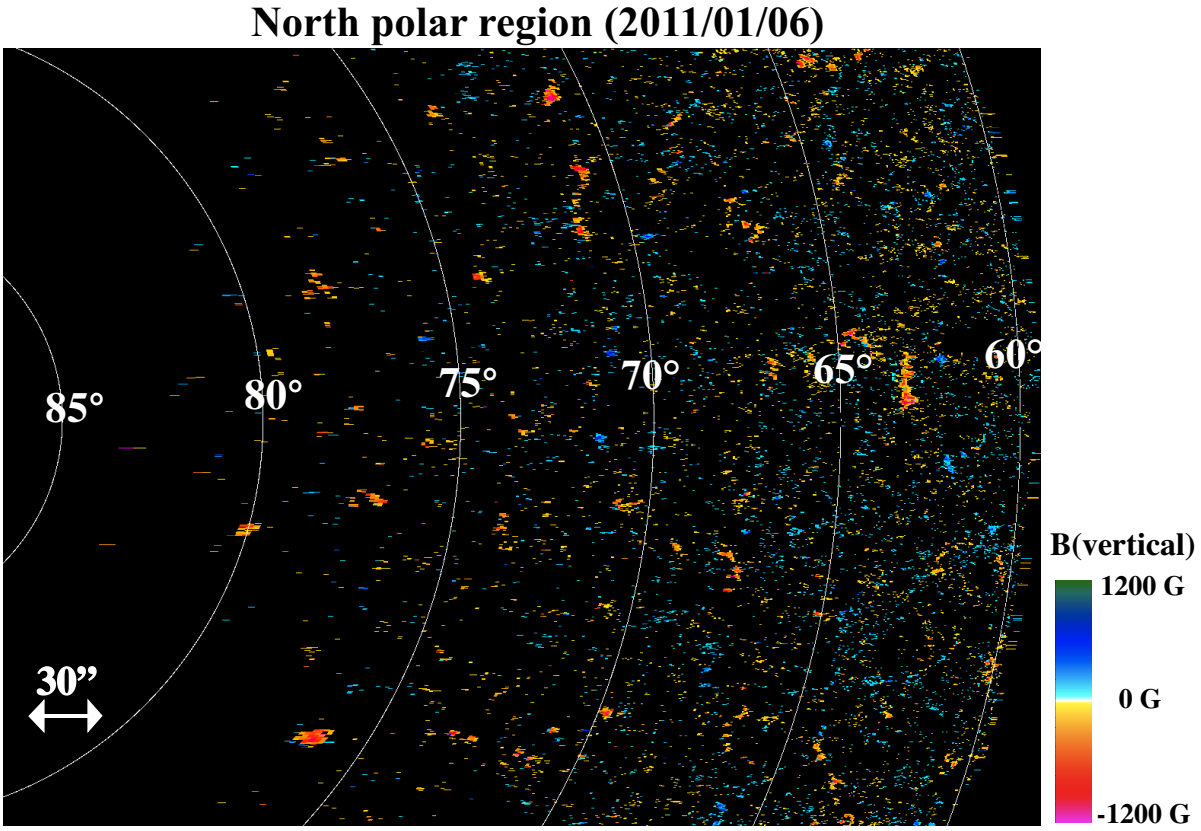

Figure 4.20: Map of signed strength of the magnetic field vectors classified as *vertical* (see section 2.4.1) in the North polar region of the Sun at 09:59—12:53 UT on 2011 January 6. The size of the FOV for the east-west direction is 326″.72. The size of the FOV for the North-South direction (163″.84) is expanded to 436″.48 as a result of correction for foreshortening. For other notations of the image, see the caption of Figure 4.2.

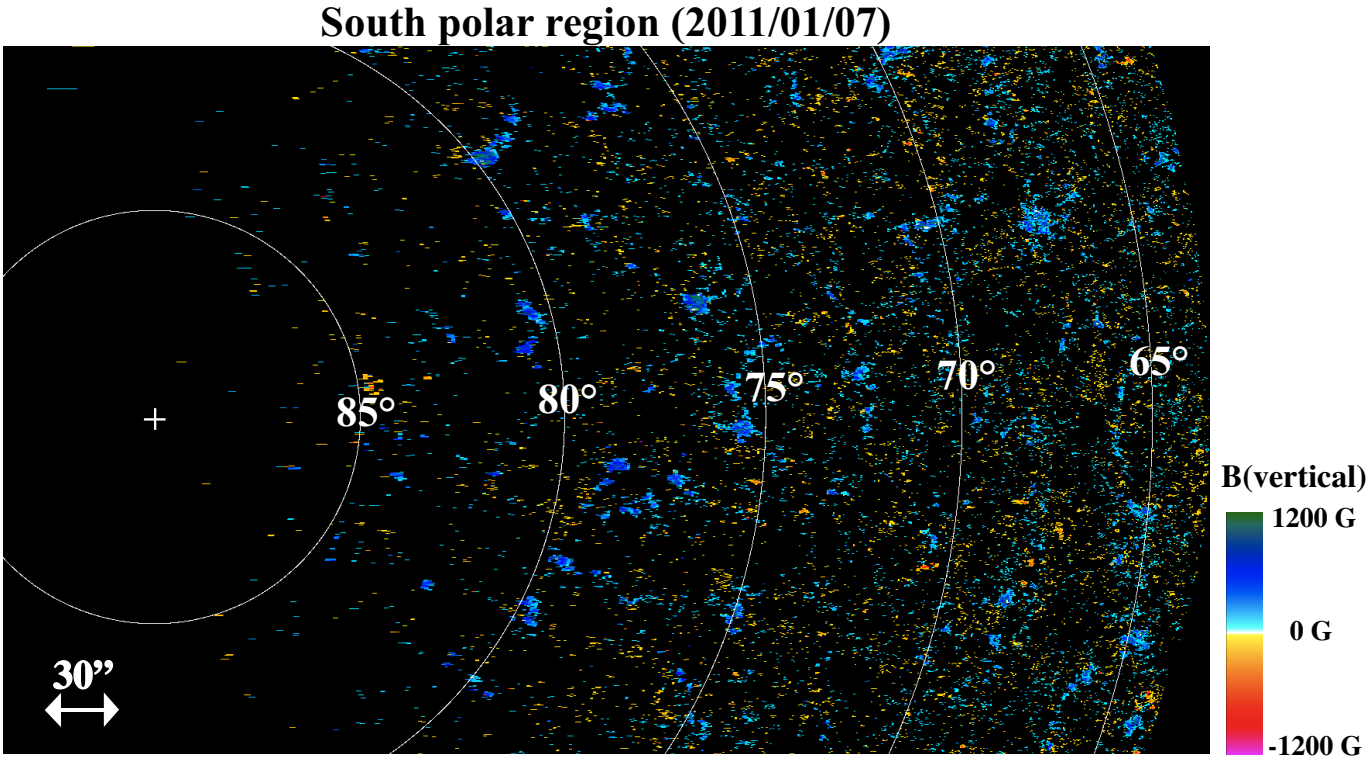

Figure 4.21: Map of signed strength of the magnetic field vectors classified as *vertical* (see section 2.4.1) in the South polar region of the Sun at 10:15—13:08 UT on 2011 January 7. The size of the FOV for the east-west direction is 292″.48. The size of the FOV for the North-South direction (163″.84) is expanded to 498″.88 as a result of correction for foreshortening. For other notations of the image, see the caption of Figure 4.3.

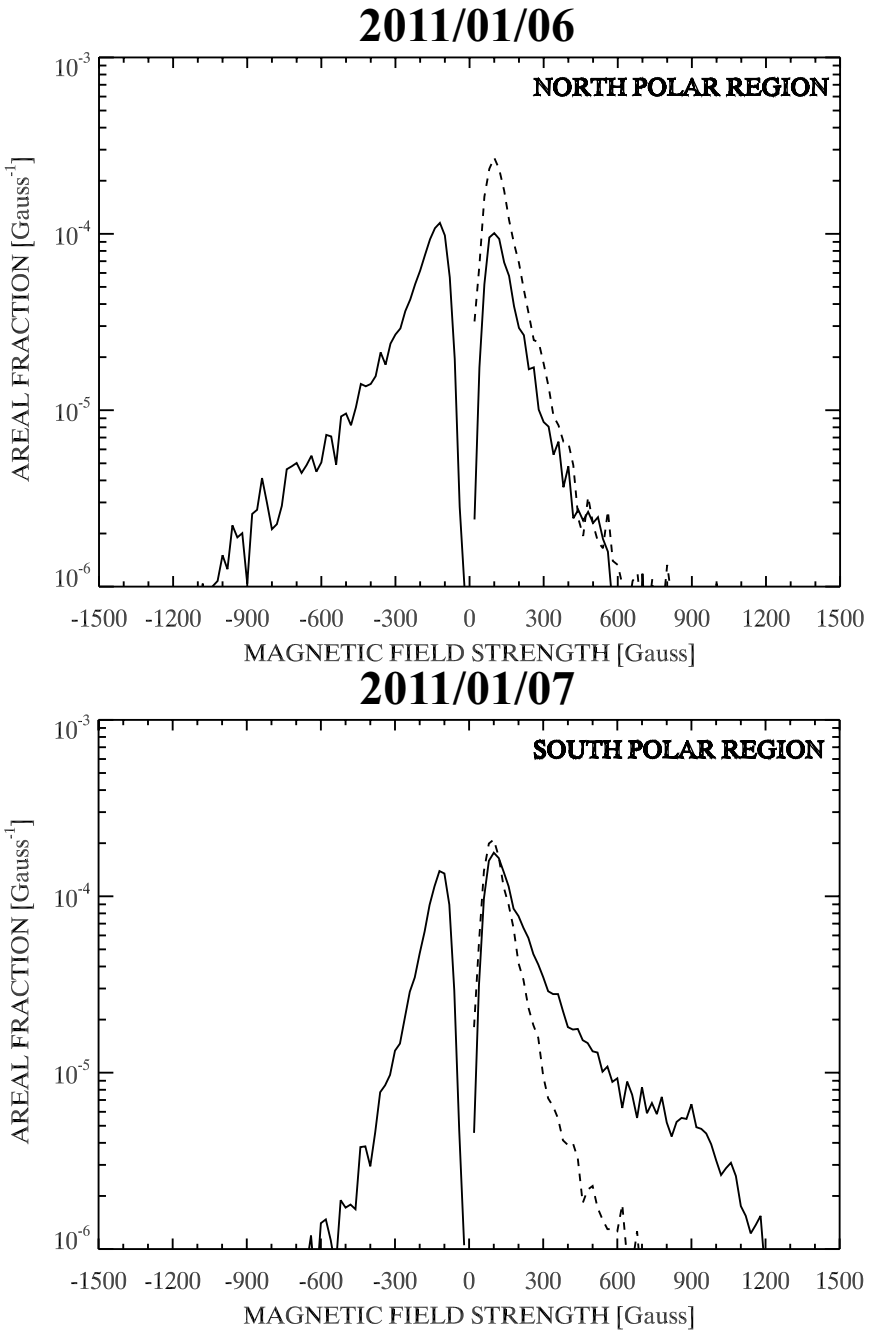

Figure 4.22: Areal fraction of the intrinsic magnetic field strength on 2011 January 6 in the North polar region (upper panel) and on 2011 January 7 in the South polar region (bottom panel). The meanings of the data are same as in Figure 4.4.

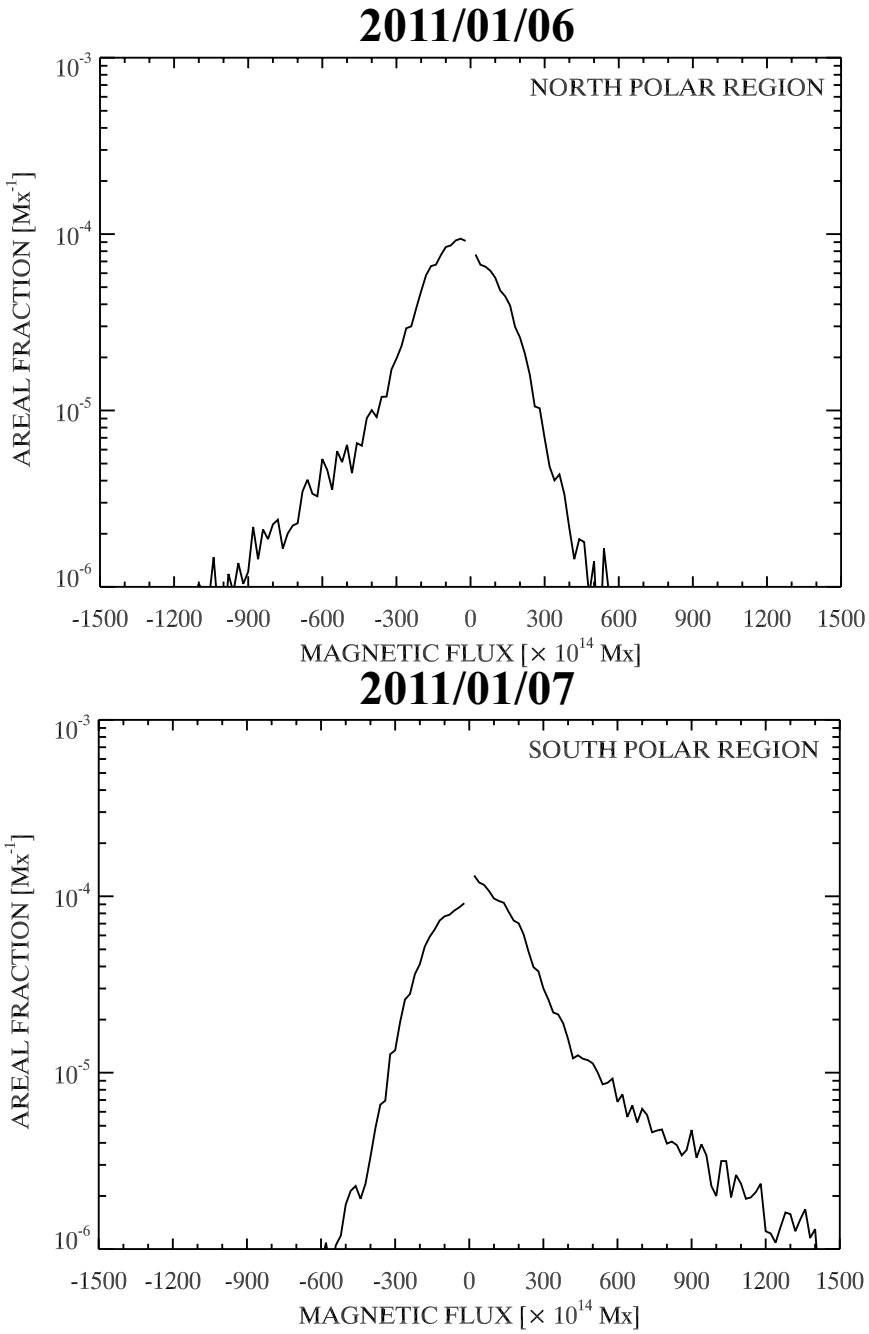

Figure 4.23: Areal fraction of the *vertical* magnetic flux on 2011 January 6 for the North polar region (upper panel) and on 2011 January 7 for the South polar region (bottom panel). The meanings of the data are same as in Figure 4.5.

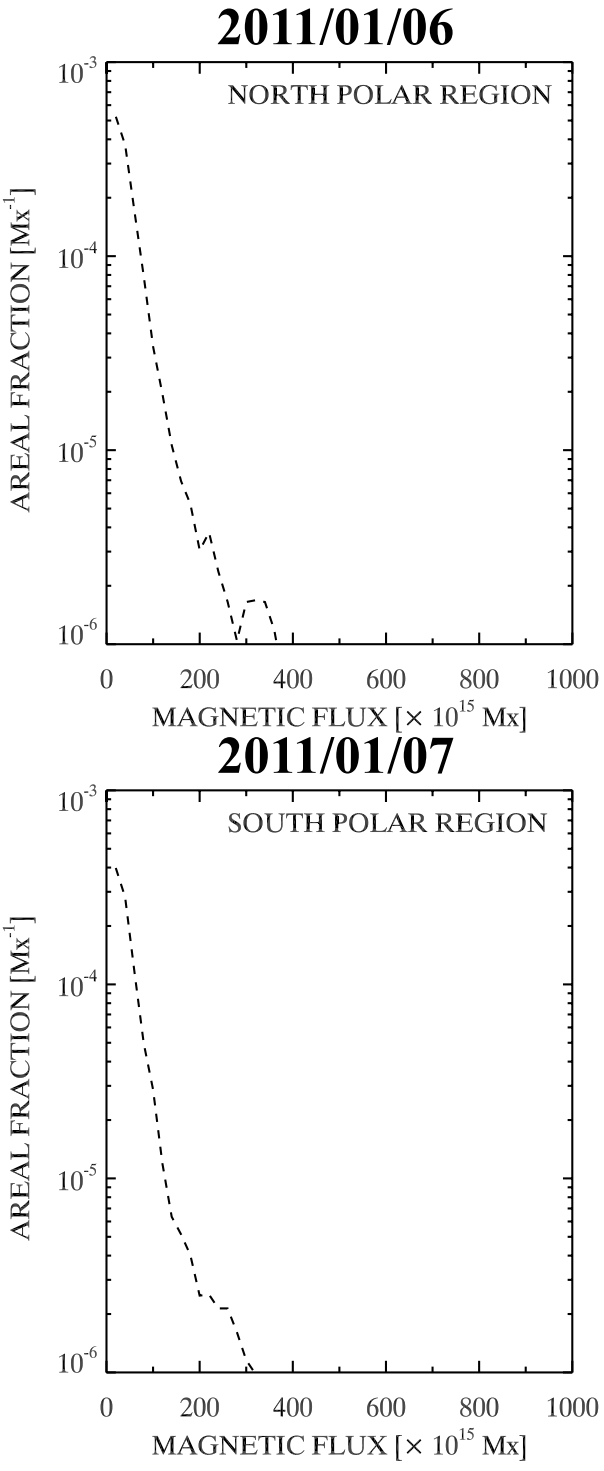

Figure 4.24: Areal fraction of the *horizontal* magnetic flux on 2011 January 6 for the North polar region (upper panel) and on 2011 January 7 for the South polar region (bottom panel). The meanings of the data are same as in Figure 4.6.

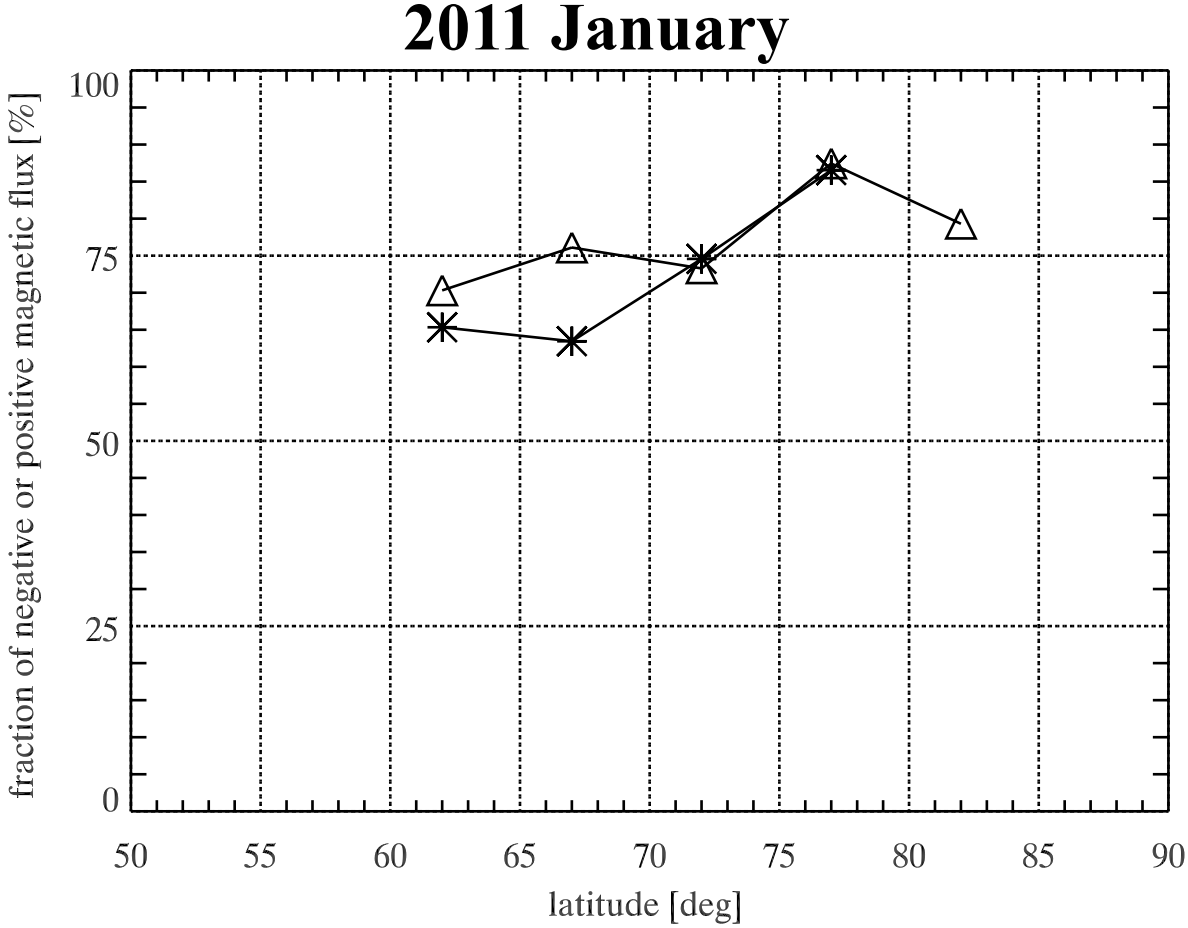

Figure 4.25: Areal fraction of dominant magnetic flux in both the polar region on 2011 January. The asterisks and triangles represent the averaged areal (over 5 degree) fraction of the magnetic flux with the dominant polarity in the North and South polar regions, respectively.

4.3 Discussion

4.3.1 Latitudinal Distribution

We here discuss the yearly variation of the latitudinal distribution of the magnetic fields. The averaged areal (over 5 degree) fraction of the dominant magnetic flux in the North and South polar regions shown in Figures 4.7, 4.13, 4.19, and 4.25, are shown in Figures 4.26 and 4.27, respectively.

In the North polar region, the fraction of the dominant magnetic flux essentially decreases from 2006 to 2011. In the latitudinal direction, the fraction increases with higher latitude, although we notice considerable fluctuation in latitude in 2009. The averaged areal fraction at $75 \sim 79$ degree in 2011 is 15 % smaller than that in 2006. This indicates that the minority polarity magnetic flux increases at high latitude. It is not clear with this observation that the increase of the minority flux is due to the advection of the active region magnetic flux, since only a small number of active regions exist in the lower latitude.

On the other hand, in the South polar region, the fraction of the dominant magnetic flux magnetic flux smoothly decreases with lower latitude for 4 years of observations (Figure 4.27). The fraction of the dominant magnetic flux does not monotonically decrease from 2006 to 2011. Interestingly, the faction between 60 and 70 degree in 2011 is about 5 % higher than that of 2009. This trend of magnetic flux in the South polar region is apparently different from that of North polar region. There is the asymmetrical nature between the North and South polar region in this period.

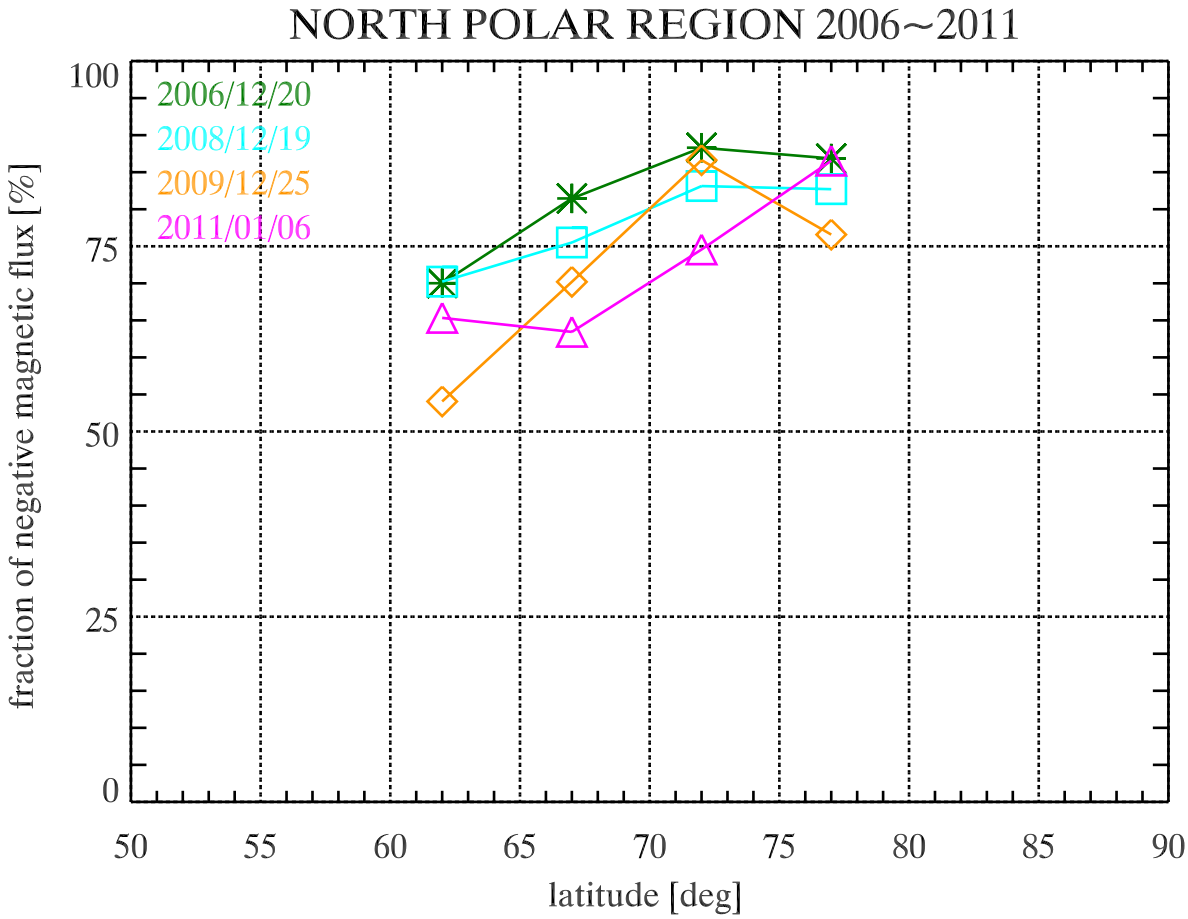

Figure 4.26: Fraction of dominant magnetic flux in the North polar region between 2006 and 2011. The green asterisks, cyan squares, yellow diamonds and magenta triangles represent the fraction on 2006 December, 2008 December, 2009 December and 2011 January, respectively. The plots are the average of the fractions over -2.5 $\sim$ 2.5 degree.

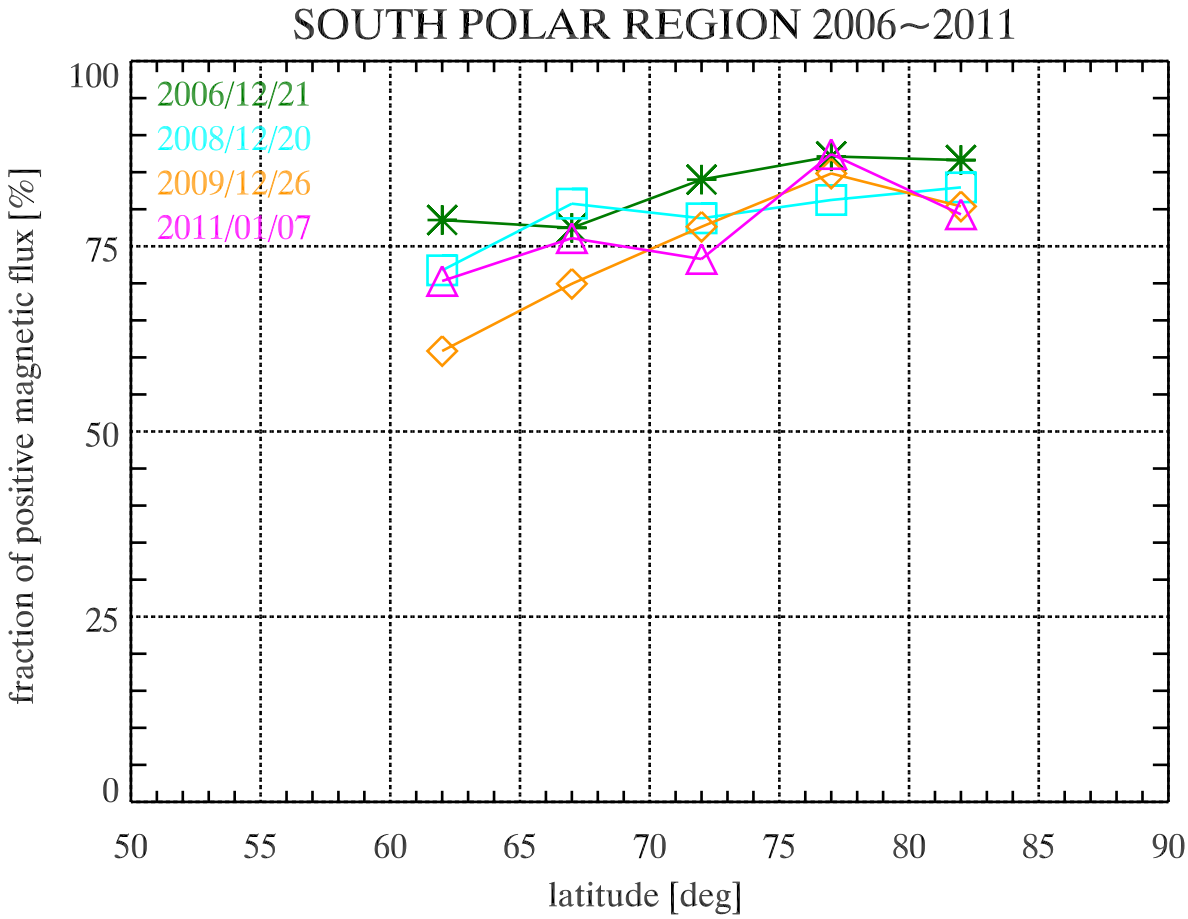

Figure 4.27: Fraction of dominant magnetic flux in the South polar region between 2006 and 2011. The green asterisks, cyan squares, yellow diamonds and magenta triangles represent the fraction on 2006 December, 2008 December, 2009 December and 2011 January, respectively. The plots are the average of the fractions for each 5 degree.

4.3.2 Distribution of Vertical and Horizontal Field

The areal fraction (histogram) of the intrinsic magnetic field strength in the North and South polar regions shown in Figures 4.4, 4.10, 4.16, and 4.22 are presented again in Figures 4.28, 4.29, 4.30, and 4.31. Those for magnetic flux are shown in Figures 4.32 $\sim$ 4.35. As shown in section 4.2, only N06 and S06 are observed with different mode of SOT/SP where pixels with weak fields tend to be missed. Therefore, the areal fractions of N06 and S06 should be much smaller in weak field pixels. We thus do not directly compare the areal fractions for 2006 with those for 2008, 2009, and 2011.

The distribution of the vertical magnetic fields in the North polar region is highly asymmetric, showing a predominance of one polarity (Figure 4.28). Fractional number of pixels with intrinsic field strength of -1 kG is the smallest in N11 data. The number of pixels with intrinsic field strength of -1 kG decrease with time.

The distribution of vertical magnetic fields in the South polar region is also highly asymmetric, showing a predominance of one polarity (Figure 4.29). In contrast to that in the North polar region, the fractional number of pixels of 1 kG is almost the same in S08, S09 and S11.

The distributions of the horizontal magnetic fields in the South polar regions are almost the same from 2008 to 2011 (Figure 4.31), while in the North polar region, the peaks at around 100 G somewhat decrease with time. (The data taken in 2006 should not be compared with other data.) There is little difference in the regime above 200 G in the North polar region. Ito et al. (2010) repored that that the areal fraction of the intrinsic magnetic field strength for the horizontal magnetic fields are exactly the same in the polar region and the quiet Sun. This may support that the horizontal magnetic fields are created by the local dynamo process. The only difference in the histograms is the peak areal fraction in the North polar region. The turnover of the histograms at around 100 G would be due to the limited sensitivity of polarization signals. Slight unknown difference may sensitively affect the peak. Except for the difference in the peak value between 2008 and 2009, all other data show exceptional coincidence.

Figures 4.36 and 4.37 show the yearly variation of the magneticflux density of the vertical and horizontal magnetic fields. The magnetic flux densities (κ_v, κ_h) of

the vertical and horizontal magnetic fields are given by

$$\kappa_v = \frac{\sum B_j \cos i_j f_j s_j}{\sum s_j}, \tag{4.1}$$

$$\kappa_h = \frac{\sum B_j \sin i_j L_j H_j}{\sum s_j}, \tag{4.2}$$

where B_j and i_j , and f_j are the intrinsic magnetic field strength and the inclination angle obtained with Equations 2.17 and 2.18, and the filling factor of the j-th SOT pixel inside the SOT/SP FOV, respectively, and s_j is the pixel size. L_j is the linear size of the pixel size and is commonly $0''.32$. H_j is the diameter of the horizontal flux tubes and is commonly assumed to be 190 km, following Ishikawa, Tsuneta, and Jurčák (2010). The horizontal magnetic flux density in the North polar region is somewhat different from that of the South polar regon. The horizontal magnetic flux density is almost constant for the South polar region, while that of the North polar region may be slightly different. We compared the derived average signed vertical magnetic flux density with the polar magnetic flux density between 55 and 90 degree by Wilcox Solar Observatory (WSO) between 2006 and 2011. WSO has observed the magnetic flux of the Sun since 1976. Only the LOS component of the magnetic flux is obtained with modest spatial resolution. Near the solar limb, the LOS approaches to the horizontal direction so that the LOS observation may detect the horizontal magnetic fields, which may potentially contaminate the observed vertical magnetic fields. On the other hand, we obtained the vertical magnetic flux from the intrinsic magnetic field strengths, the filling factor and the inclination. Our results are obviously more accurate than the conventional observations. As shown in Figure 4.36, the vertical magnetic flux density with *Hinode* in the South polar region slightly is larger than that of North polar region except for 2008 data. The magnetic flux densities in both the polar regions do not roughly coincide with the magnetic flux density by WSO.

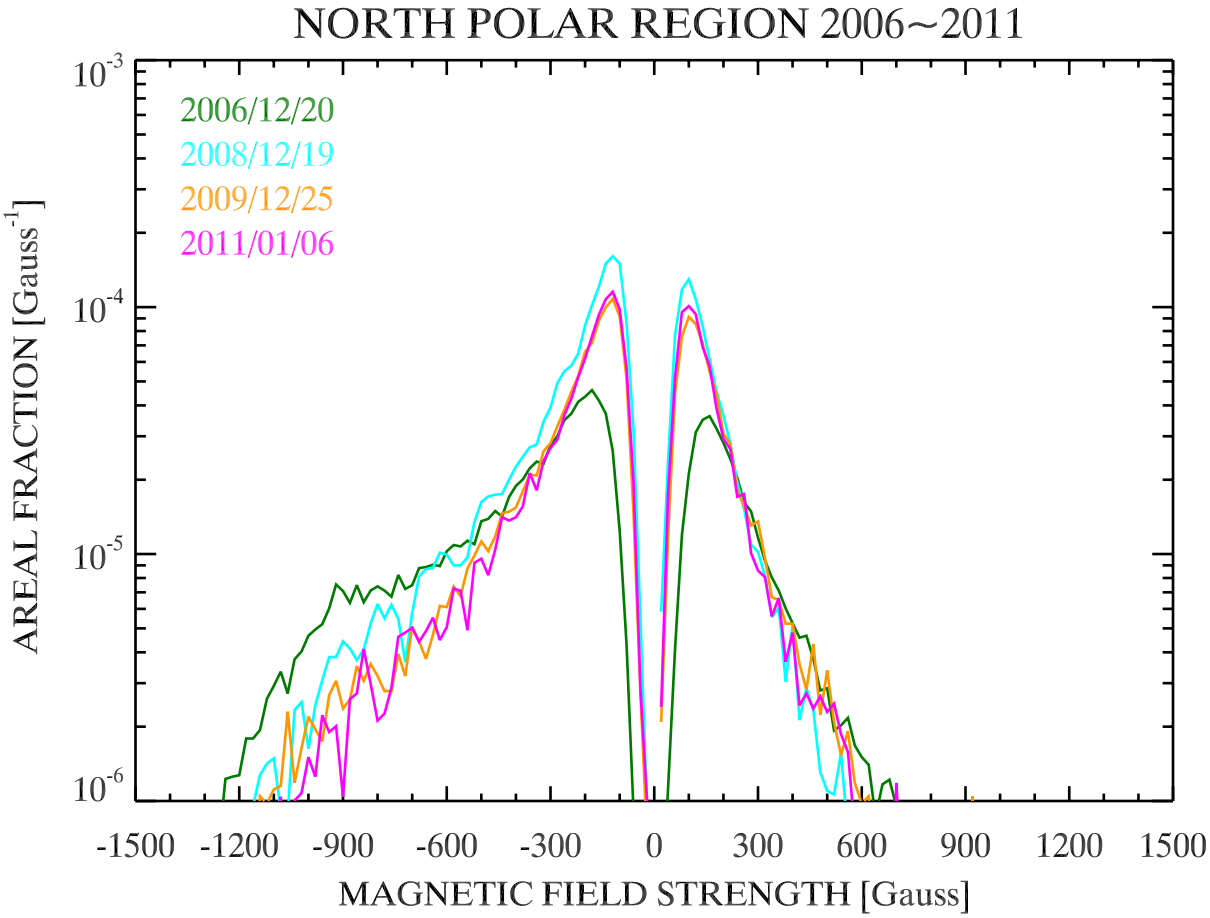

Figure 4.28: Areal fraction of the intrinsic *vertical* magnetic field strength between 2006 and 2011 in the North polar region. The green, cyan, yellow and magenta represent the fraction on 2006 December, 2008 December, 2009 December and 2011 January, respectively. The magnetic fields are classified as *vertical* or *horizontal* in this work (see section 2.4.1 for details), respectively.

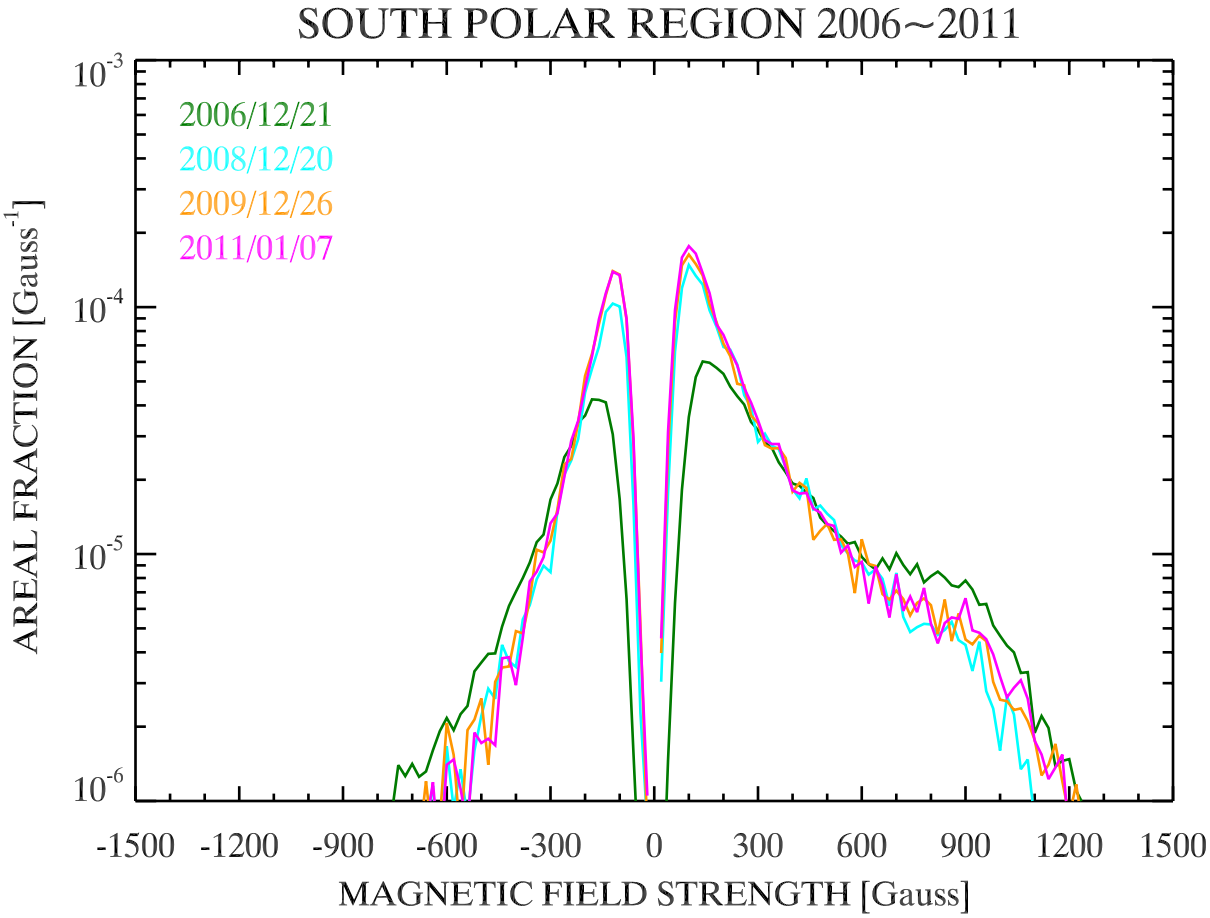

Figure 4.29: Areal fraction of the intrinsic *vertical* magnetic field strength between 2006 and 2011 in the South polar region. The green, cyan, yellow and magenta represent the fraction on 2006 December, 2008 December, 2009 December and 2011 January, respectively. The magnetic fields are classified as *vertical* or *horizontal* in this work (see section 2.4.1 for details), respectively.

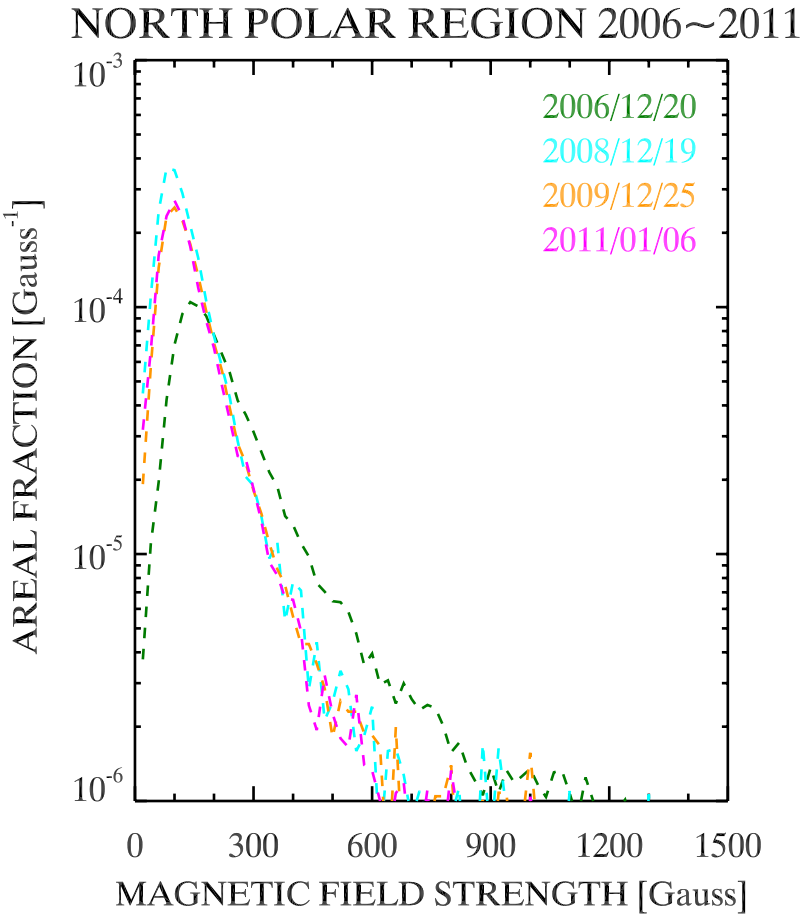

Figure 4.30: Areal fraction of the intrinsic *horizontal* magnetic field strength between 2006 and 2011 in the North polar region. The green, cyan, yellow and magenta dashed lines represent the fraction on 2006 December, 2008 December, 2009 December and 2011 January, respectively. The magnetic fields are classified as *vertical* or *horizontal* in this work (see section 2.4.1 for details), respectively.

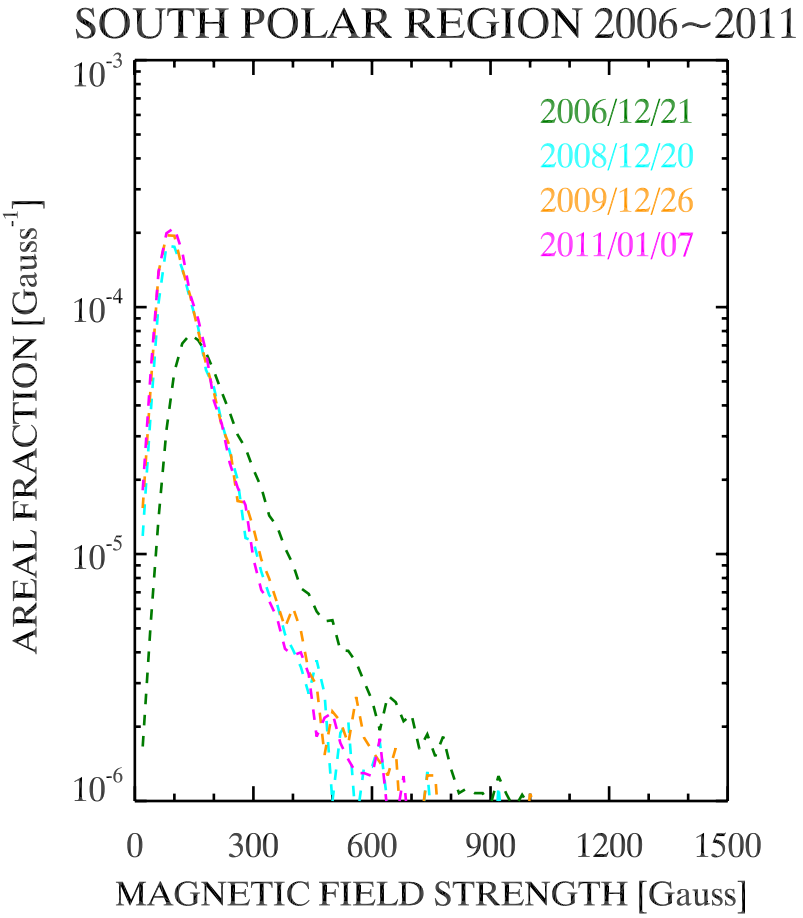

Figure 4.31: Areal fraction of the intrinsic *horizontal* magnetic field strength between 2006 and 2011 in the South polar region. The green, cyan, yellow and magenta dashed lines represent the fraction on 2006 December, 2008 December, 2009 December and 2011 January, respectively. The magnetic fields are classified as *vertical* or *horizontal* in this work (see section 2.4.1 for details), respectively.

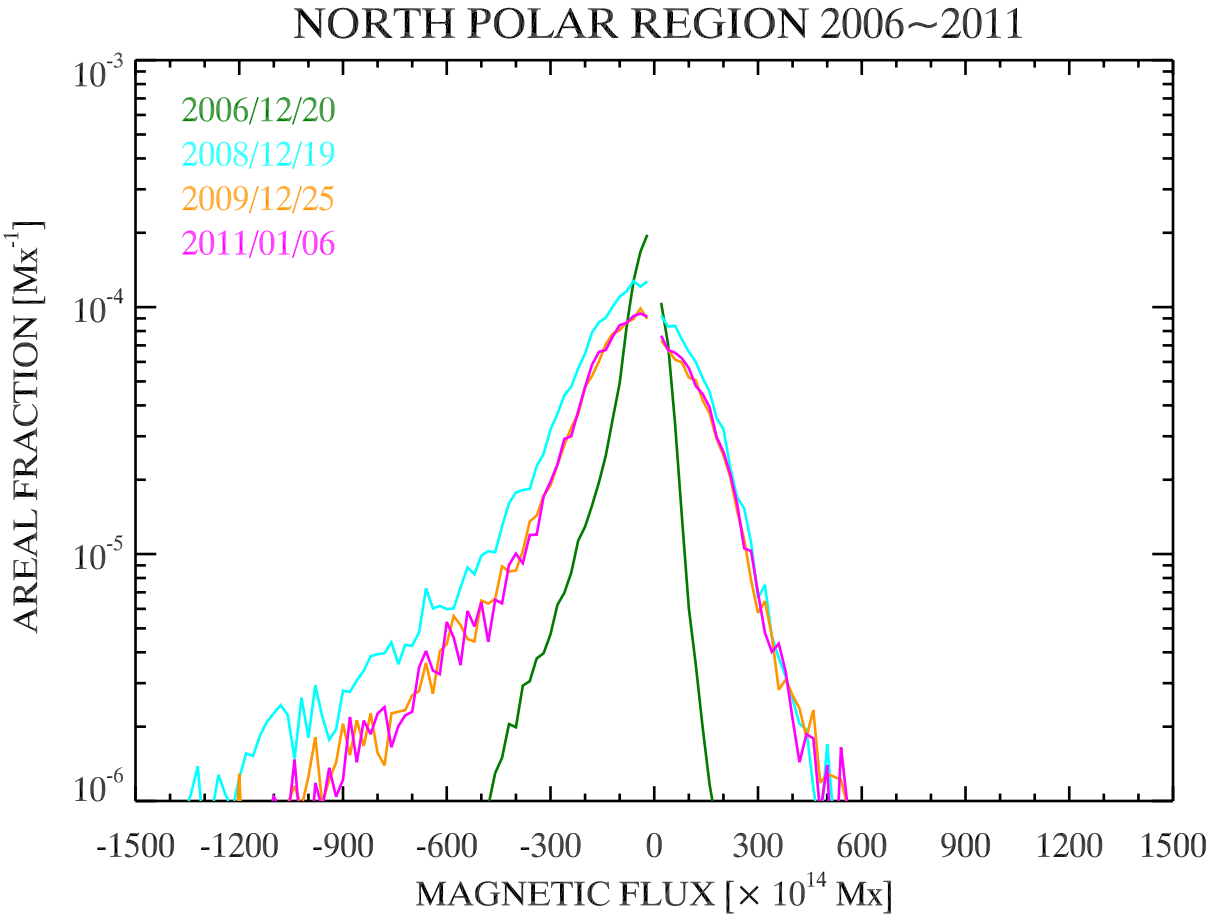

Figure 4.32: Areal fraction of the *vertical* magnetic flux between 2006 and 2011 in the North polar region. The green, cyan, yellow and magenta represent the fraction on 2006 December, 2008 December, 2009 December and 2011 January, respectively. The magnetic fields are classified as *vertical* or *horizontal* in this work (see section 2.4.1 for details), respectively.

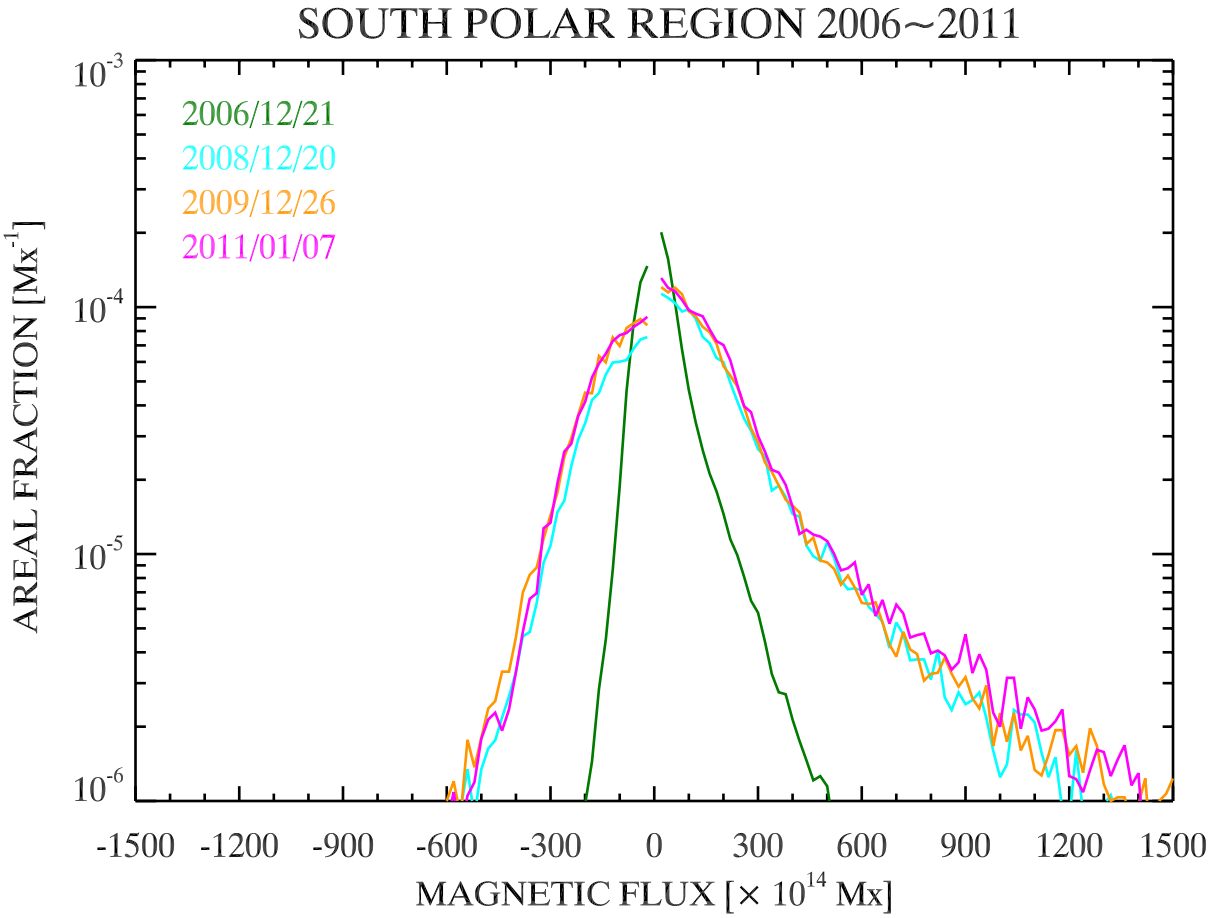

Figure 4.33: Areal fraction of the *vertical* magnetic flux between 2006 and 2011 in the South polar region. The green, cyan, yellow and magenta represent the fraction on 2006 December, 2008 December, 2009 December and 2011 January, respectively. The magnetic fields are classified as *vertical* or *horizontal* in this work (see section 2.4.1 for details), respectively.

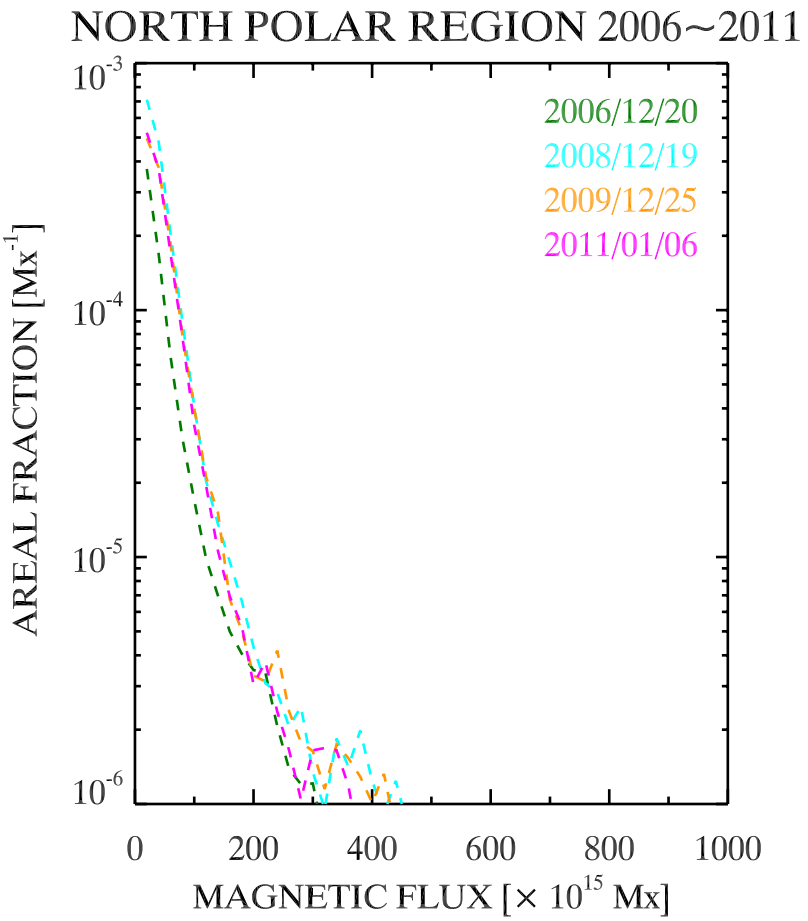

Figure 4.34: Areal fraction of *horizontal* magnetic flux between 2006 and 2011 in the North polar region. The green, cyan, yellow and magenta represent the fraction on 2006 December, 2008 December, 2009 December and 2011 January, respectively. The magnetic fields are classified as *vertical* or *horizontal* in this work (see section 2.4.1 for details), respectively.

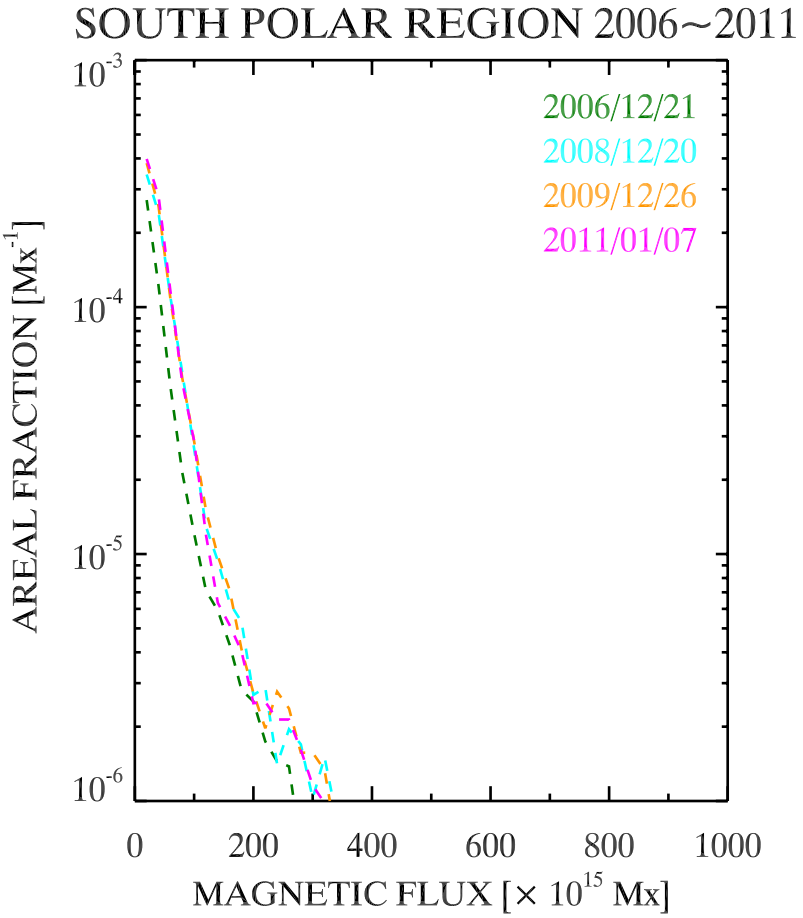

Figure 4.35: Areal fraction of the *horizontal* magnetic flux between 2006 and 2011 in the South polar region. The green, cyan, yellow and magenta represent the fraction on 2006 December, 2008 December, 2009 December and 2011 January, respectively. The magnetic fields are classified as *vertical* or *horizontal* in this work (see section 2.4.1 for details), respectively.

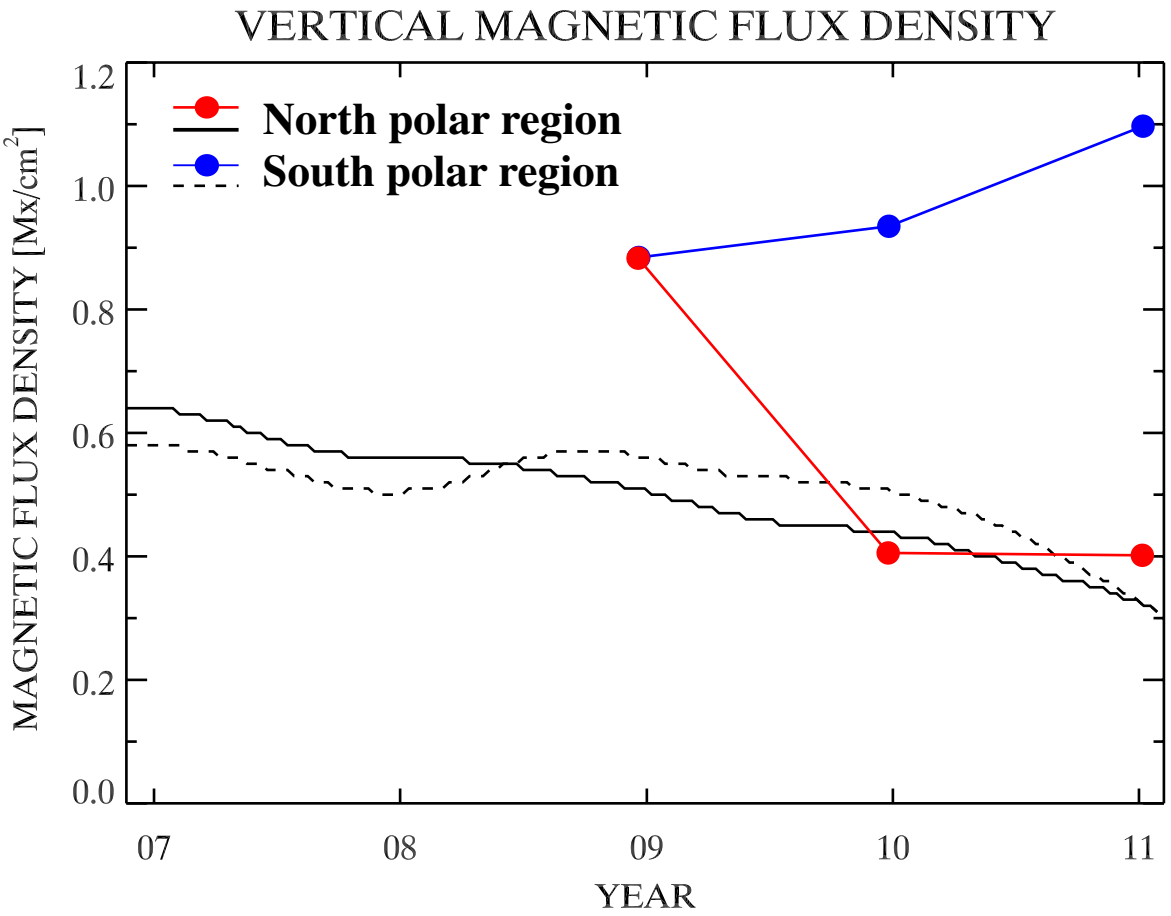

Figure 4.36: *Vertical* magnetic flux density of the polar regions in 2006 $\sim$ 2011. The red and blue dot represent the *vertical* magnetic flux density in the North and South polar regions, respectively. The polar magnetic flux density (average in 55 $\sim$ 90 degree) observed by Wilcox Solar Observatory are represented with the black solid and dashed lines, respectively.

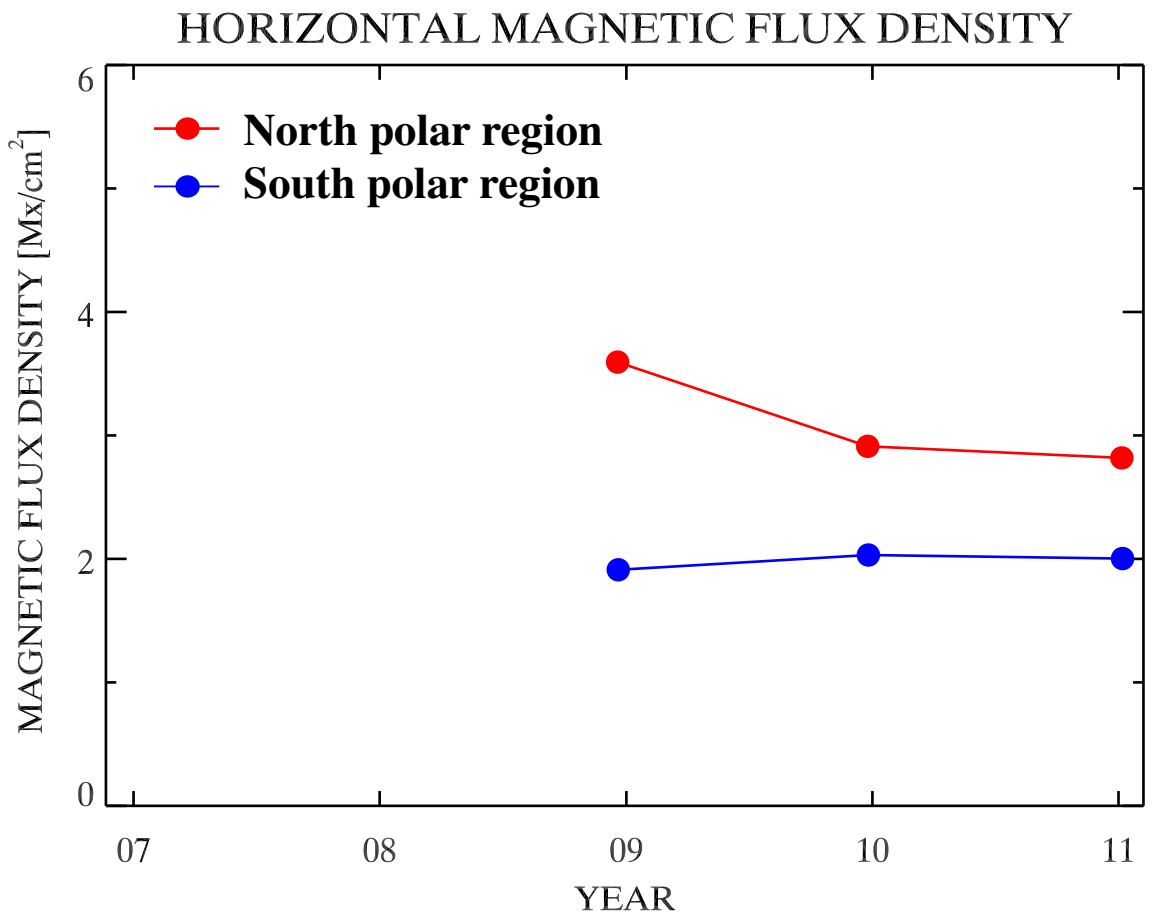

Figure 4.37: *Horizontal* magnetic flux density in both polar region between 2006 and 2011. The red and blue dot represent the *horizontal* magnetic flux density in the North and South polar region, respectively.

4.4 Summary

In this section, we have investigated the long term variation of the magnetic fields in the polar regions around solar minimum with high spatial resolution for the first time. We have presented the temporal and latitudinal variations of polar magnetic fields from December 2006, through January 2011. We essentially show that the fraction of the dominant vertical magnetic flux increases with latitude and slightly decreases with time.

We examine the temporal variation of vertical and horizontal magnetic fields. The comparison of their areal fraction of the magnetic flux showed that those of the vertical field vary, while those of the horizontal field are almost the same. The the vertical magnetic flux in the South polar region slightly is larger than that of North polar region except for end 2008 data. The horizontal magnetic flux density is almost constant for the South polar region, while that of the North polar region may be slightly different. This has to be examined carefully. There may be an effect of the slight difference in the B-angles.

Chapter 5

Summary and Future Works

5.1 General Summary

In this thesis, we have described the properties of the photospheric magnetic fields in the polar regions of the Sun. We also have presented a method to determine the photospheric magnetic vectors against the 180-degree ambiguity in the Stokes polarimetry near the solar limb. The method allows us to analyze the details of the photospheric magnetic field structure near the solar limb. The comparison between the quiet region and the North polar region showed different distributions of the magnetic field strength/flux and the polarities. Positive and negative magnetic fields are well balanced in the quiet region, while in the North polar region, negative-polarity magnetic fields dominate the other polarity. In addition, magnetic concentrations (kG-patches) in the North polar region have larger spatial size and stronger field intensity than those in the quiet region. We calculated the potential coronal magnetic field with the *Hinode* data in each region. The field in the North polar region shows that a large fraction of magnetic flux is open with the small scale closed fields, while that in the quiet region shows that the most of the magnetic fields are closed.

Using the SOT data of four years from the launch of *Hinode* to the present, we have examined the long term variation of the polar photospheric magnetic fields. Since this is an ongoing analysis, there is no clear conclusion on the time variation of the polar flux. In the South polar region, the fraction of the dominant polarity magnetic flux smoothly decreases with lower latitude for 4 years of observations. The fraction of the dominant magnetic flux does not monotonically decrease from 2006 to 2011. The faction between 60 and 70 degree in 2011 is about 5 % higher

than that of 2009 in the South polar region.

5.2 Future Workes

The following problems remain unanswered: the polarity reversal process of the global magnetic field of the Sun, and the acceleration process of the high speed solar wind in the polar coronal holes, the formation and decay processes of the polar coronal holes.

The formation process of kG-patches remains unknown. Our analysis was based on the snapshot of the photospheric magnetic fields. It is necessary to detect the their variation with an observation of high time resolution.

In Chapter 4, we have reported the time variation of the magnetic field/flux in the north and south polar regions for four years near the solar minimum. We notice the fraction of the dominant vertical magnetic flux increases with latitude and slightly decreases with time. If we continue to observe the polar regions with *Hinode*/SOT until the solar maximum, it is expected that we can observe that they become more complex and that polarity gradually reverses.

The acceleration mechanism of the fast solar wind must be related to the structure and its temporal variation of the magnetic field on the surface of the Sun, and the physical process creating the wind is still a topic of debate (Wang et al. 1989; Wang and Sheeley 1990; McComas et al. 2000; Kojima et al. 2001; Tu et al. 2005). The conventional observation of the photospheric magnetic field was based on the ground-based observations only detecting the component along the line of sight. The observation in the polar region cannot resolve the structure near the solar limb due to their low resolution, and may not accurately estimate the photospheric field in the polar coronal hole. The high-resolution observation with *Hinode*/SOT will enable us to estimate the photospheric field in the polar coronal hole. If we develop a detailed comparison between the photospheric magnetic fields and the solar wind speed above, we will be able to obtain some clues about the acceleration and the heating of the solar wind which are unsolved problems for many years.

REFERENCES

Allen, G. G., & Hagyard, M. J., 1990, *Sol. phys.*, 126, 21

Avrett, E. H. 1999, ESA Special Publications, 446, 141

Babcock, H. W., & Babcock, H. D. 1955, *Astrophys. J.*, 121, 349

Bellot Rubio, L. R. 2009, *Astrophys. J.*, 700, 284

Benevolenskaya, E. E. 2004, *Astron. Astrophys.*, 428, L5

Berger, T. E., et al. 2008, *Astrophys. J.*, 676, L89

Blanco Rodriguez, J., Okunev, O. V., Puschmann, K. G., Kneer, F., & Sánchez Andrade Nuño, B. 2007, *Astron. Astrophys.*, 474, 251

Cirtain, J. W., et al. 2007, Science, 318, 1580

Culhane, J. L., et al. 2007, *Sol. phys.*, 243, 19

DeForest, C. E., et al. 1997, *Sol. phys.*, 175, 393

del Toro Iniesta, J. C. 2003, Introduction to Spectropolarimetry, ed. J. C. del Toro Iniesta

De Pontieu, B., et al. 2007, *Publ. Astron. Soc. Japan*, 59, 655

Fox, P., McIntosh, P. & Wlison, P., R. 1998, *Sol. phys.*, 177, 375

Fujimura, D., & Tsuneta, S. 2009, *Astrophys. J.*, 702, 1443

Golub, L., et al. 2007, *Sol. phys.*, 243, 63

Harvey, J., Krieger, A. S., Timothy, A. F., & Vaiana, G. S., 1975, in Skylab Solar Workshop, 104, 50

Harvey, K. L., & Recely, F. 2002, *Sol. phys.*, 211, 31

Homann, T., Kneer, F., & Makarov, V. I. 1997, *Sol. phys.*, 175, 81

Hoyt, D. V., Schatten, K. H. 1998, *Sol. phys.*, 181, 491

Ichimoto, K., et al. 2008, *Sol. phys.*, 249, 233

Ishikawa, R., & Tsuneta, S., 2009, *Astron. Astrophys.*, 495, 607

Ishikawa, R., Tsuneta, S., & Jurčák, J., 2010, *Astrophys. J.*, 713, 1310

Ito, H., Tsuneta, S., Shiota, D., Tokumaru, M., & Fujiki, K. 2010, *Astrophys. J.*, 719, 131

Kamio, S., et al. 2007, *Publ. Astron. Soc. Japan*, 59, S757

Kano, R., et al. 2008a, *Sol. phys.*, 249, 263

Kano, R., et al. 2008b, *Publ. Astron. Soc. Japan*, 60, S827

Kojima, M., et al. 2001, *J. Geophys. Res.*, 106, 15677

Kosugi, T., et al. 2007, *Sol. phys.*, 243, 3

Leighton, R. B., 1964, *Astrophys. J.*, 40, 1547

Lin, H., Virski, J., & Zirin, H. 1994, *Sol. phys.*, 155, 243

Lites, B. W. 1996, *Sol. phys.*, 163, 223

Lites, B. W., Elmore, D. F., & Streander, K. V. 2001, in ASP Conf. Ser. 236, Advanced Solar Polarimetry-Theory, Observation, and Instrumentation, ed. M. Sigwarth (San Francisco, CA: ASP), 33

Lites, B. W., et al. 2008, *Astrophys. J.*, 672, 1273

McComas, D. J., et al. 2000, *J. Geophys. Res.*, 105, 10419

McComas, D. J., et al. 2002, *Geophys. Res. Lett.*, 29, 1290

Metcalf, T. R., 1994, *Sol. phys.*, 155, 235

Metcalf, T. R., et al. 2006, *Sol. phys.*, 237, 267

Moon, Y.-J., Wang, H., Spirock, T. J., Goode, P. R., & Park, Y. D., 1990, *Sol. phys.*, 217, 79

Okamoto, T. J., et al. 2007, Science, 318, 1577

Okunev, O. V., & Kneer, F. 2004, *Astron. Astrophys.*, 425, 321

Okunev, O. V., & Kneer, F. 2005, *Astron. Astrophys.*, 439, 323

Orozco Suárez, D., & del Toro Iniesta J. C. 2007, *Astron. Astrophys.*, 462, 1137

Orozco Suárez, D., et al. 2007a, *Astrophys. J.*, 670, L61

Orozco Suárez, D., et al. 2007b, *Publ. Astron. Soc. Japan*, 59, S837

Phillips, J. L., et al. 1995, *J. Geophys. Res.*, 22, 3301

Phillips, J. L., et al. 1995, Science, 268, 1030

Savcheva, A., et al. 2007, *Publ. Astron. Soc. Japan*, 59, S771

Savcheva, A., 2008, Proc. IAU, 247, 326

Scholl, I. F., & Habbal, S. R. 2008, *Sol. phys.*, 248, 425

Severny, A. B. 1971, Q. J. R. Astron. Soc., 12, 363

Shimizu, T., et al. 2008, *Sol. phys.*, 249, 221

Shimojo, M., & Tsuneta, S., 2009, *Astrophys. J.*, 706, L145

Shiota, D. 2009, private communication

Suematsu, Y., et al. 2008, *Sol. phys.*, 249, 197

Suzuki, T. K., & Inutsuka, S. 2006, *J. Geophys. Res.*, 111, A06101

Svalgaard, L., Duvall, T. L., Jr., & Scherrer, P. H., 1978, *Sol. phys.*, 58, 225

Tang, F. ,& Wang, H. 1991, *Sol. phys.*, 132, 247

Timothy, A. F., Krieger, A. S., & Vaiana, G. S. 1975, *Sol. phys.*, 42, 135

Topka, K., Moore, R., LaBonte, B. J., & Howard, R. 1982, *Sol. phys.*, 79, 231

Tsuneta, S., et al. 2008a, *Astrophys. J.*, 688, L1374

Tsuneta, S., et al. 2008b, *Sol. phys.*, 249, 167

Tu, C.-Y., Zhou, C., Marsch, E., Xia, L.-D., Zhao, L., Wang, J.-X., & Wilhelm, K. 2005, Science, 308, 519

Vernazza, J. E., Avrett, E. H., & Loeser, R. 1981, *Astrophys. J.*, 45, 635

Wang, Y.-M., Nash, A. G., & Sheeley, N. R., Jr. 1989, *Astrophys. J.*, 347, 529

Wang, Y.-M., & Sheeley, N. R., Jr. 1990, *Astrophys. J.*, 355, 726

Wang, Y.-M. 2009, *Space Sci. Rev.*, 144, 383

Webb, D. F., Davis, J. M., & McIntosh, P. S. 1984, *Sol. phys.*, 92, 109